Sonochemical Decomposition of Perfluorinated Surfactants: Chain Length Effects

Thesis by

Tammy Y. Campbell

In Partial Fulfillment of the Requirements

for the Degree of

Doctor of Philosophy

California Institute of Technology

Pasadena, California

2010

(Defended February 18th, 2010)

..:: dedicated to my family ::..

ACKNOWLEDGEMENTS

There is so much to be grateful for during my last five years as a graduate student at Caltech. I am eternally thankful to my advisor, Professor Michael Hoffmann for giving me the opportunity to work in his lab, which renewed my interest in environmental chemistry and its impact in the global environment. At the same time, Mike gave me the emotional and mental freedom necessary for personal growth, which enabled me to become a more passionate and better scientist. As a result, I was able to do great work on a research project for 3M, teach a few of his lectures at a graduate-level class, and give presentations at conferences. These experiences gave me the confidence to continue my aspirations towards a career in science. Overall, it has been a true honor to work for Mike here at Caltech, as he is a perfect role model and has shown me the balance between the talent and compassion that it takes to be a great scientific advisor.

I have also had the honor of working with other mentors at Caltech. Dr. Chad Vecitis, a former graduate student in the Hoffmann lab taught me everything I needed to know about my research project on perfluorochemical remediation. Chad gave me the respect and support needed to be a successful graduate student at Caltech as he helped me with experiments, papers, and presentations. He is also a great friend, as we spent time in deep conversation and shared drinks on many occasions. An industrious person of great ambition and intelligence, Chad's greatest gift is his boundless empathy and understanding for the challenges that people face in their lives and his patience and willingness to support people in his desire to see them succeed. Chad has dedicated a lot of his time and energy into mentoring; for that I am wholeheartedly grateful and wish him the best at Harvard. I am also grateful to Dr. Jie Cheng and Professor Hyungwoong Park

for enthusiastically welcoming me onto the perfluorochemical project. Jie has been so much fun and has provided me with insightful advise on my research and career endeavors. It was a great joy working with Dr. Nathan Dalleska, Director of the Environmental Analysis Center at Caltech. He helped me with my analytical chemistry, in particular with the mysterious workings of mass spectrometry. I am also grateful that Nathan allowed me to T.A. his analytical chemistry course since it allowed me to hone my skills of educating, while simultaneously providing a more in-depth understanding of analytical methods. I would also like to thank my thesis committee, Professor Harry Gray, Professor Nathan Lewis, and Professor John Bercaw, for taking time to read my work and providing helpful suggestions about my projects and ideas.

I also enjoyed spending time with past and present members of the Hoffmann lab. Dr. Christopher Boxe is a great friend and has provided me with sound career and relationship advice. I am crossing my fingers that Agata is the one for Chris. Dr. Su Young Ryu has always provided insightful experiences as a woman in science, and is always ready to listen. Dr. Angela Rincon, always full of fun and ready for lab events whether it was at the beach, Magic Mountain or drinks at the Athenaeum. Dr. Augustin Colussi, Senior Research Associate at Caltech, is a great scientist and always provides a fresh perspective on any issue. Dr. Shinichi Enami is admirable in his work ethic, friendly to everyone and is always ready to enjoy a drink and participate in lab events. Daejung Kwon, a new member to the lab, is very nice, a talented photographer and has a beautiful family. Schetema Stevens is great to talk to and very insightful. Dr. Jina Choi, friendly and inspirational in her devotion to God, is a wonderful office mate. Rifkha Kameel is someone I bonded with right away. She can talk for hours about anything and

is always full of honest opinions about my personal dilemmas. I'm so excited for the arrival of her baby. Along with Jina, I am so grateful to Rifkha for making Keck 13 such an enjoyable office to work in. Will Ford, my pseudo-therapist and close friend, definitely made Keck a brighter place with his enthusiasm and sense of humor. I am thankful to him for listening without judgment. He is one of my greatest friends. I thank Fran Matzen and Cecilia Gamboa for helping me to transition into the lab and department. I would also like to thank Professor Cliff Berkman of Washington State University: a patient, inspiring and supportive advisor who believed in my potential and ability to succeed, and who provided me with the opportunity to do organic synthesis in his lab, which gave me the confidence to pursue research at the graduate level.

I would also like to thank my close friends for helping me keep my head above water over the years. Dr. Cristal Gama and Dr. Heather Murrey are two of the best friends I took away with me from the Hsieh-Wilson lab. They are so genuine, passionate and brilliant. Cristal and Heather believed in me when I did not even have faith in myself and are the reasons I was able to make it through Caltech. Dr. Erik Rodriguez was a blast: so honest, so funny and big heart. We spent many Friday nights at Amigos drinking Long Island ice teas. I also had many good times with Rosemary Rohde, Jelena Viskota, and Rosalyn Sayaman. Girls night out definitely helped me keep my sanity as the conversations were heartfelt, yet hilarious and dancing was always a great escape. I also would like to thank my therapist, Helena Kopecky, for listening and helping me to find my own voice and reclaim my inner spirit. I must not forget Sherrell Jackson, my best friend since UCLA who has always been there for me and has taught me the important elements of emotional independence.

Finally, I would like to thank my mother (Yong), father (Joe), brother (Demetrius), and sisters (Tina and Toni), for their unconditional love, for their strength, and continuous support throughout my academic career. They are my motivation, my inspiration and my life. Thank you!

ABSTRACT

The sonochemical degradation kinetics of the aqueous perfluorochemicals (PFCs) perfluorobutanoate (PFBA), perfluorobutanesulfonate (PFBS), perfluorohexanoate (PFHA) and perfluorohexanesulfonate (PFHS) have been investigated. Surface tension measurements were used to evaluate chain-length effects on equilibrium air-water interface partitioning. The PFC air-water interface partitioning coefficients, K_{eq}^{PF}, and maximum surface concentrations, $\Gamma_{\max}^{PF}$, were determined from the surface pressure equation of state for PFBA, PFBS, PFHA and PFHS. Relative K_{eq}^{PF} values were dependent upon chain length $K_{eq}^{PFHS} \cong 2.1K_{eq}^{PFHA} \cong 3.9K_{eq}^{PFBS} \cong 5.0K_{eq}^{PFBA}$, whereas relative $\Gamma_{\max}^{PF}$ values had minimal chain length dependence $\Gamma_{\max}^{PFHS} \cong \Gamma_{\max}^{PFHA} \cong \Gamma_{\max}^{PFBS} \cong 2.2\Gamma_{\max}^{PFBA}$. The rates of sonolytic degradation were determined over a range of frequencies from 202 to 1060 kHz at dilute (< 1 μM) initial PFC concentrations. Under all conditions, the time-dependent PFC sonolytic degradation was observed to follow pseudo-first order kinetics suggesting bubble-water interface populations were below saturation. The PFHX (where X = A or S) sonolysis rate constant was observed to peak at an ultrasonic frequency of 358 kHz, similar to PFOX. In contrast, the PFBX degradation rate constants had an apparent maximum at 610 kHz. Degradation rates observed for PFHX are similar to previously determined PFOX rates, $k_{app,358}^{PFOX} \cong k_{app,358}^{PFHX}$. PFOX is sonolytically pyrolyzed at the transiently cavitating bubble-water interface suggesting that rates should be proportional to equilibrium interfacial partitioning. However, relative equilibrium air-water interfacial partitioning predicts that $K_{eq}^{PFOX} \cong 5K_{eq}^{PFHX}$. This suggests that at dilute PFC concentrations, adsorption to the bubble-water interface is sonochemically mediated.

PFC sonochemical kinetics are slower for PFBS and further diminished for PFBA as compared to longer analogs suggesting that PFBX surface films are of lower stability due to their greater water solubility. Furthermore, application of a Langmuir type kinetic model on the basis of a heterogenous solution system is applied in evaluating the sonochemical effects on surface activity and the absolute rates over four orders of magnitude of initial PFYX (Y = H or B, X = A or S). Investigations on the effects of ultrasound power densities at 83.3, 167, 250, and 333 W L^{-1} have been carried out. Rate constants exhibit a linear increase with increasing power density for all species, thus rates can be increased by simply increasing the power density. Degradation rates are compared at single frequency exposures of 202, 358, and 610 kHz and compared to dual frequency exposures at 20 + 202 and 20 + 610 kHz under the same power conditions (250 W L^{-1}). A synergistic enhancements in degradation rates for PFOS (~12%) and PFOA (~23%) were observed for 20 + 202 kHz simultaneous exposure. Frequency and power are parameters that can affect the sonochemical efficiency by modifying peak collapse temperature and by controlling the size and population of transiently cavitating bubbles.

TABLE OF CONTENTS

Chapter 1

Perfluorinated Surfactant Chain-Length Effects on Sonochemical Kinetics

Introduction

Fluorinated surfactants, a subset of fluorochemicals (FCs), are composed of a hydrophobic, per- or poly- fluorinated organic tail and highly water-soluble head group. Perfluorination, the replacement of all hydrogens with fluorines, imparts these compounds with unique physical properties such as great chemical inertness, minimal coefficients of friction, and low polarizabilities (i.e. hydro- and oleo-phobicity or fluorophilicity), making them desirable for a wide variety of commercial applications.[1] FCs are commonly employed to waterproof textiles and paper products, to protectively coat metals, as high-temperature lubricants,[2] in fire retardants, such as aqueous film-forming foams (AFFF)[3], and in semi-conductor processing.

Development of aqueous FC remediation technologies is of interest because of the environmental persistence of many PFCs (perfluorchemicals), which has led to their global distribution in the environment and the presence of some FCs in human[4] and wildlife[5, 6] plasma. Recent studies have detected low levels of perfluorobutane sulfonate (PFBS) in marine wildlife of Western Europe,[7] but at significantly lower levels than perfluorooctane sulfonate (PFOS) and perfluorooctanoate (PFOA). Similar to PFOX (where X = (S)ulfonate or c(A)rboxylate and O = (O)ctane), PFHX (H = (H)exane) and PFBX (B = (B)utane) are recalcitrant towards most conventional wastewater remediation strategies.[10, 11] Shortening of the hydrophobic tail increases water solubility. Accordingly, PFBS and PFBA exhibit a lower activity towards adsorption based removal techniques such as granular activated carbon (GAC),[12] which is currently used to remove PFOS and PFOA from pre-treated wastewater streams.[13]

Sonochemistry has been reported to be effective for the destruction of PFOS and PFOA over a range of initial concentrations. High C-F bond dissociation energies (450-530 kJ mol^{-1}), C-C bond strengthening due to fluorination(~14-17 kJ mol^{-1} per fluorine atom) and the great one-electron reduction potential of fluorine (E^0 = 3.6 V) highlights the importance of high cavitation temperatures towards the degradation of fluorochemicals.[14, 15] Interfacial temperatures produced by a transient bubble collapse provides sufficient energy for the thermolytic decomposition of FCs.[16] Initially, the C-C or C-S bond between the fluorocarbon tail and carboxylate or sulfonate head group is cleaved yielding a fluorochemical intermediate of high Henry's constant that migrates to the bubble core for further thermal and radical decomposition.[17-19] Consequently, aqueous solutions of PFOS and PFOA are readily mineralized during ultrasonic irradiation to their inorganic constituents: F^-, SO_4^{2-}, CO and CO_2 .[16, 17]

Acoustic cavitation events are responsible for the chemistry observed during ultrasonic irradiation of aqueous solutions. Cavitation occurs due to the acoustically driven growth (low P) and subsequent collapse (high P) of preexisting aqueous bubbles at ambient temperatures and pressures.[16] The transient collapse of cavitation bubbles is quasi-adiabatic, heating the vapor phase inside the cavity to temperatures of 4000 K to 5000 K, and yielding pressures on the order of 1000 bar.[20-24] Bubble-water interfacial temperatures have been estimated to be 500 to 1000K.[21, 25] As a direct consequence of these transient, localized, high temperatures and pressures, solutes that have partitioned into the vapor phase, or to the bubble-water interface will be pyrolytically decomposed to various extents. Water vapor within the collapsing cavity is homolytically-cleaved generating hydroxyl radicals, O-atoms and hydrogen atoms.[23, 26] The radicals can also

degrade organics in the bubble vapor, at the bubble-water interface, and even in bulk aqueous solution.

Sonochemical degradation kinetics are a rough function of the physicochemical properties of an organic compound. The physiochemical properties of a compound can be used to evaluate relative partitioning to the 1) bubble vapor, 2) bubble-water interface and 3) bulk aqueous phase in an ultrasonically irradiated solution, which are of decreasing sonochemical intensity. Listed in Table 1 are the physicochemical properties of perfluorinated surfactants of various chain lengths and headgroups; PFOS, PFOA, PFHS, PFHA, PFBS, and PFBA.

The perfluorinated surfactants will preferentially adsorb to the air-water interface, since they consist of a hydrophobic tail and a hydrophilic ionic headgroup. PFOS and PFOA have been shown to sonochemically decompose via pyrolytic reactions at the bubble-water interface. Thus, the sonolytic degradation rate will be proportional to the fraction of total surfactant molecules that adsorb to the interface of the transiently cavitating bubbles.[27, 28] However, estimation of the fraction of total surfactant molecules adsorbed to transiently cavitating bubbles is difficult, due to high-velocity bubble radial oscillations (>5 m s^{-1}) and short bubble lifetimes (<100 μs), which preclude utilization of equilibrium partitioning values.

Table 1. Physicochemical properties of perfluorinated surfactants. N/A means data not available.

Abbreviation	Name	Chemical Formula	Chemical Structure of the anionic form	M.W. (g mol^{-1})	Tail Carbons	pKa	Water Solubility (g L^{-1})	P_{vapor} (Pa @ 20 °C)
PFOA-A	ammonium perfluorooctanoate	$C_8F_{15}O_2NH_4$	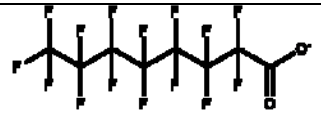	414	7	-0.1	9.5[56]	9.3 x 10^{-3}[57]
PFOS-K	potassium perfluorooctane sulfonate	$C_8F_{17}SO_3K$	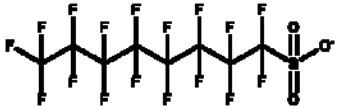	538	8	-3.27	0.5[58]	3.3 x 10^{-4}[57]
PFHA-A	ammonium perfluorohexanoate	$C_6F_{11}O_2NH_4$	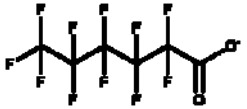	314	5	N/A	N/A	N/A
PFHS-K	potassium perfluorohexane sulfonate	$C_6F_{13}SO_3K$	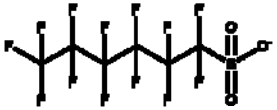	438	6	N/A	N/A	N/A
PFBA-A	ammonium perfluorobutanoate	$C_4F_7O_2NH_4$	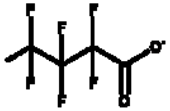	214	3	0.4[56]	N/A	<1.2 x 10^{-5}[10]
PFBS-K	potassium perfluorobutane sulfonate	$C_4F_9SO_3K$	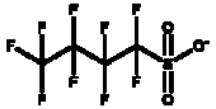	338	4	N/A	46.2	N/A

A number of previous studies have evaluated surfactant adsorption to acoustic cavitation bubbles. Fyrillas and Szeri used numerical simulations to show that high-velocity bubble oscillations drive an increased number of surfactant molecules to lightly-populated interfaces, while radial and, thus, surface area minimums limit the maximum interfacial surfactant concentration.[29] Sostaric and Reisz determined that radical scavenging efficiency increases at high (>1 mM) surfactant concentrations with decreasing n-alkyl chain length in order of SPSo (sodium 1-pentanesulfonic acid) > SOS (sodium n-octyl sulfate) ~ SOSo (sodium 1-octanesulfonic acid) > SDS (sodium dodecyl sulfate) or that the sonolytic rate maximums of nonvolatile alkyl surfactants does not correlate with the Gibbs surface excess.[30] Acoustic emission spectra studies by Greiser and Ashokkumar reveal the reduction of bubble coalescence and bubble clustering upon increasing SDS concentrations to 0.5 to 2 mM.[31] Vecitis et al. observed an enhancement of PFOS and PFOA bubble surface activity at low (<10 μM) concentrations.[32] Cheng et al. showed that addition of relatively high (>10 mM) concentrations of semi-volatile organics did not affect PFOS and PFOA (<1 μM) sonochemical rates.[33]

Here, we investigate the ultrasonic degradation kinetics of dilute aqueous (<1 μM) solutions of the perfluorochemicals PFHS, PFHA, PFBA and PFBS. The FC sonochemical degradation rate, chain-length dependence is compared to their equilibrium air-water interface partitioning chain-length dependence, as determined by surface tension measurements. The physical processes that govern sonochemical kinetics for dilute FCs, and how these processes are affected by acoustic frequency are discussed.

Experimental Methods

Perfluorobutyric acid (PFBA) and perfluorohexanoic acid (PFHA) were purchased from Sigma Aldrich. Potassium perfluorobutane-1-sulfonate (PFBS) and potassium perfluorohexane-1-sulfonate (PFHS) were provided by 3M. Ammonium acetate (> 99%) and methanol (HR-GC > 99.99%) were obtained from EMD Chemicals Inc. Aqueous solutions were prepared with purified water using a Milli-Q system (18.2 MΩ cm resistivity). Acid solutions were brought to a pH of 7 ± 0.5 by addition of ammonium hydroxide.

Ultrasonic frequencies of 202, 358, 610, and 1060 kHz were generated using Allied Signal – Elac Nautik ultrasonic transducers with the reaction solution held in a 600 mL jacketed glass reactor. The applied power density was 250 $W\text{-}L^{-1}$. The calorimetric power density was determined to be 75 ± 10% of the applied power density. The temperature was controlled at 10 ^{o}C with a Haake A80 refrigerated bath. All reactions were sparged with argon for at least 30 minutes prior to and during the reaction. PFBS and PFBA were sonicated simultaneously at initial concentrations of 0.30 μM for PFBS and 0.47 μM for PFBA. PFHS and PFHA were sonicated simultaneously at an initial concentrations of 0.23 μM for PFHS and 0.32 μM for PFHA. Dilute concentrations (<1 μM) were chosen to maintain lightly populated bubble-water interfaces. The specific concentrations were chosen because they were just below the highest concentration in the HPLC-MS calibration curve, thus yielding the widest analytical range possible. The variation in initial concentrations will not affect the results, since they will be discussed in terms of pseudo first-order rate constants, which are normalized to the initial concentration.

PFC concentrations were analyzed by HPLC-ES-MS. The samples were placed into 750 μL polypropylene auto-sampler vials and sealed with a PTFE septum crimp cap. 20 μL of collected or diluted sample was injected onto an Agilent 1100 LC for separation on a Betasil C18 column (Thermo-Electron) of dimensions 2.1 mm ID, 100 mm length and 5 μm particle size. A 2 mM aqueous ammonium acetate/methanol mobile phase at a flow rate of 0.3 mL min^{-1} was used with an initial 5:95 aqueous/methanol composition. The eluent composition was increased to 90:10 over 12 minutes to separate the PFCs. HPLC effluents were analyzed with an Agilent Ion Trap MS in the negative ion mode for the perfluorohexanesulfonate molecular ion (m/z = 399), the perfluorobutanesulfonate molecular ion (m/z = 299), the decarboxylated perfluorohexanoate ion (m/z = 269) and the decarboxylated perfluorobutanoate ion (m/z = 169). The nebulizer gas pressure was 40 PSI and the drying gas flow rate and temperature were 9 L min^{-1} and 325 $^{\circ}$C, respectively. The capillary voltage was set at + 3500 V and the skimmer voltage was -15 V. Quantification was completed by first producing a calibration curve using 8 concentrations between 1 ppb and 200 ppb fitted to a quadratic with X^{-1} weighting.

Surface tension measurements were made with a De Nouy tensiometer utilizing the ring method. The tensiometer was calibrated with a weight of known mass. Each sample was measured three times. The PFHS and PFBS surface tension measurements were on concentrations up to 10 mM and 100 mM, respectively, where the compounds became insoluble. The curve was fitted to the surface pressure equation of state using Matlab™ to determine the equilibrium air-water partitioning coefficient and the maximum surface concentration.

Results and Discussion

PFHX and PFBX Equilibrium Air-Water Interface Partitioning

PFHX and PFBX equilibrium air-water partitioning coefficients were calculated for PFHS, PFHA, PFBS, and PFBA using PFC concentration dependent surface tension measurements. From these surface tension measurements, Γ_{max}^{PFYX} and K_{eq}^{PFYX}, can be determined by fitting of the data to the surface equation of state:

$$\Pi = \gamma_0 - \gamma = nRT\,\Gamma_{max}\ln(1 + K_{eq}^{PFYX}\,[PFYX]) \qquad (2)$$

where Π is the surface pressure in N m^{-1}, γ_0 = 0.072 N m^{-1} is the surface tension of pure water and γ is the surface tension at the bulk aqueous PF concentration, [PFYX]. K_{eq} (L mol^{-1}) represents the bulk water to air-water interfacial partitioning coefficient and Γ_{max} is the maximum surface concentration in mol m^{-2}. According to the surface tension results in Figure 1, the overall order of surface activity is PFHS(C_6) > PFHA(C_5) > PFBS(C_4) > PFBA(C_3). C_n represents the number of carbons in the hydrophobic chain.

Of note in Figure 1, is the fact that the sulfonates, including PFOS, all become insoluble prior to reaching their critical micelle concentration (i.e., when the fractional coverage of the air-water interface is in unity). The perfluoro-sulfonate insolubility occurs at a surface tension of 40 ± 5 mN m^{-1}, suggesting there is a critical surface pressure at which perfluoro-alkylsulfonates undergo a phase transition.

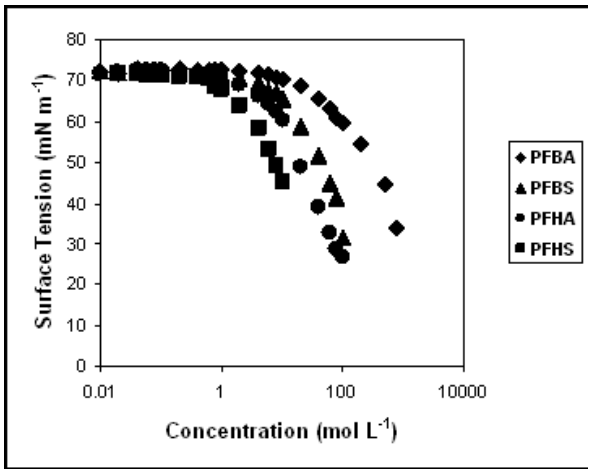

Figure 1. Plot of surface tension vs. aqueous PFBS (▲), PFBA (♦), PFHS (■) and PFHA (●) (mM).

Listed in Table 2 are the maximum surface concentrations, Γ_{max}^{PFYX}, and equilibrium partitioning constants, K_{eq}^{PFYX}, for PFBX, PFHX, and PFOX.[32] With the exception of PFBA, Γ_{max} is similar for all the compounds.

Table 2. Equilibrium air-water interface partitioning constants, K_L and Γ_{max} for PFOS, PFHS, PFBS, PFOA, PFHA, and PFBA.

PFC	**K_L (L mol^{-1})**	**Γ_{max} (mol m^{-2})**	**R^2**
PFOS	1871 ± 852 (32)	(5.0 ± 2.2) x 10^{-6} (32)	0.99
PFHS	158 ± 32.8	(5.7 ± 0.8) x 10^{-6}	0.999
PFBS	40.4 ± 8.60	(4.4 ± 0.5) x 10^{-6}	0.998
PFOA	361 ± 25.3 (32)	(4.4 ± 0.2) x 10^{-6} (32)	
PFHA	75.6 ± 11.4	(4.8 ± 0.4) x 10^{-6}	0.998
PFBA	31.7 ± 4.8	(1.95 ± 0.12) x 10^{-6}	0.998

In Figure 2, K_{eq}^{PFYX} is plotted as a semi-log function of C_n-tail. Overall, there is a wide range of K_L that spans two orders of magnitude for the perfluoro-carboxylates and sulfonates. Note that the perfluoro-carboxylates have one less fluorine-containing carbon than the perfluoro-sulfonates. The semi-log perfluoro-carboxylate and -sulfonate empirically fit to the equations: $y_{sulfonates} = 0.78e^{0.18}$; $y_{carboxylates} = 0.99e^{0.13}$. The perfluoro-carboxylate and -sulfonate curves in Fig. 2 do not overlap, indicating the headgroup speciation affects the air-water interface partitioning, with the perfluoro-carboxylate being less surface active than the perfluoro-sulfonate. This result is in qualitative agreement with previously reported acetic acid[34] and methanesulfonate[35] hydration energies. The greater hydration free energy of acetic acid as compared to methanesulfonate indicates that it will associate itself to a greater extent with bulk water implying a lower interfacial activity.

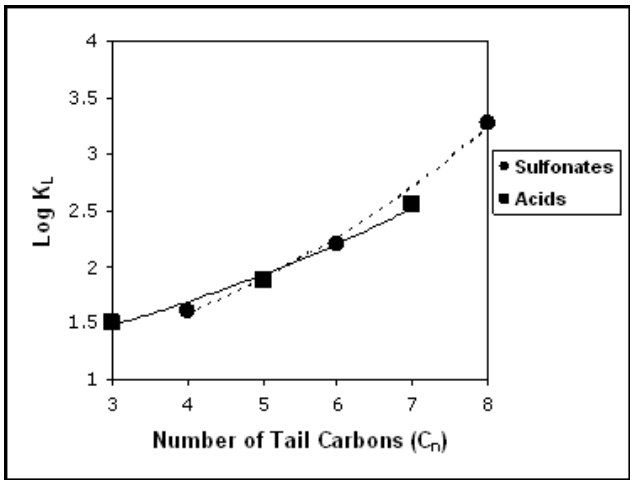

Figure 2. Plot of chain length effects on the interfacial partitioning coefficients for the sulfonates (●) and carboxylates (■).

The calculated Γ_{max}^{PFYX} values all fall into the range 5.3 ± 0.7 x 10^{-6} mol m^{-2} except PFBA, which has a maximum surface concentration, Γ_{max}^{PFBA} = 2.1 ± 0.1 x 10^{-6} mol m^{-2}. The maximum surface concentration is a balance between attractive forces of the hydrophobic tail to the air-water interface and steric/coulombic repulsion of neighboring hydrophilic headgroups.[36] Neutron reflectivity studies have estimated that the first 2-3 PFOA carbons are below the air-water interface.[37] Assuming a similar structure for PFBA, > 50% of its carbons would be beneath the air-water interface. The reduction in hydrophobic tail interactions for PFBA can be semi-quantitatively evaluated by conversion of maximum surface concentrations to area per molecule which would be 0.6 nm^2/PFYX and 1.5 nm^2/PFBA, which converts to a circle of radius r= 0.16 nm and r = 0.26 nm, respectively. 0.16 nm is on the order of the C-F bond length (0.13 nm) in CHF_3, suggesting relatively intimate contact between hydrophobic chains. Whereas, the 0.26 nm in PFBA is more representative of an ionic hydration sphere (0.3-0.4 nm), suggesting that the hydrophobicity of PFBA's short tail (C_3) cannot compensate for the coulombic repulsion between neighboring carboxylate groups.

PFHX and PFBX Frequency Dependent Sonochemical Kinetics

The semi-log, time-dependent sonochemical degradation profiles of aqueous PFHS, PFHA, PFBS and PFBA at acoustic frequencies of 202, 358, 610 and 1060 kHz (PD = 250 W L^{-1}, T = 10 ºC, Ar) are depicted in Figures 3a through 3d. Each data point represents the average of three experiments (error bars were not added, due to space issues). Ultrasonic irradiation was performed at initial PFC concentrations of $[PFBA]_i$ = 0.47 μM, $[PFBS]_i$ = 0.30 μM, $[PFHA]_i$ =0.32 μM and $[PFHS]_i$ =0.23 μM with the initial pH between 7-8. The initial PFC concentrations were degraded by at least PFBA (57%),

PFBS (66%), PFHS (86%) and PFHA (90%) after 120 minutes of exposure to ultrasound at all frequencies. In comparison, PFOS and PFOA were degraded to 87% and 99% of their initial concentrations after 120 minutes of ultrasonic irradiation.

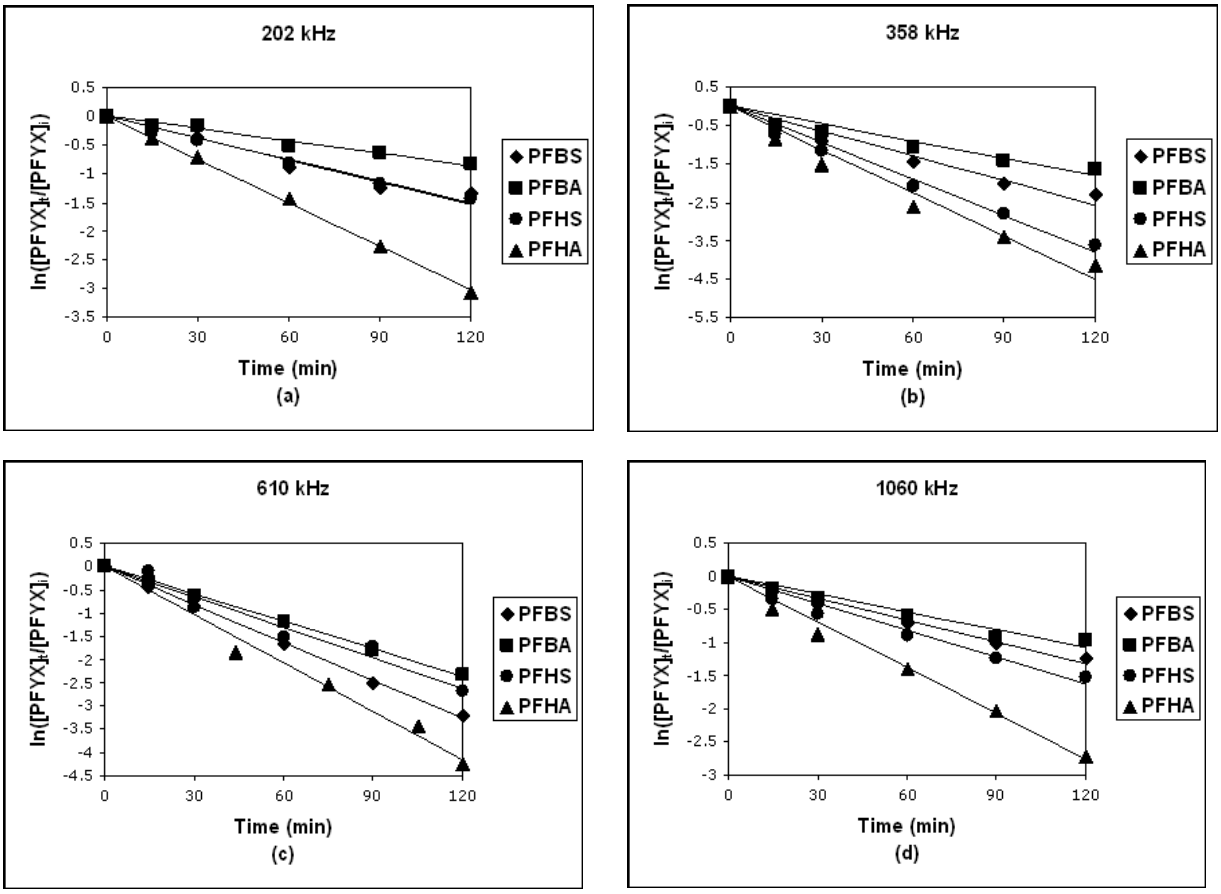

Figure 3. Pseudo first-order rate of degradation of PFYX at 250 W L^{-1} in Ar(g) saturated solutions at pH 7 and 10 °C. PFHA (▲) and PFHS (●) PFBA (■) and PFBS (♦). (3a) 202 kHz, k_{app}^{-PFBS} = 0.013 min^{-1}; k_{app}^{-PFBA} = 0.007 min^{-1}; k_{app}^{-PFHS} = 0.012 min^{-1}; k_{app}^{-PFHA} = 0.019 min^{-1}, (3b) 358 kHz, k_{app}^{-PFBS} = 0.018 min^{-1}; k_{app}^{-PFBA} = 0.012; k_{app}^{-PFHS} = 0.030; k_{app}^{-PFHA} = 0.039, (3c) 610 kHz, k_{app}^{-PFBS} = 0.023; k_{app}^{-PFBA} = 0.017; k_{app}^{-PFHS} = 0.022; k_{app}^{-PFHA} = 0.036, (3d) 1060 kHz, k_{app}^{-PFBS} = 0.009; k_{app}^{-PFBA} = 0.008; k_{app}^{-PFHS} = 0.012; k_{app}^{-PFHA} = 0.022.

The plots of ln ($[PFYX]_t/[PFYX]_i$, where Y signifies the chain length B (butane), H (hexane), O (octane) and X signifies the headgroup A (carboxylate) or S (sulfonate) vs. time plots are linear indicating pseudo-first kinetics, Fig. 3a-d. Consistent with an interfacial pyrolysis decomposition mechanism where concentrations are well below surface

$$d[PFYX]/dt = -k_{app}^{PFYX}\ [PFYX] \quad (1)$$

in which k_{app}^{PFYX} is the apparent first-order rate constant. However, the kinetic order changes below -3 where PFYX is < 10 nM causing change to the kinetic order. Rate constants determined from linear regression of data in Fig. 3 at 358 kHz follows the order $k_{app}^{PFOA} \cong k_{app}^{PFHA} > k_{app}^{PFOS} \cong k_{app}^{PFHS} > k_{app}^{PFBS} > k_{app}^{PFBA}$. The pseudo first-order rate constants and half-lives for the degradation of the six perfluoro-compounds at 250 W L^{-1} and 358 kHz are listed in Table 3. PFHX relative rates are similar to relative rates observed for the PFOX where, $\frac{k_{app}^{PFOA}}{k_{app}^{PFOS}} = 1.7$ and $\frac{k_{app}^{PFHA}}{k_{app}^{PFHS}} = 1.8$, reflecting that the carboxylates degrade faster than the sulfonates. In contrast, the degradation rate constant for the C_4 sulfonate is 1.5 times that of the carboxylate, $\frac{k_{app}^{PFBA}}{k_{app}^{PFBS}} = 0.66$.

Table 3. Apparent first-order rate constants and half-life for the degradation of PFXY, where X = B, H, or O and Y = A or S at 358 kHz, 250 W L^{-1}, 10 °C, Ar.

PFC	k_{app} (min^{-1})	$\tau_{1/2}$ (min)
PFBA	0.012 ± 0.001	57.2
PFBS	0.018 ± 0.0023	42.3
PFHA	0.053 ± 0.001	16.8
PFHS	0.030 ± 0.003	23.2
PFOA[17]	0.048 ± 0.001	16.9
PFOS[17]	0.028 ± 0.005	25.7

The PFBX and PFHX sonochemical degradation rate constants, k_{app}^{PFYX} , were determined in this work at acoustic frequencies ranging from 202 kHz to 1060 kHz at an applied acoustic power density of 250 W L^{-1}, at 10 °C in argon. The PFOX rates were taken from Vecitis et al.[17] The pseudo-first order sonolytic rate constants, k_{app}^{PFYX} , versus frequency for PFBA, PFBS, PFHA, PFHS, PFOA, and PFOS are plotted in Fig. 4a and b, for the sulfonates and carboxylates respectively. The degradation rate constants for the PFHX and PFOX have apparent maxima at 358 kHz. The PFBX sonochemical degradation rate constants have apparent maxima at 610 kHz. The observed PFOX and PFHX rate constant vs. frequency trends are comparable with previous reports[38] on the sonochemical degradation of chlorocarbons. Rate maximums at 358 kHz are due to maximum number of bubble events per unit time. The observed PFBX kinetically-optimal frequency of 610 kHz is similar to reports on chlorocarbon sonolysis.[24, 39] A sonolytic rate maximum at 610 kHz is due to enhanced bulk aqueous to cavitating bubble mass transfer effects .[24]

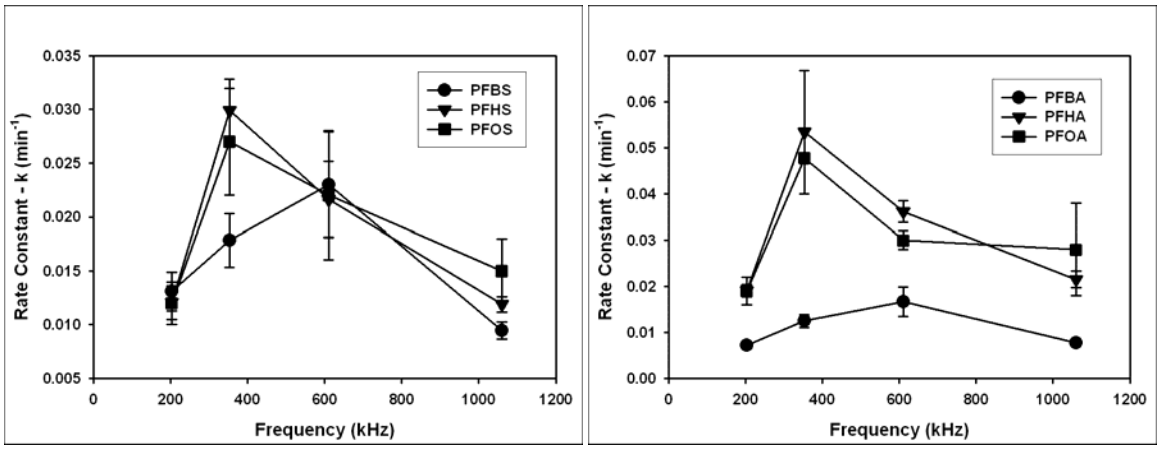

Figure 4. Rate constant and frequency dependence at 202, 358, 610 and 1060 kHz at 250 W L^{-1}, 10 °C, Ar for (4a) PFBS (●), PFHS (▼) and PFOS (■) and (4b) PFBA (●), PFHA (▼), and PFOA (■).

Sonochemical Kinetics Frequency Dependence

Acoustic frequency is one of many sonochemical parameters that modulates the cavitation dynamics of the bubble cloud present in solution. Sonochemical parameters such as power density, [25, 40, 41] reactor design,[25] area of the emitting surface,[41] dissolved gas,[40] and nature of the solvent[40] also affect cavitation dynamics. Variations on the applied frequency can affect 1) the temperature and pressure inside the bubble, [19, 27, 40, 42] 2) the number and distribution of bubbles, [40] 3) bubble size and lifetime, [18, 26, 40, 43, 44] 4) the dynamics and symmetry of collapse, [26, 40, 43, 44] and 5) radical dispersion into solution.[40, 41, 45] All the previously stated factors are interdependent in controlling sonochemical events.

The effect of acoustic frequency on sonochemical kinetics has been previously reported for a number of chemicals.[18, 19, 39-46] The rate of sonochemical potassium iodide oxidation was increased 8-fold at 300 kHz compared to 20 kHz at 2 watts of applied power.[41] The first-order rate constant for the degradation of aqueous phenyl

trifluoromethylketone was 14 times higher at 515 kHz, as compared to 30 kHz frequency.[19] The maximum 1,4-dioxane sonochemical reaction rates was observed at 358 kHz over the frequency range of 205 to 1071 kHz.[44] Over the range of 20 to 1000 kHz, the highest rate of H_2O_2 and hydroxyl radical production was observed at 500 kHz during sonolysis and the lowest production rates occurred at 20 kHz, the relative rates were not affected by the sparging gas.[26] Finally, the first-order degradation rate constants for chlorinated methanes, ethanes, and ethenes sonicated between frequency range of 205 - 1078 kHz showed an apparent maximum at 618 kHz.[39]

At higher frequencies, >100 kHz, the total number of transient cavitation bubble events per unit-time is larger and the active bubble populations account for a larger fraction of the total reactor volume.[19, 47] Average bubble vapor temperatures have little frequency dependence, [42] suggesting that the total number of bubble events per unit-time is a primary factor in determining sonochemical kinetics. Enhanced mass transfer brought on by high-velocity bubble oscillations will also increase the PFC diffusion rate from bulk water to the bubble surface.[29, 32, 39, 48] As acoustic frequency increases, a stable cavitation bubble will oscillate more frequently per unit-time leading to a more rapid rectified diffusion. The approximate resonance radius of a bubble is given by the equation $R_r^2 = 3\kappa P_0/\rho\omega_r^2$, where R_r represents the resonance radius, ω_r the resonance frequency, ρ the density of the solution, κ, the polytropic index, and P_0, the hydrostatic pressure. [24, 26] For example: in Table 4, the resonance radius of bubbles produced at frequencies of 202.6, 358, 610 and 1060 kHz are listed, reflecting the changes between the relative interfacial properties verses the gas phase properties.

Table 4. Resonance radius values (μm) and collapse times (μs) as a function of frequency (kHz).

Frequency (kHz)	Resonant Radius (μm)	Surface Area A (μm^2)	Volume V (nL)	A/V (μm^{-1})
202	17.8	3.97×10^3	0.023	0.17
358	10.0	1.26×10^3	0.0042	0.30
610	5.88	4.34×10^2	0.00085	0.51
1060	3.38	1.43×10^2	0.00016	0.88

Comparisons between bubble-surface sites to gas-phase sites as a function of frequency reveals that smaller cavitation bubbles with larger surface-to-volume ratios become prominent at higher frequencies.[24] Thus, increasing frequency results in more bubble events per unit-time and more extensive mass transfer of the solute from the bulk to the bubble interface[24] due to an increase in surface-active sites for enhanced adsorption. As a result, at higher frequencies there is mass transport of weakly partitioning PFCs from the bulk to cavitation bubbles where they can be decomposed by interfacial pyrolysis.

The total number of active bubble events per unit-time and the mass transfer of the perfluorinated species to the bubble surface [44] are two frequency dependent factors that act concomitantly on PFC degradation kinetics. The apparent frequency maximum for PFHX is 358 kHz and for PFBX is 610 kHz (Figure 4a and 4b).

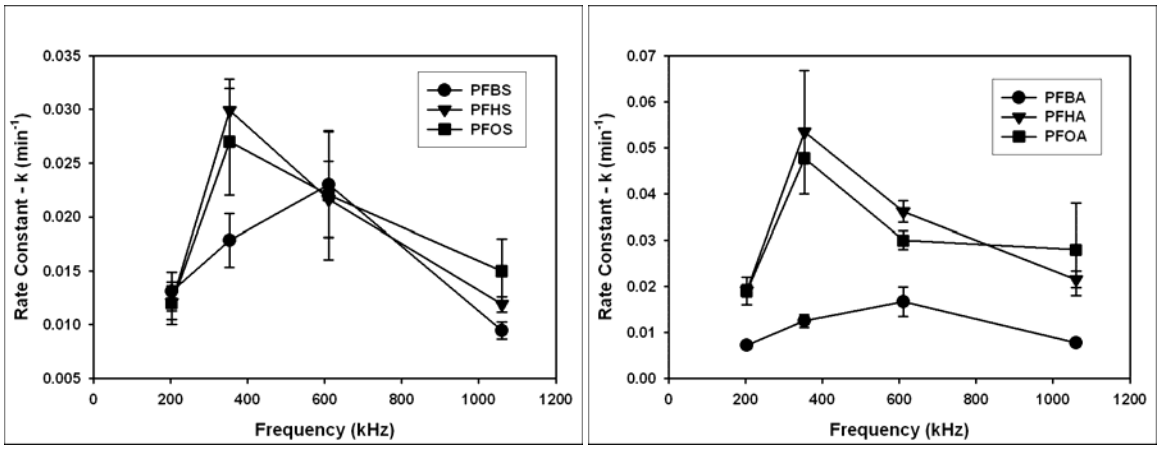

Figure 4. Rate constant and frequency dependence at 202, 358, 610 and 1060 kHz at 250 W L^{-1}, 10 °C, Ar for (4a) PFBS (●), PFHS (▼) and PFOS (■) and (4b) PFBA (●), PFHA (▼), and PFOA (■).

Since 358 kHz is the optimal frequency for PFHX, sonochemical kinetics suggests that the number of cavitation events per unit-time and, thus, the intrinsic maximum chemical reaction rate, mediates PFHX degradation kinetics. As 610 kHz is the optimal frequency for PFBX sonolysis, it suggests that mass transfer to the bubble-water interface and, thus, extent of adsorption is rate-limiting. Consistent with surface tension results, Figure 1 and Table 2, which indicate that PFBX is less surface-active than PFHX. [28, 30, 49]

For PFHX and PFBX, as the frequency increases beyond their optimal values, 358 kHz and 618 kHz, respectively, decomposition rates decrease approximately linearly with increasing frequency. At the highest frequency tested, 1060 kHz, the half-period for rarefaction of the acoustic wave is only 0.47 μs, which is insufficient time for the bubble to undergo the rapid growth required for transient cavitation limiting the number of transient cavitation events. The 0.47 μs compression half-period is approaching the characteristic time for transient bubble collapse and may interrupt these high-temperature events prior to completion. The majority of the bubbles at high frequencies is undergoing

stable cavitation, growing over many acoustic cycles, via rectified diffusion, but never transiently collapsing.[30] The gas and interface temperatures of these stable cavitation bubbles are greater than ambient, but do not approach the extremes of transiently cavitating bubbles.[21] The lower number of transient bubble events per unit-time with increasing frequency results in a decrease in PFC sonochemical rates (Figures 4a and 4b).

PFHX and PFBX Sonochemical Kinetics Adsorption Dependence

Ultrasonic irradiation of aqueous solutions creates three distinct reaction zones of varied intensity: the core of the hot spot, the hot shell surrounding the hot spot, and the bulk solution at ambient temperature.[30] The physicochemical properties of a compound will determine its relative partitioning into each of the three acoustic cavitation zones, which, in turn, will be proportional to that compounds sonochemical kinetics. For example, the relatively high Henry's Law constants for carbon tetrachloride and chloroform (K_H = 2454 Pa m^3 mol^{-1} for CCl_4 and 537 Pa m^3 mol^{-1} for $CHCl_3$), [39,50] correspond to their preferred localization at the high temperature bubble interior (205 kHz, 0.15 mM, k = 7.3 x 10 s^{-1} for CCl_4 and 4.7 x 10 s^{-1} for $CHCl_3$).[39] The sonolysis products of aqueous solutions containing surfactants OGP (n-octyl-β-D-glucopyranoside) and DGP (n-decyl-β-D-glucopyranoside) indicated surfactant localization at the bubble-water interface (0.1 to 6 mM, 614 kHz or 1.057 MHz, 0.1 to 6 mM). [51] In this case, the surfactants reacted with OH radicals that had diffused from the bubble core to the surface, which lead to an apparent, strong inhibition of H_2O_2 production.

Concentration-dependent sonochemical kinetics of PFOA and PFOS were well fitted to the Langmuir-Hinshelwood model,[32] where kinetic saturation is a result of a finite number of adsorption sites. The experiments performed here were at dilute surfactant (>1

μM), orders of magnitude below surface saturation. The sonochemical kinetics observed here can be modeled as the low-concentration limit of Langmuir-Hinshelwood kinetics.[52] The observed rate is proportional to θ^{PFYX}, the fraction of total PFYX molecules adsorbed to the bubble-water interface, eq. 3[32] and the absolute degradation rate can be modeled by eq. 4.

$$\theta^{PFYX} = \frac{K_{eq}^{PFYX}[PFYX]}{1 + K_{eq}^{PFYX}[PFYX]} \tag{3}$$

$$\frac{d[PFYX]}{dt} = -k_{app}^{-PFYX}[PFYX] = -k_{\Delta}^{-PFYX}\theta^{PFXY} \tag{4}$$

where k_{app}^{-PFYX} is the pseudo first-order rate constant in s^{-1} and k_{Δ} is the maximum intrinsic chemical reaction rate in M s^{-1}, attained when all the transiently cavitating bubble surface sites are occupied. At low concentrations when the surface is under-saturated:

$$K_{eq}^{PFYX}[PFYX] << 1 \tag{5}$$

$$\theta^{PFYX} = K_{eq}^{PFYX}[PFYX] \tag{6}$$

$$\frac{d[PFYX]}{dt} = -k_{\Delta}^{-PFYX} K_{eq}^{PFYX}[PFYX] \tag{7}$$

$$k_{app}^{-PFYX} = k_{\Delta}^{-PFYX} K_{eq}^{PFYX} \tag{8}$$

In the Langmuir-Hinshelwood model at low concentrations of surfactants, the kinetics are controlled by the fraction of the total PF molecules adsorbed to the bubble-water interface leading to apparent pseudo first-order decomposition.[32]

According to the equilibrium-partitioning coefficients listed in Table 2 and Figure 2, where the K's are plotted as a function of the tail carbon number, the sulfonates adsorb to the air-water interface more effectively than acids.[32] However, the rate of degradation of

the carboxylate is greater for the C_6 and C_8 compounds, suggesting a larger thermal activation energy for the sulfonate.[17,53] In contrast, the C_4 sulfonates degrade faster than the carboxylates, suggesting that the shorter chain length affects either dynamic adsorption under ultrasonic irradiation or thermal activation energy. The former is more plausible than the latter since hydrophobic tail-length has significant effects on air-water interface partitioning. Also, the PFBX degradation rates are slower than their PFOX and PFHX analogs, with the relative difference being greater for PFBA, $k_{app}^{\text{-PFHA/PFOA}} / k_{app}^{\text{-PFBA}} = 4.4$, than PFBS, $k_{app}^{\text{-PFHS/PFOS}} / k_{app}^{\text{-PFBS}} = 1.6$, suggesting that once the perfluorinated tail-length is less than 5 carbons (C_4-PFBS, C_3-PFBA), the dynamic adsorption to the interface during sonolysis occurs to a lesser extent. As the tail-length decreases, the hydrophobic interfacial attraction can not compensate for the coulombic repulsion between the ionic headgroups.[36] Thus, PFBA's low relative rate where $k_{app}^{\text{-PFBS}} = 1.5 k_{app}^{\text{-PFBA}}$ vs. $k_{app}^{\text{-PFHA/PFOA}} = 1.7\text{-}1.8 k_{app}^{\text{-PFHS/PFOS}}$ is that PFBA is more water soluble, as a result of its shorter chain length, consistent with PFBA's smaller maximum surface excess concentration.

Figure 5 shows the ratio of PFBX, PFHX, and PFOX rate constants as a function of frequency. For PFHX and PFOX, frequency has little effect on the ratio of rate constants. For PFBX, the ratio is observed to decrease with increasing frequency. PFBS is the stronger surfactant, yet PFBA rates increased to a greater extent with increasing frequency.

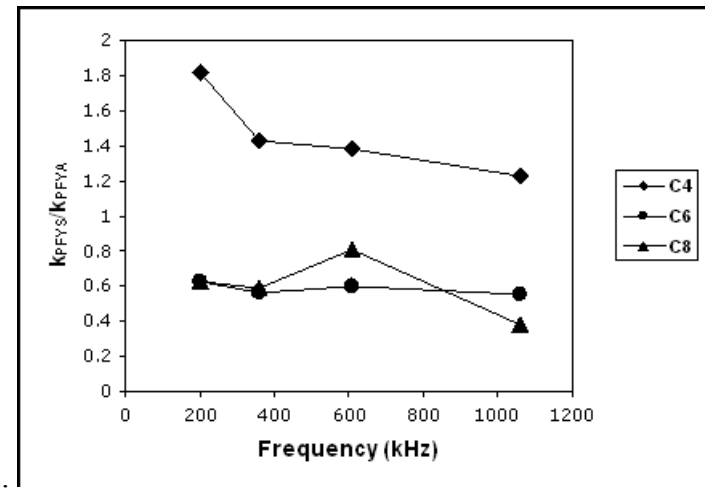

Figure 5. Frequency effects on the competitive adsorption of PFBX (♦), PFHX (●), and PFOX (▲), where X = A or S, on the bubble water interface.

The time-scale of bubble growth is short (μs) compared to the time required for the surfactants to equilibrate with the gas solution interface of the bubble (ms).[30] For example, at 47 kHz, a 2 mM aqueous sodium dodecyl sulfate (SDS), an anionic hydrocarbon surfactant, solution reached equilibrium with the air-water interface after >3 ms.[30,54] However, at f > 10 kHz, bubble radial oscillation velocities are much faster than chemical diffusion rates, $\nu_{bub,rad} >> \nu_{diffusion}$.[48] And once adsorbed to the air-water interface, strong surfactants such as SDS, have negligible diffusion rates away from the interface, $k_{desorb} = 500\ s^{-1}$ or $\tau_{1/2} > 1$ ms,[55] which is much longer than estimated bubble lifetimes 10-100 μs. Thus, once adsorbed to a cavitating bubble, strong surfactants such as SDS (PFOA has similar surfactant properties) are not expected to desorb over the bubble lifetime. Due to the large volume covered by the radial bubble oscillations, irreversible interfacial adsorption gives little room mass for transfer enhancements.

However, if a species was able to diffuse away from the bubble-water interface over a relevant time-scale, $(\ln 2)/k_{desorb} < 100$ μs, and mass transfer were sonochemically

mediated, $k_{adsorb} = k_{bub,osc,}$ mass transfer enhancements with increasing frequency can be rationalized. If the perfluoro-chemical were able to desorb during a non-transient, bubble compression phase, they could be re-adsorbed during the subsequent rarefaction phase. $K_{eq} = k_{adsorb}/k_{desorb}$, and if k_{adsorb} but not k_{desorb} is sonochemically enhanced, then an increase in K_{eq} would be expected. k_{adsorb} will increase with mounting frequency due to increased SA/V ratios and increased frequency of bubble oscillations per unit time. Sonochemical frequency dependences, Fig. 5, suggest this is active for the perfluorinated species with C_n-tail < 5 or K_{eq} < 50 M^{-1}, consistent with previous arguments (see Adsorption section) that PFBA is not hydrophobic enough to counteract coulombic repulsions of the headgroups and thus has a lower maximum surface concentration.

The apparent rate constants normalized to the PFOX rate constant, $k_{app}^{\text{-PFYS}} / k_{app}^{\text{-PFOS}}$ or $k_{app}^{\text{-PFYA}} / k_{app}^{\text{-PFOA}}$ vs. the equilibrium partitioning values, $K_{eq}^{\text{-PFYX}}$, for all 4 frequencies is plotted in Fig. 6. There is no correlation between the equilibrium partitioning constant until C_n-tail < 5 or $K_{eq}^{\text{-PFYX}} < 50$ M^{-1}. The equivalent normalized rate constants for C_n-tail > 5 suggest that under lightly populated bubble-water interface conditions, adsorption kinetics are sonochemically mediated. There is an apparent hydrophobic tail-length threshold for the sonochemical mediation of adsorption and, thus, degradation kinetics, a result of the inability of the shorter chains to form a stable surface film, due to their greater water solubility.

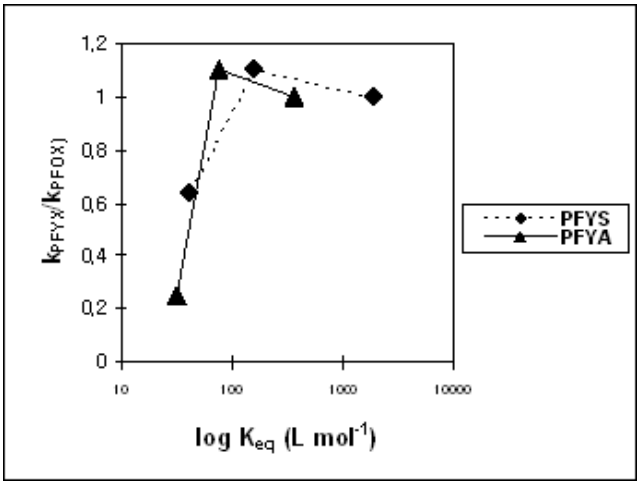

Figure 6. Apparent rate constants normalized to the PFOX rate constant vs. equilibrium partitioning values, $K_{eq}^{\text{-PFYX}}$.

Conclusions

The sonochemical efficiency of degradation is influenced by frequency effects and the adsorption behavior of the compounds based on their physical and chemical properties. Equilibrium bubble-surface partitioning was shown to have no effect on the C_6 and C_8 PFC sonolysis kinetics, with minor effect on PFBS, and large effects on PFBA. Furthermore, PFBA and PFBS experienced sono-enhanced sorption with increasing frequency. If surfactants do not reach equilibrium concentrations at the interface, then the rate of the reactions would depend on the fraction of compounds adsorbed at nucleation and the number of transiently cavitating bubbles in solution. In terms of frequency effects, PFHX and PFOX exhibit rate maximums at 358 kHz, and PFBX rate maximums were at 610 kHz. These results show that optimizing the degradation rates of perfluoro-chemicals of different chain lengths is dependent on the physical parameters controlling acoustic cavitation.

Acknowledgements

Research support and donation of analytical equipment from the 3M Environmental Laboratory is gratefully acknowledged. The author also wishes to thank Dr. Jie Cheng (Caltech), and Dr. Hyungwoong Park for their useful discussions and Dr. Nathan Dalleska of the Environmental Analytical Center for analytical assistance. Originally submitted for publication: Campbell, T.Y.; Vecitis, C.D.; Mader, B.M.; Hoffmann, M.R. Perfluorinated Surfactant Chain-Length Effects on Sonochemical Kinetics. *J. Phys. Chem. A*, **2009**, *36*, 9834-9842.

References

1. Key, B.D.; Howell, R.D.; Criddle, C.S. *Environ. Sci Technol*. **1997**, 31, 2445-2454.
2. 3M Company. Docket AR226-0547; *Office of Pollution Prevention and Toxics; US Environmental Protection Agency*: Washington D.C., **1999**.
3. Moody, C.A.; Field, J.A. *Environ. Sci. Technol*. **2000**, 34, 3864-3870.
4. Kärrman, A.; Ericson, I.; van Bavel, B.; Darnerud, P.; Aune, M.; Glynn, A.; Lignell, S.; Lindtröm, G. *Environ. Health. Persp*. **2007**, 115, 226-230.
5. Jones, P.D.; Hu, W.; Coen, W.D.; Newsted, J.L.; Giesy, J.P. *Environ. Tox. Chem.* **2003**, 22, 2639-2649.
6. Russell, M.H.; Berti, W.R.; Szosteck, B.; Buck, R.C. Environ. Sci. Technol. **2008**, 42, 800-807.
7. Van de Vijver, K.I.; Hoff, P.; Das, K.; Brasseur, S.; van Dongen, W.; Esmans, E.; Reijnders, P.; Blust, R.; De Coen, W. *Environ. Sci. Technol*. **2005**, 39, 6978-6984.
8. 3M Company. Docket AR226-0588; *Office of Pollution Prevention and Toxics; US Environmental Protection Agency*: Washington D.C., **1999**.
9. Chang, S.; Das K.; Ehresman, D.J.; Ellefson, M.E.; Gorman, G.S.; Hart, J.A.; Noker, P.E.; Tan, U.; Lieder P.H.; Lau, C.; Olsen, G.W.; Butenhoff, J.L. *Toxicol. Sci*. **2008**, 104, 40-53.
10. NICNAS, 2005. *Potassium perfluorobutanesulfonate. Existing chemical hazard assessment report*. Department of Health and Aging. National Industrial Chemical Notification and Assessment Scheme (NICNAS). Australian Government, Sidney. Australia.
11. Ochoa-Herrera, V.; Sierra-Alvarez, R. *Chemosphere* **2008**, 72, 1588-1593.

12. 3M Company. Docket AR226-1699; *Office of Pollution Prevention and Toxics; US Environmental Protection Agency*: Washington D.C., **1999**.

13. Oliaei, F.; Kriens, D.; Kessler, K. *Report to Senate Environment Committee*. **2006**.

14. CRC Handbook of Chemistry and Physics; CRC Press, Inc; Boca Raton, Fl, 1980; 61st Ed.

15. Hudlicky, M.; Pavlath, A.E. *Chemistry of Organic Fluorine Compounds II: A Critical Review*; ACS Chemistry; Washington, DC 1995.

16. Moriwaki, H.; Takagi, Y.; Tanaka, M.; Tsuruho, K.; Okitsu, K.; Maeda, Y. *Environ. Sci. Technol*. **2005**, 39, 3388-3392.

17. Vecitis, C.D.; Park, H.P.; Cheng, J.; Mader, B.T.; Hoffmann, M.R. *J. Phys. Chem. A*, **2008**, 112, 4261-4270.

18. Petrier, C.; Francony, A. *Wat. Sci. Tech*. **1997**, 35, 175-180.

19. Theron, P.; Pichat, P.; Guillard, C.; Petrier, C.; Chopin, T. *Phys. Chem. Chem. Phys.* **1999**, 4663-4668.

20. Colussi, A.J.; Weavers, L.K., ; Hoffmann, M.R. *J. Phys. Chem. A* **1998**, 102, 6927-6934.

21. Leighton, T. G. *The Acoustic Bubble*; Academic Press: London, 1994.

22. Suslick, K.S.; Hammerton, D.A.; Cline, R.E.; *J. Am. Chem. Soc*. **1986**, 108, 5641-5642.

23. Destaillats, H.; Hung, H; Hoffmann, M.R. *Environ. Sci Technol*. **2000**, 34, 311-317.

24. Hung, H.; Hoffmann, M.R. *J. Phys. Chem. A.* **1999**, 103, 2734-2739.

25. Kotronoreau, A.; Mills, G.; Hoffmann, M.R. *J. Phys. Chem*. **1991**, 95, 3630-3638.

26. Hua, I.; Hoffmann, M.R. *Environ. Sci. Technol*. **1997**, 31, 2237-2243.

27. Sostaric, J.Z., Riesz, P. *J. Phys. Chem. B*. **2002**, 106, 12537-12548.

28. Tronson, R.; Ashokumar, M.; Grieser, F. *J. Phys. Chem B*. **2003**, 107, 7307-7311.

29. Fyrillas, M.; Szeri, A.J. *J. Fluid Mech*. **1996**, 311, 361-378.

30. Sostaric, J.Z.; Riesz, P. *J. Am. Chem. Soc*. **2001**, 123, 11010-11019.

31. Ashokumar, M.; Hodnett, M.; Zeqiri, B.; Grieser, F.; Price, G.J. *J. Am. Chem. Soc*. **2007**, 129, 2250-2258.

32. Vecitis, C.D.; Park, H.P.; Cheng, J.; Mader, B.T.; Hoffmann, M.R. *J. Phys. Chem. C*, **2008**, 112, 16850-16857.

33. Cheng, J.; Vecitis, C.D.; Park, H.; Mader, B.T.; Hoffmann, M.R. *Environ. Sci. Technol*. Submitted April **2008**.

34. Markham, G.D/; Bock, C.L.; Bock, C.W. *Struct. Chem*. **1997**, 8, 293-307.

35. Guthrie, J.P.; Stein, A.R.; Huntington, A.P. *Can. J. Chem.* **1998**, 76, 929-936.

36. Israelachvili, J.N.; *Intermolecular and Surface Forces: with Applications to Colloidal and Biological Systems*; Academic Press, Orlando, Fl. 1985.

37. Simister, E.A.; Lee, E.M.; Lu, J.R.; Thomas, R.K.; Ottewill, R.H.; Rennie, A.R.; Penfold, J. *J. Chem. Soc. Faraday Trans*. **1992**, 88, 3033-3041.

38. Zhang, G.; Hua, I. *Environ. Sci. Technol*. **2000**, 34, 1529-1534.

39. Colussi, A.J.; Hung, H.; Hoffmann, M.R. *J. Phys. Chem. A*. **1999**, 103, 2696-2699.

40. Okitsu, K.; Ashokumar, M.; Grieser, F. *J. Phys. Chem*. **2005**, 109, 20673-20675.

41. Wayment, D.G.; Casadonte, D.J. *Ultrason. Sonochem*. **2002**, 9, 189-195.

42. Ciawi, E.; Rae, J.; Ashokumar, M.; Grieser, F. *J. Phys. Chem. B* **2006**, 110, 13656-13660.

43. Price, G.; Ashokumar, M.; Grieser, F. *J. Am. Chem. Soc*. **2004**, 126, 2755-2762.

44. Beckett, M.A.; Hua, I. *J. Phys. Chem. A.* **2001**, 105, 3796-3802.

45. Petrier, C.; David, B.; Laguian, S. *Chemosphere*. **1996**, 32, 1709-1718.

46. Alegria, A.; Lion, Y.; Kondo, T.; Riesz, P. *J. Phys. Chem*. **1989**, 93, 4909-4913.

47. Okitsu, K.; Suzuki, T.; Takenaka, N.; Bandow, H.;Nishimura, R.; Maeda, Y. *J. Phys. Chem. B*, **2006**, 110, 20081-20084.

48. Eller, A.; Flynn, HG. *J. Acoust. Soc. of Am*. **1965**, 37, 493-503.

49. Ruiz, A.I.; Canals, A.; Hernandis,V. *J. Anal. Atom. Spect*., **1993**, 8, 109-113.

50. Mackay, D.; Shiu, W.Y.; Ma, K.C. *Illustrated Handbook of Physical-Chemical Properties and Environmental Fate of Organic Chemicals*; Lewis Publishers; Boca Raton, FL, 1993; Vol. III.

51. Cheng, J.Y.; Riesz, P. *Ultrason. Sonochem*. **2007**, 14, 667-671.

52. Langmuir, I. *J. Am Chem. Soc*. **1916**, 38, 2221.

53. Glockner, V.; Lunkwitz, K.; Prescher, D. *Tenside Surf. Det*. **1989**, 26, 6.

54. Fainerman, V.B. *Colloids and Surfaces*, **1991**, 57, 249-266.

55. Chang, C.H.; Franses, E.I. *Colloid Surface A*, **1995**, 100, 1-45.

56. Goss, K. *Environ. Sci. Technol.* **2008**, 42, 456-458.

57. Heckster, F.M.; Laane, R.; deVoogt, P. Rev. *Environ. Contam. Toxicol*. **2003,** 179, 99-121.

58. Environment Agency, 2004. *Environmental Risk Evaluation Report: Perfluorooctane sulphonate (PFOS).* Chemical Assessment Section. Wallingford, United Kingdom.

Chapter 2

Sonolysis of Perfluorinated Surfactants: Power and Dual Frequency Effects

Introduction

The fate of perfluorinated organic compounds in the aquatic environment is of great concern because of their persistence, bioaccumulation,[1] and toxicity.[2, 3] Perfluorination yields unique physical properties, such as chemical inertness, minimal coefficients of friction, and low polarizabilities, which makes them desirable for a wide variety of commercial applications.[4] Fluorochemicals (FCs), which include perfluoroalkylsulfonates and perfluorocarboxylates, are utilized in products such as Teflon and Scotchguard, and have been detected globally in the atmosphere, hydrosphere and biosphere. Their stability arises from their high bond strength (450-530 kJ mol^{-1}) and low polarizabilities.[5] Current remediation strategies are slow (or ineffective) toward perfluorinated contaminants due to their oxidative stability. Therefore, it is of importance to develop effective remediation processes to address the environmental issue of widespread perfluorochemical contamination and persistence.

The efficient decomposition of organic compounds using ultrasound irradiation is a viable technology in the remediation of environmentally persistent and recalcitrant compounds such as perfluorinated chemicals (PFCs). Ultrasound irradiation produces high-energy chemistry in a very short timescale (~nanoseconds). During irradiation, a population of newly formed gas bubbles are excited to a resonant radius via rectified diffusion. This is followed by the absorption of energy during the rarefaction cycle of the ultrasonic waves causing their growth to a maximum size followed by an adiabatic collapse. The intense collapse generates average vapor temperatures near 5000 K [6, 7] and pressures on the order of several hundred atmospheres.[8] These high temperature and pressure conditions are sufficient enough to pyrolyze perfluorinated surfactants, which

are localized at the interfacial region of the cavitation bubble, to their inorganic substituents.[9]

In the present paper, power density, single- and dual-frequency effects are used to evaluate rates of degradation and the energy efficiency in the remediation of perfluorochemicals. An increase in power density leads to a linear increase in the sonochemical degradation kinetics of perfluorinated surfactants. However, the intensity and energy efficiency in the acoustic field is dependent on the frequency value and on the presence of either dual- or single- frequency exposure. The effect that these parameters have on cavitation bubble dynamics under ultrasonic irradiation will be discussed.

Materials and Methods

Perfluorobutyric acid (PFBA), perfluorohexanoic acid (PFHA), and perfluorooctanoate (PFOA) were purchased from Sigma Aldrich. Potassium perfluorobutane-1-sulfonate (PFBS), potassium perfluorohexane-1-sulfonate (PFHS), and potassium perfluorooctane-1-sulfonate (PFOS) were provided by 3M. Ammonium acetate (> 99%) and methanol (HR-GC > 99.99%) were obtained from EMD Chemicals Inc. Aqueous solutions were prepared with purified water using a Milli-Q system (18.2 mΩ cm resistivity). Acid solutions were brought to a pH of 7 by addition of ammonium hydroxide.

Sonication at single frequency exposures of 202, 358, and 610 kHz were performed for power densities at 83, 167, 250, and 333 W L^{-1} using an Allied Signal – Elac Nautik ultrasonic transducer with the solution contained in a 600 mL jacketed glass reactor. Dual frequency exposures at 20 + 202 and 20 + 610 kHz under an applied power density of 250 W L^{-1} were carried out using a 20 kHz horned transducer placed

perpendicular to an Allied Signal – Elac Nautik ultrasonic tranducer with the solution contained in a 600 mL jacketed glass reactor. The temperature was modulated with a Haake A80 refrigerated bath maintained at 10 °C. All reactions were sparged with argon for at least 30 minutes prior and during the reaction, unless otherwise noted. PFBS and PFBA were sonicated simultaneously at total initial concentrations of 300 and 470 nM, respectively. PFHS and PFHA were sonicated simultaneously at initial concentrations of 230 and 320 nM, respectively. Under varying power densities and single frequency exposures of either 358 or 610 kHz, PFOS and PFOA were sonicated simultaneously at initial concentrations of 200 and 240 nM, respectivly. PFOS and PFOA concentrations were 200 and 240 nM, respectively, under dual frequency conditions.

PFBS, PFBA, PFHS, PFHA, PFOS and PFOA were analyzed using HPLC-MS. The samples were placed into 750 μL polypropylene autosampler vials and sealed with a PTFE septum crimp cap. 20 μL of collected or diluted sample was injected onto an Agilent 1100 LC for separation on a Betasil C18 column (Thermo-Electron) of dimensions 2.1 mm ID, 100 mm length and 5 μm particle size. A 2 mM aqueous ammonium acetate/methanol mobile phase at a flow rate of 0.75 mL min^{-1} was used with an initial 70:30 water/methanol composition. HPLC effluents were analyzed with an Agilent Ion Trap MS in the negative ion mode for the perfluorooctanesulfonate molecular ion (m/z = 499), the perfluorohexanesulfonate molecular ion (m/z = 399), the perfluorobutanesulfonate molecular ion (m/z = 299), the decarboxylated perfluorooctanoate molecular ion (m/z = 369), the decarboxylated perfluorohexanoate molecular ion (m/z = 269) and the decarboxylated perfluorobutanoate molecular ion (m/z = 169). The nebulizer gas pressure was 40 PSI, while the drying gas flow rate and

temperature were 9 L min^{-1} and 325 $^{\circ}C$, respectively. The capillary voltage was set at +3500 V and the skimmer voltage was – 15 V. Quantification was completed by first producing a calibration curve using 8 concentrations between 1 ug L^{-1} and 200 ug L^{-1} fitted to a quadratic with X^{-1} weighting.

Results

The rate of degradation of PFHX (where X = c(A)rboxylates or (S)ulfonates) and PFBX at 202 and 610 kHz were evaluated at power densities from 83 W L^{-1} to 330 W L^{-1}. PFOX rates were evaluated at the same power densities, but at frequencies of 358 and 610 kHz. Plots of the pseudo first-order rate constants, k, versus the input power density are shown in Figures 1a-c for PFHX, PFBX, and PFOX, respectively. A gain in power density will amplify sonochemical effects. This is reflected in the measured rate constants which show linear increases with increasing power density. However, at 202 kHz, PFBA deviates from the trend in which the maximum rate constant is 0.035 min^{-1} at 250 W L^{-1} and subsequently decreases to ~0.032 min^{-1} at 330 W L^{-1} (Figure 1a).

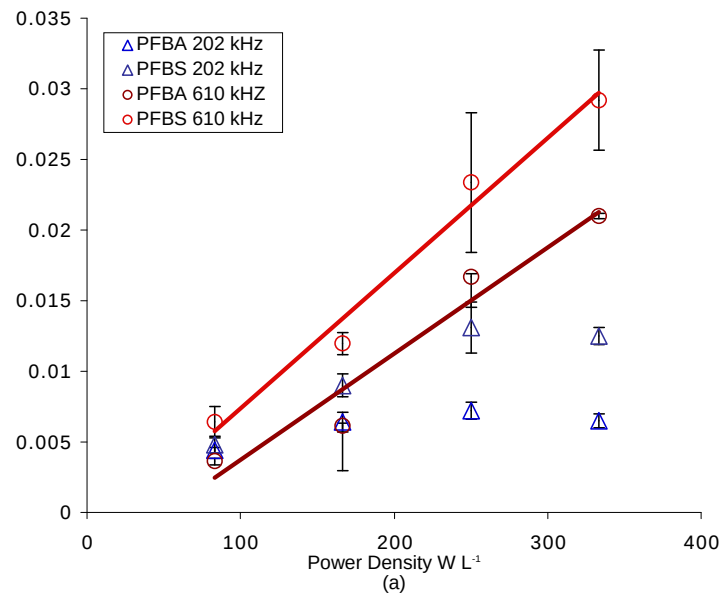

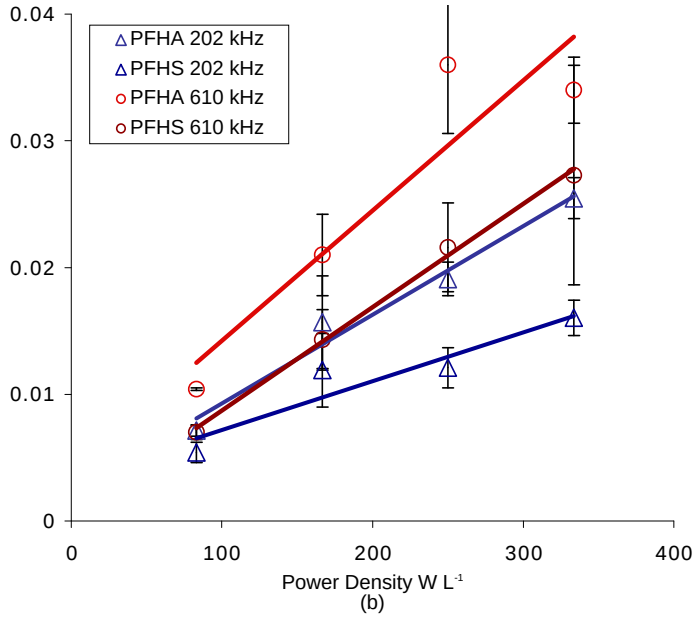

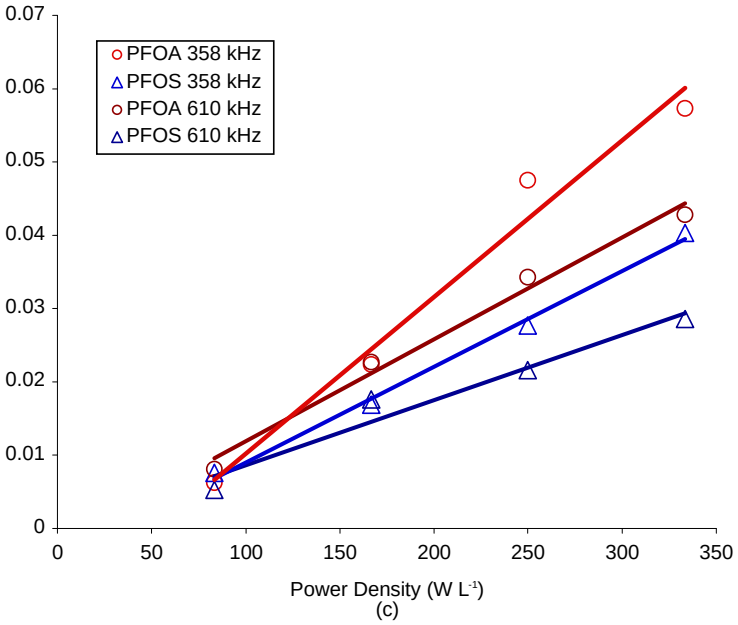

Figure 1. Rate constant dependence on power densities 83, 166, 250, and 333 W L^{-1} at 202 and 610 kHz, 10 °C, Ar for (1a) PFHX, (1b) PFBX and (1c) PFOX.

The effects of frequency and applied power density on the degradation rate of perfluorinated surfactants (C_n > 5) were explored in order to obtain optimal physical parameter conditions. The pseudo first-order rate constant, k, versus power density and frequency is shown in Figure 2a and 2b. For each frequency, power was varied from 83 to 333 W L^{-1}. From the 3-D plot, the power density value of 333 W L^{-1} and ultrasonic frequencies of 358 kHz and 618 kHz for PFYA (where Y = (O)ctane or (H)exane) and PFYS, respectively, are the most effective for C_n > 5 rates of degradation.

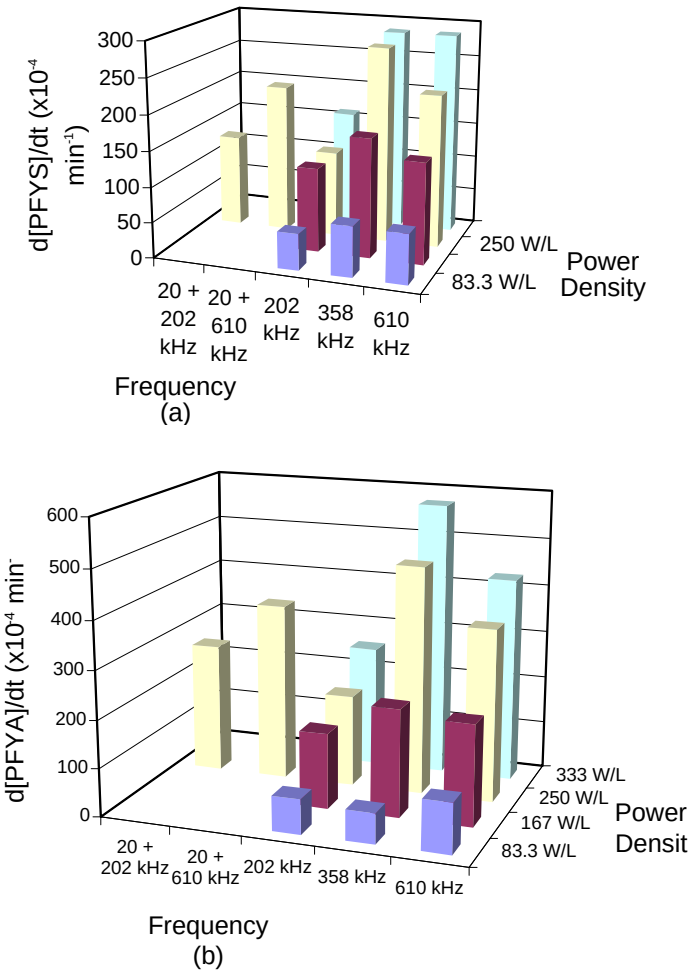

Figure 2. Effects of power density and frequency on the pseudo-first order rate constants for C_n > C_4 degradation for (2a) PFYS and (2b) PFYA.

Figure 3 shows single- and dual- frequency degradation effects for PFOA and PFOS. While there was no relative enhancement in degradation under 20 + 610 kHz dual frequency exposure compared to single frequency exposure at 610 kHz, there were 12 % PFOS and 23 % PFOA enhancements in degradation rates when a 20 kHz horned transducer was placed perpendicular to a 202 kHz sonochemical reactor compared to single frequency exposure at 202 kHz. The increase in degradation may be attributed to better overlap of acoustic waves, leading to an enhancement of cavitational effects and induction of sonochemical reactions. The overlapping waves may produce a non-sine ultrasonic wave form that enhances bubble expansion and shortens collapse time.

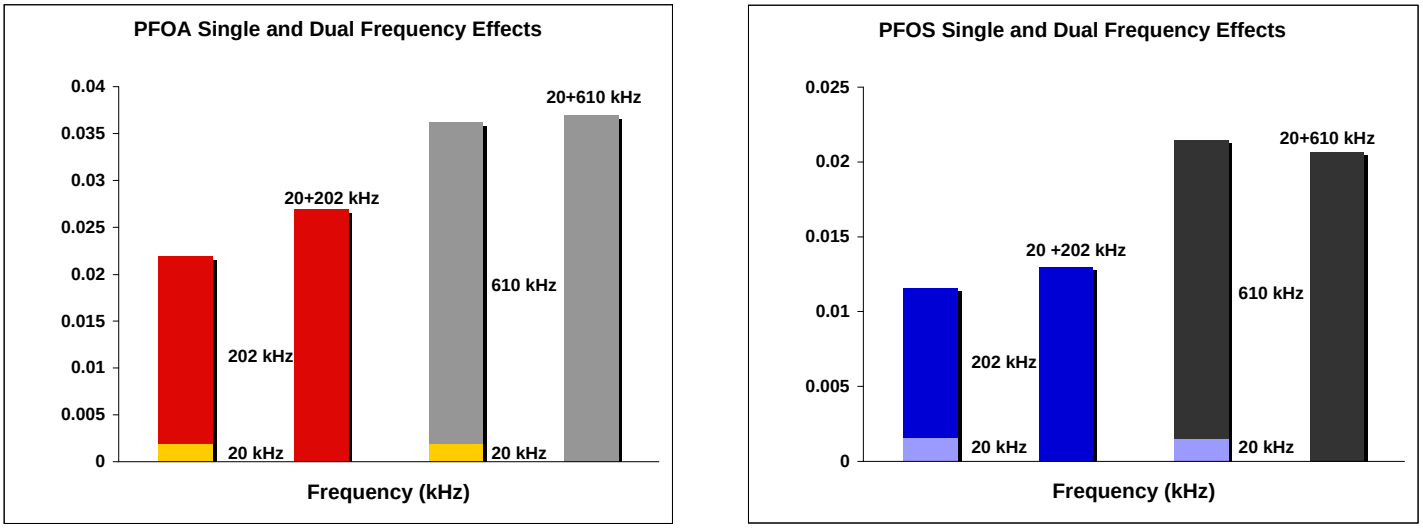

Figure 3. Single- and dual-frequency degradation effects for a) PFOA and b) PFOS. The 20 kHz columns represents single frequency exposure at 20 kHz and at either 205 or 618 kHz separately. The 20 + 205 kHz columns and the 20 + 618 kHz columns represent dual frequency or simultaneous exposure.

Discussion

Effects of Ultrasonic Power Density

Correlations between increases in power density and sonochemical reaction rates have been observed in a number of studies. Kang et al. observed an increase in methyl *tert*-butyl ether degradation with increasing power density up to 250 W L^{-1}.[10] Hua et al. showed a proportional increase in the degradation of *p*-nitrophenol with increasing power-to-volume ratio over the range of 0.98-7.27 W cm^{-3} in a parallel-plate, near-field reactor.[11] Suri et al. revealed increases in estrogen degradation rates with an increase in power intensity, finding that the 4 kW ultrasound reactor was more energy efficient than 0.6 and 2 kW sonicators.[12] Finally, Chen et al. found that reducing the reaction volume, or increasing the average ultrasonic power density, would lead to an enhancement in reaction rate of phenol and chlorophenol degradation, especially when used in conjunction with a photocatalysis in the presence of Hombikat TiO_2 suspensions.[13]

With the exception of PFBX at 202 kHz and 333 W L^{-1}, enhancements in PFYX degradation occurs with increasing sonication power density (Figures 1a-1c). Two reasons for the predominant linear correlations between sonochemical reactions and applied power is that increases in power density can increase the number of active cavitation bubbles and also the size (R_{max}) of the individual bubbles.[14, 15] Increases in R_{max} results in greater maximum collapse temperatures and sonochemical activity due to the conversion of the higher potential energy available into chemical reactions, heat, light and sound emissions during collapse.[15] Furthermore, rectified diffusion is know to increase with acoustic power, shifting the bubble size distribution.[16] Sonochemical

activity is enhanced if the previous bubble population was primarily composed of exceedingly small bubbles that resisted expansion due to strong surface tension (but under heavily-applied acoustic power), grow via rectifed diffusion to a size that responds rapidly to the rarefaction wave, and subsequently experience runaway expansion in just one cycle. The new bubble population could also be composed of bubbles that are less than the dynamic limit, but reach R_{max} faster due to enhanced rates of rectified diffusion. However, a drawback could be the growth of bubbles so large that there is insufficient time for collapse before the end of the pressure cycle. Out of such populations, there are those in which collapse occurs at another cycle, or if $P_A = P_H$, then the bubble may never undergo transient collapse.[17] However, shifts in bubble size distribution at a certain applied power is affected by frequency. While higher frequencies can shift the system to a more active bubble population, it requires higher power levels to produce transient bubbles with T_{max} values, comparable to values at lower frequencies due to decreased growth and collapse times. Further, frequency effects will be discussed later in the frequency section of this paper.

Another reason for the linear correlation between rate and power density is that increased power results in an enhancement of chemical effects brought on by increased mixing intensity, due to the turbulence produced from cavitational effects. In the degradation kinetics of heterogeneous reactions there are three steps: 1) mass transfer of the reactant to the bubble-water interface, 2) adsorption onto the bubble surface, and 3) chemical reaction at the surface.[18] The rate-limiting step influences the k_{obs} value. In evaluating reaction rate trends according to energy input into the system, the power density data distinguishes between mass transport and reaction-limited kinetics.[18]

According to the data in Figures 1a-1c, the linear increase in PFYX rates may reflect mass transport limited kinetics, while the non-linear behavior of PFBX at 202 kHz may reflect both mass transport and reaction-limited kinetics (Figure 1a).

Non-linear decreases in reaction rates at higher power densities have been attributed to a decrease in the efficiency of energy transfer to solution with input energy lost as heat,[18, 19] the scattering of ultrasound waves by bubble clouds,[20-24] or Bjerknes forces decreasing the distance between bubble clusters and the promotion of bubble-bubble coalescence leading to a smaller number of transient bubbles (Figure 1b).[25, 26] Secondary Bjerknes forces are proportional to the square of the sound pressure,[25] with bubbles smaller than resonance size collecting at the pressure antinodes and those larger than resonance aggregating at the pressure nodes.[26]

Because the majority of the PFYX rates show continued increases with power density under the same conditions, inefficient energy transfer, wave scattering, or Bjerknes forces are not the primary reason for the decrease in degradation rates for PFBX at 202 kHz, 333 W L^{-1}. Alternatively, reaction-limited kinetics in conjunction with low surface activity [27] may explain the decrease, revealing the constraints that physical parameters such as power and frequency have on the bubble dynamics. To understand this effect, we must discuss the relationship between power intensity and frequency in influencing the catalytic environment in terms of bubble size and bubble population (transient vs. stable) present in solution that can catalyze the physico-chemical decomposition of perfluorinated surfactants.

Power intensity controls the cavitation bubble size, bubble collapse time, the transient temperature, and the internal pressure in the cavitation bubble during collapse.

The power intensity is proportional to the power density and is related to the acoustic amplitude P_A (eq.1):

$$I = P_A^2/2\rho c \quad (1)$$

Where I is the sound intensity (amount of energy flowing per unit area, per unit time), ρ is the density of the medium, and c is the velocity of sound in the medium. At high intensities, a small vapor bubble may grow through inertial effects. Lower intensities induce growth via rectified diffusion in which the bubble will grow over many acoustic cycles. Diffusion of gas or vapor in or out of the bubble depends on the slightly larger surface area during expansion compared to bubble compression making bubble growth larger during expansion. When the bubble has reached its critical size, R_0, also known as resonance size, it is able to absorb ultrasound energy and grow rapidly to a size R_{max} during a single cycle of sound. At R_{max}, the bubble can no longer efficiently absorb energy. Unable to sustain itself, the bubble collapses, generating a high temperature and pressure environment that promotes physico-chemical reactivity.

R_{max} is the maximum radius a bubble can attain prior to cavitational collapse, and is dependent on the density of the liquid, the applied frequency, the hydrostatic pressure, and the acoustic pressure according to the following equation [17] (eq. 2):

$$R_{max} = \frac{4}{3\omega_a}(P_A - P_H)\left(\frac{2}{\rho P_A}\right)^{1/2}\left[1+\frac{2}{3P_H}(P_A - P_H)\right]^{1/3} \quad (2)$$

where ω_a is the applied acoustic frequency and P_H is the external (hydrostatic) pressure (= 1 atm). Furthermore, the bubble collapse time, τ, is proportional to the maximum bubble size R_{max} by [17]:

$$\tau = 0.915 R_{max}(\rho/(P_{H+}P_a)^{1/2}(1+P_{vg}/P_m) \quad (3)$$

where $P_H + P_a$ is the pressure in the liquid and P_{vg} is the vapor pressure in the bubble.

Bubble sizes are constrained by a dynamic radial limit for acoustic cavitation,[26] in which bubbles undergoing cavitational growth must have initial sizes $\leq R_{max}/2.5$ (Table 1). The bubble population present able to grow at 202 kHz is approximately 3 times larger than the bubbles at 610 kHz (R_{max} is inversely proportional to frequency). At high acoustic intensities with large values in P_A, the cavitation bubbles grow during the rarefaction cycle to very large R_{max} values, but are unable to undergo complete collapse during the compression phase due to insufficient collapse times. Therefore, these bubbles are not transient, and continue to either oscillate under stable cavitation conditions, or grow large enough to escape from the liquid through buoyancy and mass convection. The results for PFBX (202 kHz and 333 W L^{-1}) in Figure 1a reflect the predictions by the equations above, showing that there is an optimum power density that works in synergy with frequency to attain maximum rates of sonochemical degradation. For the other data, as discussed in Campbell et al., enhanced mass transfer effects at higher frequencies for C_4, and greater surface activity for longer chain surfactants ($C_n > 5$) are factors that help to overcome a less active bubble population in solution.[27]

Table 1. Dynamic Limit to Caviation Values Rmax/2.5 (μM).

P_A (atm)	Frequency (kHz)	Rmax (μM)	Rmax/2.5 (μM)
2.5	202	17.9	7.16
2.5	358	10.1	4.00
2.5	610	5.96	2.38
3.5	202	27.5	11.0
3.5	358	15.7	6.26
3.5	610	9.14	3.66
4.4	202	35.5	14.2
4.4	358	20.3	8.1
4.4	610	11.8	4.72
5.1	202	41.7	16.7
5.1	358	24.0	9.59
5.1	610	13.9	5.56

Effects of Ultrasonic Single Frequencies

Several studies evaluating the single frequency degradation of perfluorinated surfactants under a diverse set of conditions have been reported recently. Moriwaki et al. investigated the rates, products and possible mechanisms involved in the sonochemical decomposition of PFOS and PFOA in aqueous solutions.[28] Their studies were followed by Vecitis et al., who provided a detailed study of the high-temperature, gas-phase kinetics and mechanisms of PFOS and PFOA mineralization at optimal frequency and power density values over a wide range of concentrations (10 nM to 10 μM).[9] Vecitis et al. further investigated the concentration-dependent effects of PFOA and PFOS over concentrations of 20 nM to 200 μM, developing a Langmuir-Hinshelwood formalism to describe sonochemical adsorption mechanisms of PFOA and PFOS to the bubble-water interface.[29] Three subsequent matrix studies on PFOS and PFOA were performed. First, Cheng et al. revealed a reduction in sonochemical degradation of PFOS and PFOA in landfill groundwater due to competitive adsorption by organic components in

environmental matrices.[30] However, combination of ozonation with sonolysis led to a recovery in the rate loss. Second, Vecitis et al. reported that the sonochemical degradation of aqueous dilutions of FC-600, aqueous fire fighting foam (AFFF), was minorly effected by the components present in the AFFF matrix.[31] Third, Cheng et al. evaluated the effects of various inorganic species on PFOS and PFOA sonochemical kinetics, showing ion-concentration dependent Hofmeister and pH effects on degradation rates.[32] Finally, to examine the effects of chain length on sonochemical degradation, Campbell et al. compared the kinetics and adsorption behavior of PFHA, PFHS, PFBA, PFBS, PFOA, and PFOS at varied frequencies, showing that C_6 and C_8 rates were controlled by the number of cavitation events per unit time and that C_4 kinetics were influenced by mass transfer to the bubble-water interface.[27]

In studying how frequency influences bubble dynamics, we must first discuss how mass, momentrum and energy conservation govern the bubble motion dynamics in a liquid medium. Bubble motion dynamics is described by the following Rayleigh-Plesset non-linear ordinary differential equation (eq 4):

$$RR'' + \frac{3}{2}R'^2 = \frac{1}{\rho}[(P_0 + \frac{2\sigma}{R_0} - P_v)(\frac{R_0}{R})^{3\kappa} + P_v - \frac{2\sigma}{R} - P_0 - P_a(t)] \qquad (4)$$

where R (R_0) is the initial bubble radius, R' and R'' are its first and second derivatives, respectively. P_0 is the hydrostatic pressure, $P_a(t)$ is the acoustic forcing pressure, κ is the polytropic index of the vapors or gases, P_v is the water vapor pressure, ρ and σ are the density and surface tension, respectively. The Rayleigh-Plesset Equation describes the bubble's response to a time-varying pressure field, P(t), in which the superimposition of P(t) onto the hydrostatic constant pressure, P_0, changes the bubble radius, R_0, to a new value R(t), generating kinetic energy in the liquid. Despite bubble expansion, the surface

tension effect, $2\sigma/R_0$, confines the bubble size, such that it oscillates at each new equilibrium size. The equilibrium state is stabilized by the surface tension effect opposing the positive pressure of the liquid confining the gas present in the bubble. However, negative pressures counteract the confining pressures of the surface tension pressure. For very small bubbles operating on their own timescales at high resonance frequencies, pressure changes over low frequency timescales (much less than the bubble resonance) are felt by the bubble to be quasi-static.[26]

However, under an optimal driving frequency, bubble expansion is sustained through an extended and amplified rarefaction cycle, followed by a short collapse via a shortened compression stage. According to the following derivation, this process occurs when the bubble's natural resonance is equal to the applied ultrasonic frequency.[17] $P_a(t)$ is a sinusoidal wave of amplitude P_A and angular frequency ω according to the equation (eq. 5):

$$P_a(t) = -P_A \sin \omega t \qquad (5)$$

Neglecting vapor pressure and viscosity and under small amplitude oscillations, eq. 4 reduces to (eq. 6):

$$R_\varepsilon'' + \omega_0^2 R_\varepsilon = \frac{P_A}{\rho R_0} \sin \omega t \qquad (6)$$

where ω_0 is the resonance angular frequency given by (eq. 7):

$$\omega_o^2 = \frac{1}{\rho R_o^2}[3\kappa(P_o + \frac{2\sigma}{R_o}) - \frac{2\sigma}{R_o}] \qquad (7)$$

since the resonance frequency $f_0 = \omega_0/2\pi$, then by neglecting surface tension terms, it is inversely proportional to R_0 and equation 6 becomes:

$$R_{\varepsilon}(t) = \frac{P_A}{\rho R_o(\omega^2 - \omega_0^2)}[\sin\omega t - \frac{\omega}{\omega_0}\sin\omega_0 t] \qquad (8)$$

When $\omega \approx \omega_0$ and the initial bubble radii is smaller than a certain critical value, $R_{0,\,crit}$, then optimal forcing (rarefaction wave) leads to runaway expansions of the responding bubble beyond the constraints of the linearized formula of Equation 4 in just one cycle. Bubbles with $R_0 > R_{0,\,crit}$ will oscillate a few times before collapsing. Thus, the range of bubble sizes susceptible to transient cavitation are dependent on frequency as a parameter.

In previous studies, perfluoroalkylsulfonates were determined to be stronger surfactants compared to perfluoroalkylcarboxlyates but with slower rates of degradation due to the energy of activation required in breaking the bond between the carbon-carboxylate vs carbon-sulfonate moieties.[9] In Figure 2, PFYX exhibit a minimum of 19 % enhancements in degradation rates with increasing power density at each frequency, with the exception of PFYS at 358 kHz. Although the sonolytic rate maxima is mediated by the number of cavitation events per unit time at 358 kHz, increasing the power density from 250 W L^{-1} to 333 W L^{-1} increases the reaction rate only 3 %. According to Hung et al., this can be attributed to a decrease in the efficiency of energy transfer to solution at higher power densities due to a greater loss of input energy as heat.[19] Interestingly, PFYS show identical rates of degradation at 358 kHz and 618 kHz under an applied power density of 333 W L^{-1} which indicates that despite the possible loss of input energy at higher power, there is a 30 % enhancement in degradation at 618 kHz from 250 to 333 W L^{-1}. The increase in relative enhancement can be attributed to increased mass transfer effects brought on my the higher power intensity and higher frequency effects. Although, 358 kHz and 250 W L^{-1} is optimal conditions for longer chain surfactants ($C_n > 5$), [9, 29] the combination of increased mixing intensity at higher power densities[18, 19] and larger

surface-to-volume ratios at 610 kHz[18-20] enhances surfactant binding to the interfacial region. At higher frequencies, rectified diffusion is able to occur more rapidly because there are more acoustic cycles per unit time such that there is a greater distribution of bubbles that can reach resonance size more quickly leading to an enhancement in sonolysis. Furthermore, surface tension which is inversely correlated with bubble radius, provides a collapsing force on the bubble.[33] For example, a 13.9 μm (610 kHz) bubble will experience a surface tension that is almost twice as large as a 24 μm (358 kHz) bubble at an acoustic pressure of 5.1 atm leading to a more complete collapse with higher temperatures.

Effects of Ultrasonic Dual Frequency

The theoretical goal of exploring a dual frequency system is to attain optimal driving conditions to produce large responses from the oscillating bubble that are multiples of the natural frequency, ω_0. Single sinewaves apply the same driving effort in rarefaction and compression even though the bubble collapse time is much shorter than the expansion. Under optimized dual frequency exposure, an optimal waveform will spend most of its efforts in rarefaction so that the bubbles can expand to their maximize size followed by a swift compression. Enhancements in the intensity of the collapse and differences in rates of rectified diffusion can lead to a greater number of cavitating bubbles.

Dual frequency reactors have been empirically shown to dramatically enhance the physical and chemical effects of ultrasound.[34, 35] The non-linear process of cavitation produces cavitating bubbles that emit sub- and higher-order harmonics. Taking advantage of this phenomenon, Umemura et al. developed an instrument that produced

second-harmonic superimpositions (SHS) of 0.75 MHz and 1.5 MHz that led to a ten fold increase in iodide oxidation rates.[34] Yasuda et al. observed an increase in fluorescence intensity of terephthalate ion for dual frequency in comparison to single frequency.[36] They also performed sonochemical luminescence experiments using luminol to show that the sonochemical reaction fields became more extensive in the reactor and more intensive around the center of the reactor.[36] Swamy et al. found that the simultaeneous application of frequencies at 20 and 40 kHz enhanced extraction rates of copper from oxide ores along with an increase in yields.[37] Brotchie et al. demonstrated a synergistic effect of enhanced sonoluminescence for 20 kHz and 355 kHz and 20 kHz and 1056 kHz when low power was applied to the higher frequency.[38]

Under the application of identical power, Figure 3 provides a comparison in decomposition rates for PFYX at 20 + 202 and 20 + 610 kHz vs single frequency exposure at either 202 or 610 kHz, respectively. 12 % PFOS and 23 % PFOA enhancements in degradation rates were observed when a 20 kHz horned transducer was placed perpendicular to a 202 kHz sonochemical reactor. As mentioned previously, the synergism in dual frequency application is believed to induce the cavitation efficiency via deformation of a sinusoidal waveform.[34, 35] The modification of the rarefaction and compression mechanisms leads to a more effective bubble growth, resulting in a more intense collapse.[34, 35] Kawabata et al. suggested that the amplitude of the acoustic field is a function of the fundamental and second-harmonic (eq. 9):

$$P_a(r,t) = P_{a(1)}(r)\sin(\omega t + \phi_1(r)) + P_{a(2)}(r)[\sin(2(\omega t + \phi_1(r))) + \Delta\phi(r)]^{34, 35} \quad (9)$$

where $P_a(r,t)$ is the acoustic pressure at point r at time t and $P_{a(1)}(r)$ and $P_{a(2)}(r)$ are the amplitudes of the fundamental and second harmonic at point r, respectively. ω is

the angular frequency of the fundamental, $\phi_1(r)$ the phase of the fundamental at point r and $\Delta\phi(r)$, the phase of the second harmonic relative to the fundamental. Furthermore, second harmonic superimposition is sensitive to the relative phase $\Delta\phi$, showing that the enhancement of cavitation and induction of sonochemical reactions is not a sum of independent effects but a synergistic result between the acoustic waveforms.[34, 35] Thus, the ultrasound frequencies closer in value at 20 + 202 kHz provides better overlap of wave forms than 20 + 610 kHz exposure, leading to enhanced sonochemical activity. Modification of the acoustic field increases the wave amplitude, producing higher temperature and pressures upon collapse. Furthermore, accelerated mass transfer effects, enhanced hydrodynamic forces and increases in the bubble population present in solution may also occur under a dual frequency environment.

Energy Efficiency

The energy efficiency of the various ultrasound conditions used in this study was evaluated to determine the practical potential for applying the aforementioned conditions toward the remediation of perfluorinated surfactants. Hua et al. evaluated the energy efficiency of a sonochemical system by calculating the G value, the number of molecules degraded per unit of energy input into the system.[11]

$$\text{G value} = \Delta C N_o V / \Delta T W \text{ [molecules } k^{-1}\text{]}^{11, 39} \quad (10)$$

Where ΔC is the change in the solute concentration over a given time interval ΔT; N_o = 6.023×10^{23} molecules/mol; V is the volume of the solution; W is the voltage. The G values represents a lower limit of energy efficiency in the reactor since the energy transduction process is not 100 % efficient.[11] The energy efficiencies in terms of the

energy required to degrade PFOS and PFOA under varying power densities at single and dual frequencies are listed in Tables 2-5.

Table 2. Comparison of Energy Efficiencies between single and dual frequency systems (202 and 610 kHz) for the degradation of PFC's.

	Power (W) Volume (L)	k (min^{-1})	Concentration (nM)	G value x 10^{13} (molecule kJ^{-1})
$f_{202\ kHz,PFOA}$	150 600	0.020 min^{-1} $t_{1/2}$ = 35 min	240	14
$f_{202+20\ kHz,PFOA}$	150 600	0.027 min^{-1} $t_{1/2}$ = 26 min	240	19
$f_{610\ kHz,PFOA}$	150 600	0.034 min^{-1} $t_{1/2}$ = 20 min	240	24
$f_{610+20\ kHz,PFOA}$	150 600	0.037 min^{-1} $t_{1/2}$ = 19 min	240	25
$f_{202\ kHz,PFOS}$	150 600	0.01 min^{-1} $t_{1/2}$ = 69 min	200	6
$f_{202+20\ kHz,PFOS}$	150 600	0.013 min^{-1} $t_{1/2}$ = 53 min	200	8
$f_{610\ kHz,PFOS}$	150 600	0.02 min^{-1} $t_{1/2}$ = 35 min	200	11
$f_{610+20\ kHz,PFOS}$	150 600	0.021 min^{-1} $t_{1/2}$ = 33 min	200	12

Table 3. Comparison of Energy Efficiencies of PFBX degradation at varying power input (50 W, 100 W, 150 W, 200 W) and frequencies (205 and 610 kHz).

	Power (W) Volume (L)	k (min^{-1})	Concentration (nM)	G value x 10^{13} (molecule kJ^{-1})
$f_{202\ kHz,\ PFBA}$	50	0.0044	470	6
	600	$t_{1/2}$ = 158 min		
$f_{202\ kHz,\ PFBA}$	100	0.0064	470	9
	600	$t_{1/2}$ = 108 min		
$f_{202\ kHz,\ PFBA}$	150	0.0072	470	7
	600	$t_{1/2}$ = 96 min		
$f_{202\ kHz,\ PFBA}$	200	0.0065	470	9
	600	$t_{1/2}$ = 107 min		
$f_{610\ kHz,\ PFBA}$	50	0.0037	470	5
	600	$t_{1/2}$ = 187 min		
$f_{610\ kHz,\ PFBA}$	100	0.0061	470	8
	600	$t_{1/2}$ = 114 min		
$f_{610\ kHz,\ PFBA}$	150	0.017	470	23
	600	$t_{1/2}$ = 41 min		
$f_{610\ kHz,\ PFBA}$	200	0.021	470	29
	600	$t_{1/2}$ = 33 min		
$f_{202\ kHz,\ PFBS}$	50	0.0048	300	4
	600	$t_{1/2}$ = 144 min		
$f_{202\ kHz,\ PFBS}$	100	0.009	300	8
	600	$t_{1/2}$ = 77 min		
$f_{202\ kHz,\ PFBS}$	150	0.013	300	11
	600	$t_{1/2}$ = 53 min		
$f_{202\ kHz,\ PFBS}$	200	0.013	300	11
	600	$t_{1/2}$ = 53 min		
$f_{610\ kHz,\ PFBS}$	50	0.004	300	3
	600	$t_{1/2}$ = 173 min		
$f_{610\ kHz,\ PFBS}$	100	0.006	300	5
	600	$t_{1/2}$ = 116 min		
$f_{610\ kHz,\ PFBS}$	150	0.017	300	15
	600	$t_{1/2}$ = 41 min		
$f_{610\ kHz,\ PFBS}$	200	0.021	300	18
	600	$t_{1/2}$ = 33 min		

Table 4. Comparison of Energy Efficiencies of PFHX degradation at varying power input (50 W, 100 W, 150 W, 200 W) and frequencies (205 and 610 kHz).

	Power (W) Volume (L)	k (min^{-1})	Concentration (nM)	G value x 10^{13} (molecule kJ^{-1})
$f_{202\ kHz,\ PFHA}$	50	0.007	320	7
	600	$t_{1/2}$ = 99 min		
$f_{202\ kHz,\ PFHA}$	100	0.016	320	15
	600	$t_{1/2}$ = 43 min		
$f_{202\ kHz,\ PFHA}$	150	0.019	320	18
	600	$t_{1/2}$ = 36 min		
$f_{202\ kHz,\ PFHA}$	200	0.025	320	23
	600	$t_{1/2}$ = 28 min		
$f_{610\ kHz,\ PFHA}$	50	0.010	320	9
	600	$t_{1/2}$ = 69 min		
$f_{610\ kHz,\ PFHA}$	100	0.021	320	20
	600	$t_{1/2}$ = 33 min		
$f_{610\ kHz,\ PFHA}$	150	0.036	320	34
	600	$t_{1/2}$ = 19 min		
$f_{610\ kHz,\ PFHA}$	200	0.034	320	32
	600	$t_{1/2}$ = 20 min		
$f_{202\ kHz,\ PFHS}$	50	0.005	230	3
	600	$t_{1/2}$ = 139 min		
$f_{202\ kHz,\ PFHS}$	100	0.012	230	8
	600	$t_{1/2}$ = 58 min		
$f_{202\ kHz,\ PFHS}$	150	0.012	230	8
	600	$t_{1/2}$ = 58 min		
$f_{202\ kHz,\ PFHS}$	200	0.016	230	11
	600	$t_{1/2}$ = 43 min		
$f_{610\ kHz,\ PFHS}$	50	0.007	230	5
	600	$t_{1/2}$ = 99 min		
$f_{610\ kHz,\ PFHS}$	100	0.014	230	9
	600	$t_{1/2}$ = 50 min		
$f_{610\ kHz,\ PFHS}$	150	0.022	230	14
	600	$t_{1/2}$ = 32 min		
$f_{610\ kHz,\ PFHS}$	200	0.027	230	18
	600	$t_{1/2}$ = 26 min		

Table 5. Comparison of Energy Efficiencies of PFOX degradation at varying power input (50 W, 100 W, 150 W, 200 W) and frequencies (358 and 610 kHz).

	Power (W) Volume (L)	k (min^{-1})	Concentration (nM)	G value x 10^{13} (molecule kJ^{-1})
$f_{358\ kHz,\ PFOA}$	50	0.0063	240	7
	600	$t_{1/2}$ = 110 min		
$f_{358\ kHz,\ PFOA}$	100	0.022	240	23
	600	$t_{1/2}$ = 32 min		
$f_{358\ kHz,\ PFOA}$	150	0.048	240	35
	600	$t_{1/2}$ = 14 min		
$f_{358\ kHz,\ PFOA}$	200	0.057	240	30
	600	$t_{1/2}$ = 12 min		
$f_{610\ kHz,\ PFOA}$	50	0.008	240	17
	600	$t_{1/2}$ = 87 min		
$f_{610\ kHz,\ PFOA}$	100	0.023	240	24
	600	$t_{1/2}$ = 30 min		
$f_{610\ kHz,\ PFOA}$	150	0.034	240	24
	600	$t_{1/2}$ = 20 min		
$f_{610\ kHz,\ PFOA}$	200	0.043	240	23
	600	$t_{1/2}$ = 16 min		
$f_{358\ kHz,\ PFOS}$	50	0.007	200	12
	600	$t_{1/2}$ = 99 min		
$f_{358\ kHz,\ PFOS}$	100	0.017	200	15
	600	$t_{1/2}$ = 41 min		
$f_{358\ kHz,\ PFOS}$	150	0.028	200	16
	600	$t_{1/2}$ = 25 min		
$f_{358\ kHz,\ PFOS}$	200	0.04	200	18
	600	$t_{1/2}$ = 17 min		
$f_{610\ kHz,\ PFOS}$	50	0.005	200	9
	600	$t_{1/2}$ = 139 min		
$f_{610\ kHz,\ PFOS}$	100	0.018	200	16
	600	$t_{1/2}$ = 39 min		
$f_{610\ kHz,\ PFOS}$	150	0.022	200	13
	600	$t_{1/2}$ = 32 min		
$f_{610\ kHz,\ PFOS}$	200	0.029	200	13
	600	$t_{1/2}$ = 24 min		

Generally, there is a linear increase in energy efficiency with increasing power density up to a certain value. Energy efficiency is also chain length dependent, with enhancements under dual frequency exposure. Comparison of G values in Tables 2 and 5 ([PFOA] = 240 nM, [PFOS] = 200 nM) show that increasing the acoustic power from 150 W to 200 W (Table 5) at a single frequency of 610 kHz does not improve the energy efficiency towards PFOX degradation. However, under simultaneous frequency of 20 + 610 kHz, there is a 4 - 9 % relative enhancement in energy efficiency. At acoustic powers of 150 and 200 W (f = 610 kHz), energy efficiency is on the order of PFBS ≥ PFHS > PFOS. For the carboxylates, PFHA is greater than PFOA, while PFBA is less than PFHA. Overall, increasing frequency and acoustic power improves energy efficiency for the less surface active chains. However, with the exception of PFOS (f = 358 kHz), increasing the acoustic power for the most surface active surfactants, PFOS and PFOA, does not lead to an enhancement in energy efficiency, with values maximizing at 150 W. Interestingly, improvement in energy efficiencies can occur through changing surfactant concentrations, with higher surfactant concentrations lead to better energy efficiency. According to values by Vecitis et al, G values for PFOA and PFOS are 1972 x 10^{13} and 154 x 10^{13} molecules kJ^{-1} ([PFOA] = 13,100 nM, [PFOS] = 14,000 nM, 250 W L^{-1}, 358 kHz).[29] Thus, effectively harnesses the ultrasound power towards sonolytic degradation of perfluorinated surfactants, means increasing the PFYX concentration until the cavitation sites approach saturation with increasing bulk solute concentration.[29] According to Sunartio et al, addition of charged surfactants to solution enhances sonochemical activity by affecting the structure of bubble clusters and gas solubility in solution.[25, 40] Although informative, the experiments were not conclusive as to the energy

efficiency at the level of the bubble population or bubble water interface but gave an overall measure of the efficency in the reactor design. Furthermore, while there are limitations to optimizing energy efficiency via frequency and power, other options include increasing surfactant concentration and the application of dual frequency sound waves.

Finally, the fast and nearly adiabatic collapse of a bubble converts the elastic potential energy into the internal energy of the bubble plus the kinetic energy of the liquid shell. The maximum temperature (T_{max}) and pressure (P_{max}) inside the bubble is (eq. 11 and 12):

$$T_{\max} = T_0\{\frac{P_m(\kappa-1)}{P}\} \quad (11) \qquad P_{\max} = P\{\frac{P_m(\kappa-1)}{P})\}^{\kappa/(\kappa-1)} \quad (12)$$

where T_0 is the ambient temperature, P is the pressure in the bubble at its maximum size, $P_m = P_0 + P_a$ is the constant external presure during the fast collapse (P_0 is the hydrostatic pressure and P_a is the acoustic pressure). However, the actual maximum temperature and pressures are constrained by the kinetic energy of the bubble liquid shell available and the work necessary to heat the vapor in the adiabatic stage. Depending on the power density and frequency, bubbles can undergo hundreds to thousands of oscillations. Decreases in pressure increases the water vapour that upon initial collapse condenses at the interface due to higher pressures but does not fully condense due to the enhanced speed at the final stage of compression. The amount of vapor trapped at the end of collapse may play a major role in T_{max} values and degradation rates. Colussi et al has shown that the endothermic atomization of water molecules represents a major contribution to the energy balance of the bubble, controlling the past phase of collapse.[41] Molecules

decompose thermally due to the extreme conditions created at the end of the bubble collapse. Water dissociates within a few μs above 3500 K[42]:

$$H_2O\ (g) \rightarrow H\ (g) + {}^{\bullet}OH\ (g)$$

The endothermic dissociation of water vapor ($\Delta H \sim 5 \times 10^5$ J/mol) has a net oxidizer production of 8.7×10^{-9} OH mol J^{-1} [33] at 513 kHz, 0.065 W cm^{-3} under an argon atmosphere (rates represent a lower limit of the true rate of OH production via thermolysis in the gas phase of the bubble). The experimental rate implies that only 0.45 % = 100 x (8.7×10^{-9} OH mol J^{-1} x 5.0×10^5 J mol^{-1}) of the applied ultrasound power is converted to sonochemical action. Furthermore, the thermal decomposition of ammonium perfluorooctanoate in water has an enthalpy of $\Delta H = 167$ kJ mol^{-1}.[43] If given a G value of 1972 molecules k J^{-1} (2.3×10^{-8} mol kJ^{-1})[29], then < 10^{-4} % = 100 x (2.3×10^{-8} mol kJ^{-1} x 167 kJ mol^{-1}) of the power density is used for the degradation of perfluorochemicals.

Thus, while optimal power density, frequency, and concentration values have been found for the ultrasound irradiation of perfluorinated surfactants,[9, 27, 29] further research endeavors should be directed toward optimization of dual frequency to dramatically intensify the physical and chemical effects of ultrasound. This would hopefully lead to greater energy efficiency of the ultrasonic process, making it more economically attractive for commercial applications. With the average price of electricity at 8.14 cents per kilowatt per hour, the cost of degrading 1 L of solution containing perfluorinated surfactants (358 kHz, 250 W L^{-1}, 10 °C, argon, ~200 nM PFOX) under single frequency exposure is approximately \$10 m^{-3} which is much greater than the \$0.25m^{-3} for conventional water treatment and \$2 m^{-3} for reverse osmosis. However,

implementing a dual frequency system that relies on the propagation of two waves of different frequencies, enhances sonochemical effects thereby decreasing the cost of sonochemistry by 23% making the price ~ \$7.5 m^{-3}. Although the enhancements prove less cost-effective than reverse osmosis, the results are preliminary and are not optimized in terms of perfluorinated surfactant concentration or for a system where the waveforms generated during dual frequency can undergo a maximum level of constructive interference to afford the greatest enhancements in sonochemical activity.

Conclusions

The evolution and fate of vapour – filled microbubbles in solution is a dynamic and complex process. Serving as catalytic reaction vessels, measureable chemical effects occur in bubbles undergoing large-amplitude asymmetric oscillations beyond the linear response, leading to intense temperatures and conditions that can pyrolyze perfluorinated surfactants. In this paper, reaction rates increase linearly with power density but eventually level off for less surface active surfactants such as PFBX at 202 kHz. Dual frequency exposure can enhance sonochemical activity by either halving the intensity threshold to decrease the power input necessary to produce the same bubble population or producing higher maximum radius values ($R_{max)}$, followed by shorter collapse times that can generate higher temperatures and pressures compared to single frequency exposure. Overall, variable parameters such as power density, single or dual frequency, and type of sonic field influences bubble dynamics and thermodynamics through the modification of bubble radii and population density which in turn can influence sonochemical rates of degradation and energy efficiency.

Acknowledgements

Research support and donation of analytical equipment from the 3M Environmental Laboratory is gratefully acknowledged. The authors also wish to thank Dr. Jie Cheng (Caltech), and Dr. Hyungwoong Park for their useful discussions and Dr. Nathan Dalleska of the Environmental Analytical Center for analytical assistance.

References

(1) Russell, M. H.; Berti, W. R.; Szosteck, B. Buck, R. C. *Environ. Sci. Technol.* **2008**, *42*, 800-807.

(2) Olsen, G. W.; Mair, D. C.; Reagen, W. K.; Ellefson, M. E.; Ehresman, D. J.; Butenhoff, J.L.; Zobel, L.R. *Chemosphere* **2007**, *68*, 105-111.

(3) 3M Company. *Sulfonated Perfluorochemicals in the Environment: Sources, Dispersion, Fate and Effects*; Docket AR226-0620; Office of Pollution Prevention and Toxics; U.S. Environmental Protection Agency: Washington, D.C., 2000.

(4) Key, B. D.; Howell, R. D.; Criddle, C. S. *Environ. Sci. Technol*. **1997**, *31*, 2445-2454.

(5) 3M Company. *The Science of Organic Fluorochemistry*; docket AR226-0547; Office of Pollution Prevention and Toxics, U.S. Environmental Protection Agency: Washington, D.C., 1999.

(6) Didenko, Y. T.; McNamara, W. B.; Suslick, K. S. *J. Am Chem. Soc.* **1999**, 121, 5817.

(7) Ciawi, E.; Rae, J.; Ashokumar, M.; Grieser, F. *J. Phys. Chem. B* **2006**, 110, 13656-13660.

(8) McNamara *J. Phys. Chem. B* **2003**

(9) Vecitis, C. D.; Park, H.; Cheng, J.; Mader, B. T.; Hoffmann, M. R. *J. Phys. Chem. A* **2008**, *112*, 4261-4270.

(10) Kang, J. W.; Hung, H. M.; Lin, A.; Hoffmann, M. R. *Environ. Sci. Technol.* **1999**, *33*, 3199-3205.

(11) Hua, I.; Hochemer, R. H.; Hoffmann, M. R. *Environ. Sci. Technol.* **1995**, *29*, 2790-2796.

(12) Suri, R. P. S.; Nayak, M.; Devaiah, U.; Helmig, E. *J. Haz. Mat.* **2007, *146*, 472-478.

(13) Chen, Y. C.; Smirniotis, P. *Ind. Eng. Chem. Res.* **2002**, *41*, 5958-5965.

(14) Barber, B. P.; Wu, C. C.; Lofstedt, R.; Roberts, P. H.; Putterman, S. J. *Phys. Rev. Lett.* **1994, *72*, 1380-

(15) Kanthale, P.; Ashokkumar, M.; Grieser, F. *Ultrason. Sonochem.* **2008**, *15*, 143-150.

(16) Crum, L. A. *J. Acoust. Soc. Am.* **1980**, *68*, 203-211.

(17) Mason, T. J. *Sonochemistry: theory, applications and uses of ultrasound in chemistry*; John Wiley & Sons: New York, 1988.

(18) Hung, H. M.; Ling, F. H.; Hoffmann, M. R. *Environ. Sci. Technol.* **2000**, *34*, 1758-1763.

(19) Hung, H. M.; Hoffmann, M. R. *Environ. Sci. Technol.* **1998**, *32*, 3011-3016.

(20) Suslick, K. S.; Didenko, Y.; Fang, M. M.; Hyeon, T.; Kolbeck, K. J.; McNamara, W. B.; Mdleleni, M. M.; Wong, M. *Phil. Trans. Royal Soc. London, Series A* **1999**, *357*, 335-353.

(21) Gutierrez, M.; Heinglen, A. *J. Phys. Chem.* **1990**, *94*, 3625-3628.

(22) Holt, R. G.; Crum, L. A. *J. Acoust. Soc. Am.* **1992**, *91*, 1924-1932.

(23) Price, G. J.; Duck, F. A.; Digby, M.; Holland, W.; Berrman, T. *Ultrason. Sonochem.* **1997**, *4*, 165-171.

(24) Vichare, N.; Gogate, P.; Pandit, A. *Chem. Eng. & Technol.* **2000**, *23*, 683-690.

(25) Sunartio, D.; Ashokkumar, M.; Grieser, F. *J. Phys. Chem. B* **2005**, *109*, 20044-20050.

(26) Leighton, T. G. *The Acoustic Bubble*; Academic Press: London, 1994.

(27) Campbell, T. Y.; Vecitis, C. D.; Mader, B. T.; Hoffmann, M. R. *J. Phys. Chem. A* **2009**, *113*, 9834-9842.

(28) Moriwaki, H.; Takagi, Y.; Tanaka, M.; Tsuruho, K.; Okitsu, K.; Maeda, Y. *Environ. Sci. Technol*. **2005**, *39*, 3388-3392.

(29) Vecitis, C. D.; Park, H. P.; Cheng, J.; Mader, B. T.; Hoffmann, M. R. *J. Phys. Chem. C* **2008**, *112*, 16850-16857.

(30) Cheng, J.; Vecitis, C. D.; Park, H.; Mader, B. T.; Hoffmann, M. R. *Environ. Sci. Technol*. **2008**, *42*, 8057-8063.

(31) Vecitis, C. D.; Wang, Y.; Cheng, J.; Park, H.; Bader, B. T.; Hoffmann, M. R. *Environ. Sci. Technol.* Accepted November **2009**.

(32) Cheng, J.; Vecitis, C. D.; Park, H.; Bader, B. T.; Hoffmann, M. R. *Environ. Sci. Technol.* Accepted November **2009**.

(33) Hua, I.; Hoffmann, M. R. *Environ. Sci. Technol.* **1997**, *31*, 2237-2243.

(34) Kawabata, K.; Umemura, S. *J. Phys. Chem.* **1996**, *100*, 18784-18789.

(35) Kawabata, K.; Umemura, S. *Ultrason. Sonochem.* **1996**, *3*, 1-5.

(36) Yasuda, K.; Torii, T.; Yasui, K.; Iida, Y.; Tuziuti, T.; Nakamura, M.; Asakura, Y. *Ultrason. Sonochem.* **2007**, *14*, 699-704.

(37) Swamy, K. M.; Narayana, K. L. *Ultrason. Sonochem.* **2001**, *8*, 341-346.

(38) Brotchie, A.; Ashokkumar, M.; Grieser, F. *J. Phys. Chem. C* **2007**, *111*, 3066-3070.

(39) Couppis, E. C.; Klinzing, G. E. *AIChE*. **1974**, *20*, 485-491.

(40) Sunartio, D.; Ashokkumar, M.; Grieser, F. *J. Am. Chem. Soc.* **2007**, *129*, 6031-6036.

(41) Colussi, A. J.; Weavers, L. K.; Hoffmann, M. R. *J. Phys. Chem. A* **1998**, 102, 6927-6934.

(42) Colussi, A. J.; Hoffmann, M. R. *J. Phys. Chem. A* **1999**, *103*, 11336-11339.

(43) Krusic, P. J.; Roe, D. C. *Anal. Chem.* **2004**, *76*, 3800-3803.

Chapter 3

A Langmuir Type Mechanism for the Sonochemical Degradation of Perfluorosurfactants

Introduction

Sonochemistry involves the use of sounds waves as an energy source to increase chemical reactivity in solution. Modern ultrasonic devices rely on piezoelectric transducers to generate sounds waves that move longitudinally through a liquid medium enhancing molecular motion, leading to a wide variety of physical and chemical processes such as hydrodynamic shearing,[1, 2] the degradation [3-5] or synthesis[6, 7] of chemical species, or nanoparticle dispersion[8]. These processes are dependent on the phenomenon termed acoustic cavitation, the formation, growth, and collapse of vapour bubbles which generates average vapor temperatures near 5000 K[10, 11] and pressures on the order of several hundred atmospheres.[12] The degradation of dissolved organic compounds occur either through direct pyrolysis or through oxidation reactions with transiently produced high temperature species such as O-atoms, hydroxyl radicals and H-atoms generated from the pyrolysis of water.[13]

The efficient decomposition of organic compounds using ultrasound irradiation makes it a viable technology in the remediation of environmentally persistent and recalcitrant compounds such as perfluorinated chemicals (PFCs). Due to their high bond strength (450-530 kJ mol-1) and low polarizability, PFCs are resistant to current advanced oxidative technologies. Reduction using elemental iron under near supercriticial water conditions is effective in decomposing PFC's to their primary constituents; however, the scale-up of a high pressure and a high temperature system has proven difficult.[14, 15] Photodegradation of PFOS by UV irradiation in water is possible but with slow rates of degradation.[16] Recently, acoustic cavitation as induced by high frequency ultrasound was shown to successfully degrade perfluorinated surfactants,

perfluorooctane sulfonate (PFOS) and perfluorooctanoate (PFOA) to their inorganic constituents.[14, 17] Therefore, while most organic compounds can be degraded through more economically viable alternative remediation techniques, sonochemistry is a plausible option for persistent pollutants such as fluorochemicals.

A number of reports concerning the sonochemical degradation of various types of organic compounds under heterogenous and homogenous conditons have revealed a Langmuir type kinetic model. Nanzai et al reported reported a Langmuir type mechanism for the degradation of alkylbenzene sulfonates of varying chain length at concentrations between 15-40 mM.[4] Okitsu et al showed the sonochemical degradation of azo dyes, butyric acid, and benzoic acid following Langmuir-Hinshelwood kinetics.[18] Finally, Vecitis et al measured the concentration-dependent rates of perfluorooctanesulfonate (PFOS) and perfluorooctanoate (PFOA) below 100 mM and modeled the results with a Langmuir type mechanism.[19] Due to their surface active properties, all aforementioned organic compounds accumulate at the interfacial region of the cavitation bubble where they undergo adsorption prior to interfacial sonochemistry.

The physical process of adsorption of perfluorinated surfactants, PFOS and PFOA, to the bubble-water interface dictates the rates of their sonochemical degradation[19] with the initial rate-determining step being the ionic headgroup cleavage at the interface followed by a relatively quick mineralization of the fluorcarbon tail.[14] However, a detailed study on how chain length effects the adsorption to the bubble-water interface has yet to be investigated. Studies by Campbell et al reveal that equilibrium bubble surface partitioning was shown to have no correlation to perfluorinated surfactants (C_n > 4) sonochemical kinetics and that adsorption was ultrasonically mediated under lightly

populated conditions.[20] However, initial results also suggested a possible correlation between equilibrium partitioning and sonochemical kinetics for the shorter chain and less surface active species, perfluorobutane sulfonate (PFBS) and perfluorobutanoate (PFBA).

Although reports on the reaction kinetic model of the longer chain PFOS and PFOA have been made, information about the concentration dependent reaction kinetics of shorter chain PFHA, PFHS, PFBA and PFBS are investigated for the first time. Application of a Langmuir type kinetic model on the basis of a heterogeneous solution system is applied in evaluating the sonochemical effects on surface activity and the absolute rates over four orders of magnitude of initial PFYX (Y = H or B, X = A or S) are determined. Furthermore, changes in the physico-chemical properties of bubbles caused by the accumulation of the surfactants will also be considered.

Experimental Methods

Perfluorobutyric acid (PFBA) and perfluorohexanoic acid (PFHA) were purchased from Sigma Aldrich. Potassium perfluorobutane-1-sulfonate (PFBS) and potassium perfluorohexane-1-sulfonate (PFHS) were provided by 3M. Ammonium acetate (>99%) and methanol (HR-GC > 99.99%) were obtained from EMD Chemicals Inc. Aqueous solutions were prepared with purified water using a Milli-Q system (18.2 MW cm resistivity). Acid solutions were brought to a pH of 7.0 by addition of ammonium hydroxide.

An ultrasonic frequency of 618 kHz was generated using an Allied Signal-ELAC Nautik ultrasonic transducer with the reaction solution held in a 600 mL jacketed glass reactor. The applied power density was 250 W L^{-1}. The temperature was controlled with a Haake A80 refrigerated bath maintained at 10 °C. All reactions were sparged with

argon for at least 30 minutes prior to and during the reactions. PFHS and PFHA were sonicated simultaneously over an initial concentration range of 467 nM to 110 mM for PFHA and 122 nM to 135 mM for PFHS. PFBS and PFBA were sonicated simultaneously over an initial concentration range of 277 nM to 158 mM for PFBA and 217 nM to 122 mM for PFBS. Higher concentrations of the four compounds were not tested, as sonication caused the compounds to precipitate. Concentration versus time profiles were fitted either to a single exponential decay for first-order kinetics, or linearly for zero-order kinetics.

Analysis of PFBA and PFBS was completed by high-performance liquid chromatography mass spectrometry (HPLC-MS). The samples were placed into 750 mL polypropylene autosampler vials and sealed with a poly(tetrafluoroethylene) (PTFE) septum crimp cap. For reactions with initial concentrations greater than 250 ppb, serial dilutions to achieve a concentration of 100 ppb were completed prior to analysis. Aliquots (20 μL) were injected into an Agilent 1100 LC for separation on a Betasil C18 column (Thermo-Electron) of dimensions 2.1 mm i.d., 100 mm length, and 5 μm particle size. A 2 mM aqueous ammonium acetate/methanol mobile phase at a flow rate of 0.3 mL min-1 was used with an initial 5:95 aqueous/methanol composition. The eluent composition was increased to 90:10 over 12 min to separate the PFCs. HPLC effluents were analyzed with an Agilent ion trap mass spectrometer in the negative ion mode for the perfluorohexanesulfonate molecular ion (m/z = 399), the perfluorobutanesulfonate molecular ion (m/z = 299), the decarboxylated perfluorohexanoate ion (m/z = 269) and the decarboxylated perfluorobutanoate ion (m/z = 169). The nebulizer gas pressure was 40 PSI and the drying gas flow rate and temperature were 9 L min-1 and 325 °C,

respectively. The capillary voltage was set at +3500 V and the skimmer voltage was -15V. Quantification was completed by first producing a calibration curve using 8 concentrations between 1 and 200 ppb fitted to a quadratic with X^{-1} weighting.

Surface tension measurements were made with a De Nouy tensiometer utilizing the ring method. The tensiometer was calibrated with a weight of known mass. Each sample was measured three times. The PFBS surface tension measurements were on concentrations up to 10 and 100 mM, respectively, where the compounds became insoluble. The curve was fitted to the surface pressure equation of state using Matlab to determine the equilibrium air-water partitioning coefficient and the maximum surface concentration.

Results

PFBX Concentration-Dependent Sonochemical Kinetics.

Sonolysis of aqueous solution of perfluorinated surfactants using different initial concentrations were carried out at 618 kHz, 250 W L^{-1}, 10 °C under an argon atmosphere. The initial concentration ranges for PFBA were 277 nM – 158 μM and for PFBS were 217 nM – 123 μM. The degradation of PFBX (X = c(A)rboxylate or (S)ulfonate) by sonication is reflected by a decrease in concentration of each of the PFCs over time (depicted in Figures 1a-b). At PFBA concentrations over the range of 277 nM to 29.6 μM, the observed kinetics are pseudo-first order and are fitted to a single exponential decay. Similarly, at concentrations over the range of 217 nM to 19.2 μM, PFBS kinetics are pseudo-first order and are also fitted to a single exponential decay. Previously reported results on PFBA and PFBS sonochemical decomposition completed at $[PFBA]_i \leq$ 0.47 μM and $[PFBS]_i \leq 0.30$ μM displayed similar kinetic orders (Campbell, J. Phys

Chem C). At PFBA concentrations of 53.3 μM to 158 μM, the reaction kinetics are zero-order over the entire time-course. Similar, zero-order reaction kinetics are observed for PFBS concentrations of 40.5 μM to 123 μM.

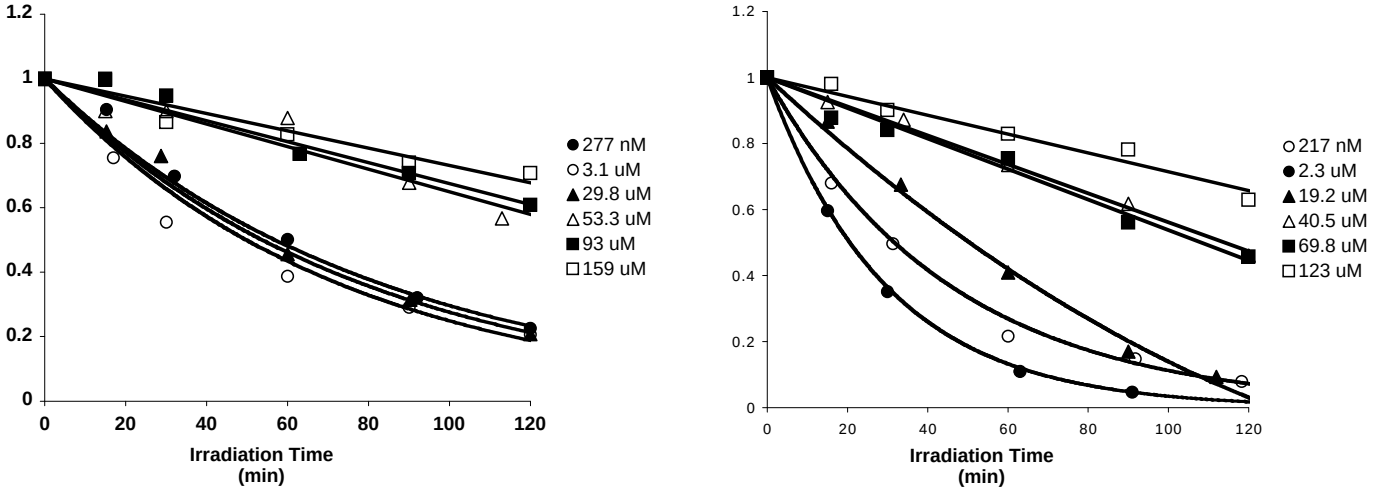

Figure 1a-b. Time dependent plots of PFBX sonolytic degradation over a range of initial concentrations under ultrasonic conditions: 618 kHz, 250 W L^{-1}, 10 °C, and argon. (a) $[PFBA]_t/[PFBA]_i$ vs time in minutes. (b) $[PFBS]_t/[PFBS]_i$ vs time in minutes.

The transition of PFBX from pseudo-first-order kinetics at low concentrations to zero-order kinetics at high concentrations is consistent with saturation kinetics in which high $[PFBX]_I$ saturate the adsorption sites at the transiently cavitating bubble-water interface where sonochemical decomposition of PFBX occurs pyrolytically. The observed kinetic parameters are given in Table 1.

TABLE 1: Concentration Dependent Sonochemical Kinetics of PFBX

[PFBA] (nM)	first-order (min^{-1})	zero-order (nM min^{-1})	-d[PFBA]/dt (nM min^{-1})	[PFBS] (nM)	first-order (min^{-1})	zero-order (nM min^{-1})	-d[PFBS]/dt (nM min^{-1})
277	0.014		3.85	217	0.022		4.71
3099	0.017		52.3	2297	0.029		65.9
15137	0.006		96.9	9521	0.009		82.8
29621	0.004		118	19160	0.005		93.9
53261		79.9	79.9	40509		166	166
92973		205	205	69781		286	286
125210		238	238	91661		275	275
158849		238	238	109107		185	185
158382		317	317	122708		417	417

For low initial concentrations, $[PFBA]_i \leq 29.6$ μM and $[PFBS]_i \leq 19.1$ μM the time-dependent plot was fitted to an exponential curve to determine the first-order rate constant, k_{app}^{-PFBX} (min^{-1}), and eq 1 was used to determine the absolute rate.

$$\frac{d[PFBX]}{dt} = -k_{app}^{-PFBX}[PFBX] \qquad (1)$$

For high initial concentrations, $[PFBA]_i > 50$ μM and $[PFBS]_I > 30$ μM, the time-dependent plot was fitted to a linear curve with the slope $k_{app}^{-PFBX'}$, taken to be the absolute degradation rate, eq 2.

$$\frac{d[PFBX]}{dt} = -k_{app}^{-PFBX'} \qquad (2)$$

For concentrations less than 53.4 μM, the degradation rates were in the order $k_{app}^{PFBS} > k_{app}^{PFBA}$. These results are the same as previous reports on the sonolysis of PFBX.[20]

Equilibrium Partitioning to the Air-Water Interface.

In previous reports, a kinetic model based on a Langmuir type mechanism was described for the sonolysis of PFOS and PFOA.[19] This model was used to explain the localization of the reaction zone to be at the interfacial region of the transiently cavitation bubble, where pyrolysis occurred due to high temperatures. The interfacial adsorption of

PFBA and PFBS are also described by the Langmuir type mechanism. In the Langmuir model, the surface excess, Γ_{ex}, is a function of the equilibrium interface partitioning constant, K_{eq} in liters per mole, and the maximum surface concentration Γ_{max} in moles per square meter. The equibrium adsorption of PFBX to the bubble-water interface is shown in eq 3.

$$\Gamma_{ex,eq}^{PFBX} = \Gamma_{Max,eq}^{PFBX} \frac{K_{eq}^{PFBX}[PFBX]}{1 + K_{eq}^{PFBX}[PFBX]} \qquad (3)$$

The Γ_{ex} and K_{eq} values are determined from the dependence of surface tension on surfactant concentration (Figure 2) by least-squares fitting of the surface pressure to the Szyszkowski equation, eq 4.

$$\Pi = \gamma_0 - \gamma_{[PFBX]} = nRT\Gamma_{Max,eq}^{PFBX} \ln(1 + K_{eq}^{PFBX}[PFBX]) \qquad (4)$$

where Π is the surface pressure in newtons per meter, $\gamma_0 = 0.072$ N m^{-1} is the surface tension of pure water, and $\gamma_{[PFBX]}$ is the surface tension at varying PFBX concentration. Maximum air-water interface concentrations are previously reported as $\Gamma_{max}^{PFBA} = 1.95 \times 10^{-6}$ mol m^{-2} and $\Gamma^{PFBS} = 4.4 \times 10^{-6}$ mol m^{-2} and equilibrium partitioning coefficients as $K^{PFBA} = 31.7$ L mol^{-1} and $K^{PFBS} = 40.4$ L mol^{-1}.

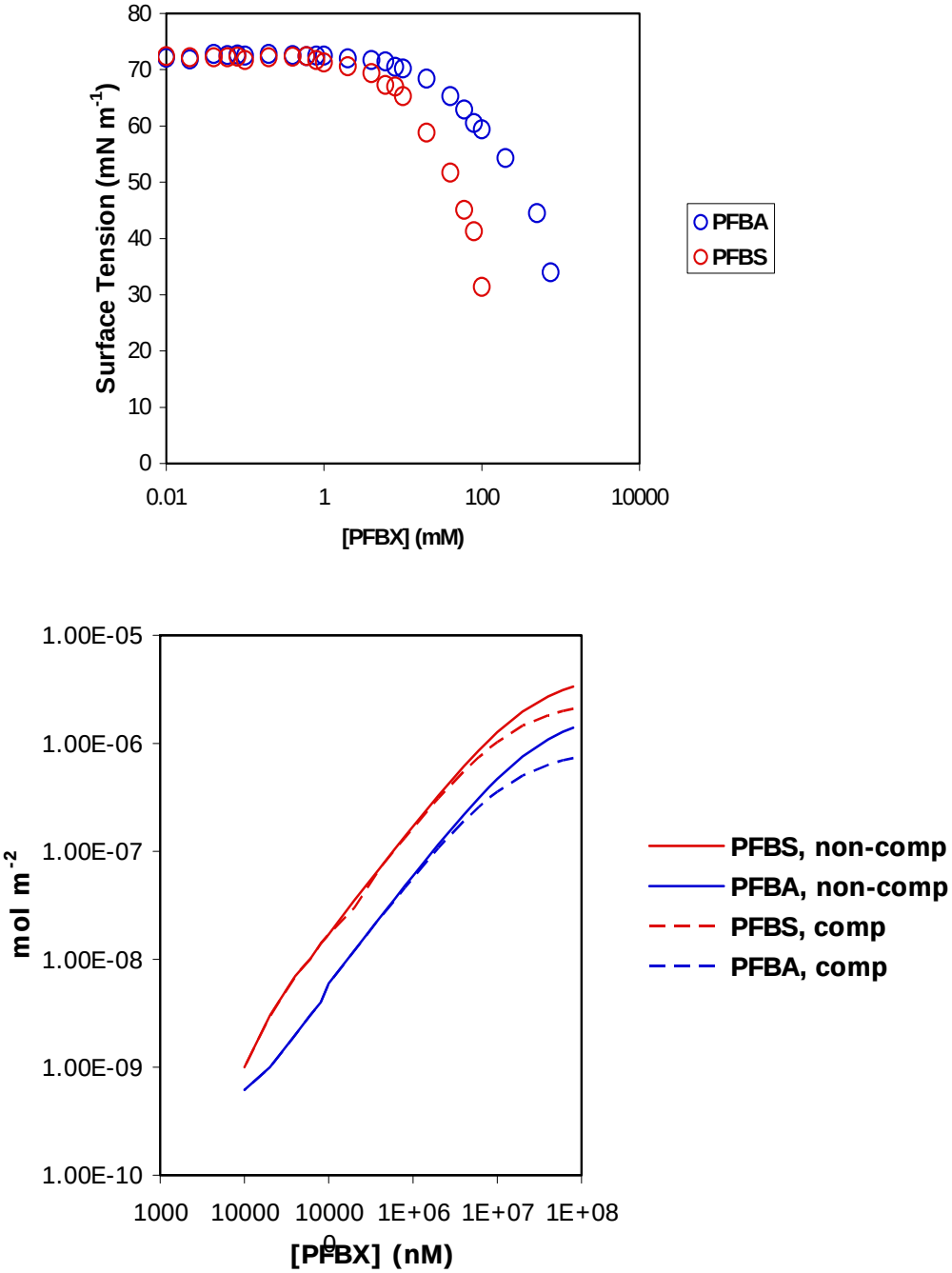

Figure 2. (a) Surface tension of PFBX as a function of concentration. (b) Plot of surface excess vs aqueous PFBS or PFBA concentration: (red solid line) PFBS noncompetitive, (blue solid line) PFBA noncompetitive, (red dashed line) PFBS competitive, (blue dashed line) PFBA competitive.

According to the surface tension data, PFBS shows to be the stronger surfactant. Furthermore surface excess values versus PFBX concenrations were plotted in Figure 2b where solid lines represented individual PFBX curves and dashed lines are for individual components of the [PFBS] + [PFBA] curve modeled according to a competitive adsorption isotherm eq 5.

$$\Gamma_{ex,eq}^{PFBS} = \Gamma_{Max,eq}^{PFBS} \frac{K_{eq}^{PFBS}[PFBS]}{1 + K_{eq}^{PFBS}[PFBS] + K_{eq}^{PFBA}[PFBA]} \qquad (5)$$

Contrary to results by Vecitis et al in which PFOS outcompetes PFOA for air-water interface sites thus decreasing its surface excess by 7.2 under saturation condtions,[19] there is little competition between the surface excess of PFBS and PFBA due to the high water solubility of PFBA.

Discussion

d[PFBX]/dt vs [PFBX]$_I$ Sonochemical Kinetic Modeling.

There are three different regions in which sonochemistry can occur: (1) the inside of the cavitating bubble with high pressures and temperatures, (2) the interfacial region of the bubble, (3) the bulk solution. Although radical reactions occur in all the regions, perfluorinated surfactants are inert to OH radicals. Assuming that the majority of the surfactants exist in their anionic form, accumulation would occur at the bubble-water interface. The rate is dependent on the number of effective reaction sites to which the surfactants can bind. Binding in turn is dependent on the equilibrium constant, $K=k_1/k_{-1}$, which is defined as the concentration moving away or towards the reaction site prior to bubble collapse. At the moment of bubble collapse, molecules adsorbed at the reaction site are pyrolyzed with the pseudo-first order rate constant k.

The transition from first-order to zero-order kinetics upon increasing initial concentration is consistent with Langmuir kinetic mechanism In this mechanism, the rate of PFBX degradation is proportional to θ_{Sono}^{PFBX}, the fraction of total molecules adsorbed to the transiently cavitating bubble-water interface (eqs 6 and 7).

$$\theta_{Sono}^{PFBX} = \frac{K_{Sono}^{PFBX}[PFBX]}{1+K_{Sono}^{PFBX}[PFBX]} \tag{6}$$

$$\frac{d[PFBX]}{dt} = V_{\max}^{-PFBX}\ \theta_{Sono}^{PFBX} = V_{\max}^{-PFBX}\ \frac{K_{Sono}^{PFBX}[PFBX]}{1+K_{Sono}^{PFBX}[PFBX]} \tag{7}$$

$$\frac{d[PFBX]}{dt} = V_{\max}^{-PFBX}\ \frac{K_{Sono}^{PFBX}[PFBX]}{1+K_{Sono}^{PFBX}[PFBX]} \tag{8}$$

where $V_{\max}^{-PFYX}$ (M $s^{-1)}$ is the maximum rate of reaction when all the available adsorption sites are occupied and the interfacial adsorption equilibrium constant K_{Sono}^{PFBX} = k_1/k_{-1} represents PFBX concentration at the interfacial region or in the bulk solution. This is based on a pseudo-steady state assumption for the adsorption and desorption of PFBX under the conditions in which the approach to equilibrium and the determination of bubble lifetime is uncertain due to high frequency bubble oscillations.

The transition in kinetic regimes is consistent with a Langmuir model. At low PFBX concentrations, the surface is undersaturated, reflecting first-order kinetics (eqs 8 – 11).

$$K_{Sono}^{PFBX}[PFBX] << 1 \tag{8}$$

$$\theta_{\text{Sono}}^{PFBX} = K_{Sono}^{PFBX}[PFBX] \tag{9}$$

$$\frac{d[PFBX]}{dt} = k_{app}^{-PFBX}[PFBX] = -V_{Max}^{PFBX} K_{Sono}^{PFBX}[PFBX] \tag{10}$$

$$k_{app}^{-PFBX} = -V_{Max}^{PFBX} K_{Sono}^{PFBX} \tag{11}$$

Although no intermediate concentrations were observed, theoretically adsorption starts to slow down as the bubble surface becomes increasingly populated (eq 12):

$$\frac{d[PFBX]}{dt} = -V_{Max}^{PFBX} \frac{K_{Sono}^{PFBX}[PFBX]}{1 + K_{Sono}^{PFBX}[PFBX]} \qquad (12)$$

At high concentrations, all the surface sites are occupied and the maximum absolute rates is modeled by (eq 13 and 14).

$$K_{Sono}^{PFBX}[PFBX] >> 1 \qquad (13)$$

$$\frac{d[PFBX]}{dt} = -V_{Max}^{PFBX} \qquad (14)$$

These results correlate with a transition in kinetic regimes based on low and high concentration as consistent with Langmuir type kinetics. At low and intermediate concentrations, the kinetics is proportional to the concentration of PFBX adsorbed to the bubble water interface, while high concentrations suggest the rate limiting step to be PFBX pyrolysis due to complete occupation of all surface sites.[19]

Figure 3 a and 3b show the absolute degradation rate vs PFBX concentration in linear-linear and log-log format, respectively (values obtained from Table 1). Over the initial concentration ranges from 200 nM to 3000 nM, k_{app}^{-PFBX} (eq 1) are constant with $k_{app}^{-PFBS} = 0.026$ min^{-1} and $k_{app}^{-PFBA} = 0.016$ min^{-1} and $k_{app}^{-PFBS} = 1.65\ k_{app}^{-PFBA}$. At these values, the surface sites are undersaturated and the increase in the absolute rates correlate with an increase in θ_{Sono}^{PFBX}. Due to the greater maximum interfacial concentrations of PFBS,

$\Gamma_{Max}^{PFBS} = 2.3\Gamma_{Max}^{PFBA}$, and larger partitioning coefficient, $K_{eq}^{PFBS} = 1.3K_{eq}^{PFBA}$, PFBS is expected to have greater equilibrium activity at the bubble-water interface.

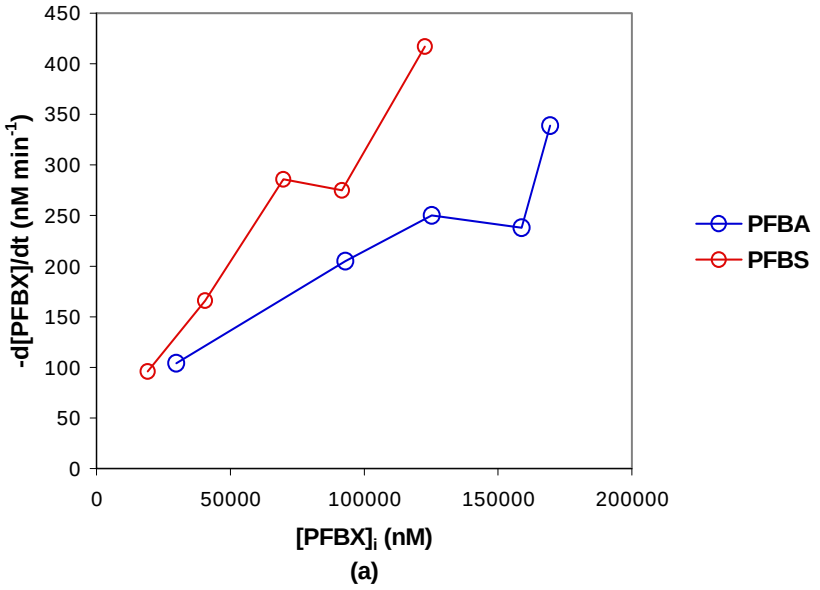

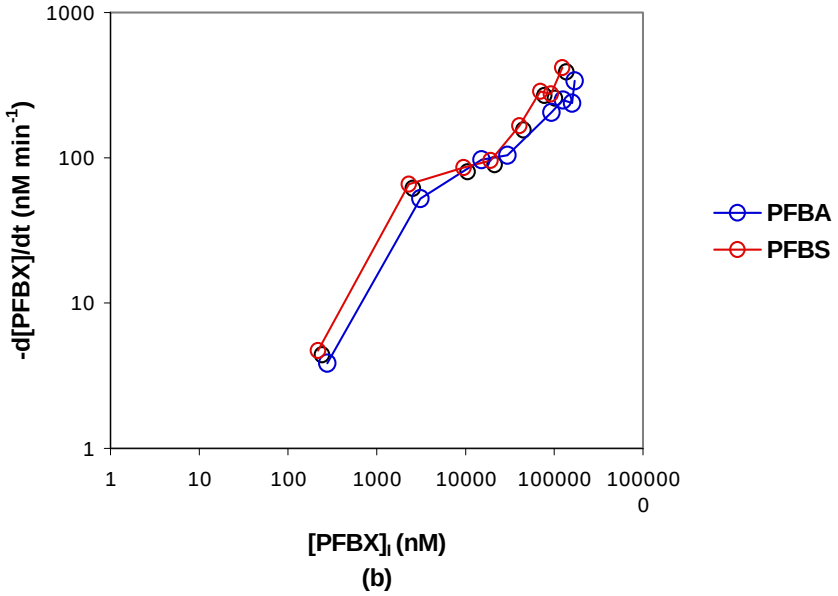

Figure 3. Absolute PFBX sonolysis rate plotted as a function of initial PFBX concentration and fitted by the competitive LH model: (a) Linear-linear plot (b) Log-log plot.

To find a linear relationship between concentration dependence and degradation rate, both sides of eq 12 were inverted:

$$\frac{1}{d[PFYX]/dt} = \frac{1}{V_{\max}^{-PFYX} K_{Sono}^{PFYX}} \frac{1}{[PFYX]} + \frac{1}{V_{\max}^{-PFYX}} \qquad (15)$$

and a reciprocal plot of $\frac{1}{d[PFYX]/dt}$ versus $\frac{1}{[PFYX]}$ based on the LH approach was shown in Figure 4a and 4b. [PFBX] > 40 μM (Figure 4a), showed a linear relationship, while data for [PFBX] < 30 μM (Figure 4b) was not able to be fitted in a straight line.

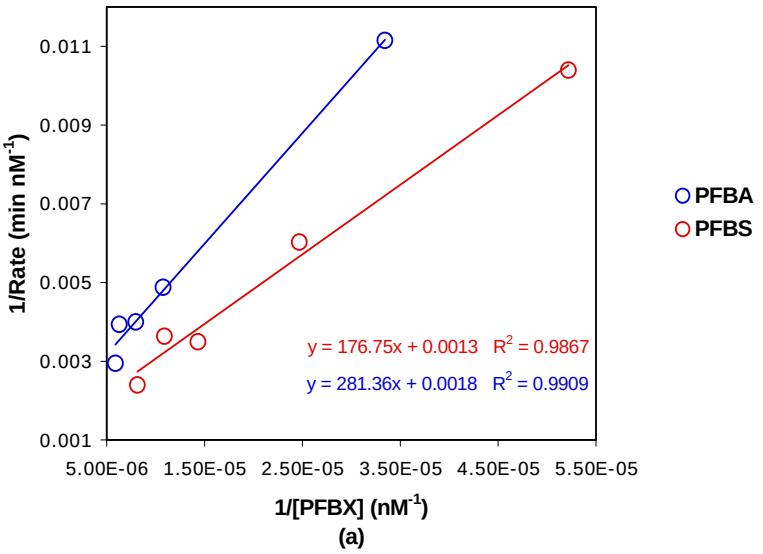

Figure 4. (a) Reciprocal plot of PFBA (29.9-159 μM), PFBS (19.1-109 μM). (b) Reciprocal log-log plot of PFBA (277 nM -170 μM) and PFBS (217 nM - 123 μM).

As previously mentioned, according to Figure 3, at initial concentration ranges over 277 nM - 159 μM for [PFBA] and 217 nM – 109 μM for [PFBS], the absolute rates are observed to saturate at $V_{Max,App}^{-PFBA}$ = 252 nM min^{-1} and $V_{Max,App}^{-PFBS}$ = 281 nM min^{-1}, showing convergence of maximum rates of degradation when the bubble surface sites are saturated. These correspond to K_{sono} values of 63, 942 M^{-1} for PFBA and 92, 527 M^{-1} for PFBS with

$K_{PFBS} \approx 1.4\ K_{PFBA}$. However, reciprocal plots of the initial concentration vs the the rate over the initial concentrations ranges of 29.9 – 170 μM = PFBA and 19.2 – 123 μM = PFBS shows that $V_{Max,App}^{-PFBA}$ = 556 nM min^{-1} and $V_{Max,App}^{-PFBS}$ = 769 nM min^{-1} (Figure 4 and Table 2).

Table 2: Sonochemical vs Equilibrium Surface Activity. Italicized values of V_{Sono} are From Reciprocal Plots

	frequency (kHz)	applied power density (W L^{-1})	$\Gamma_{eq,\ max}$ (mol m^{-2})	K_{eq} (M^{-1})	$V_{sono,\ max}$(nM min^{-1})	K_{sono} (M^{-1})	K_{sono}/K_{eq}	ref.
PFBA	618	250	1.95e-6	31.7	252 *(556)*	6397	369	this work
PFBS	618	250	4.4e-6	40.4	282 *(769)*	7355	182	this work
PFOA	354	250	4.5e-6	360	1660	28500	79	vecitis
PFOS	354	250	5.1e-6	1970	230	121000	61	vecitis

The relative order of the K_{Sono} values is $K_{PFBS} \approx 1.1\ K_{PFBA}$. According to eq 6, K_{Sono} is proportional to θ_{Sono}^{PFYX}, the fraction of total molecules adsorbed to the transiently cavitating bubble-water interface. The longer tailed species partitions more effectively. However, the relative values of the sonolytic enhancement K_{sono}/K_{eq} are PFBA ≈ 2 PFBS suggesting a greater ultrasonic effect on the dynamic adsorption the the bubble interface by the shorter chain PFBA. Although small, the difference in the magnitude of sonolytic enhancement can be delineated from the ability of the surfactants to partition into the bubble-water interface, which is dependent on the n-alkyl chain length. The higher V_{max} from the reciprocal plots reflects variations from the LH kinetic model at [PFBA] > 159 μM and [PFBS] > 91.7 μM. At high concentrations, surfactant accumulation at the

bubble-water interface induces changes in the physico-chemical properties of the cavitating bubble.[4, 21, 22] Changes in the reaction pathway, in the physico-chemical properties of the bubble, and enhanced electrostatic repulsion between molecules and bubbles are all factors that may contribute to substantially enhanced rates.

According to Burns et al, in aqueous solution, there exists an equilibrium between two electronically and structurally unique species (i.e. PFBA and PFBA-H) which exhibit different partitioning capabilities dictated by their physicochemical properties.[23] The pH of the solution decreases over the irradiation time, such that the degradation of the chemicals is controlled by the relative proportions of the acidic (neutral species) and anionic species as well as the magnitude of their partition coefficents. When the anionic form of PFBA or PFBS is protonated, the neutral species will readily partition to the gas phase, lowering the collapse temperature [24] which can decrease the rate of the reaction as shown for PFBX in Figure 3a. However, fluorination which inductively withdraws electron density away from the carboxlate anion, stabilizing the conjugate base, has less effect with increasing chain length such that the shorter chain perfluorinated species, PFBA, has a lower pKa than PFBS. Furthermore, the dimensions of PFBA (0.26 nm) is more similar to an ionic hydration sphere (0.3 –0.4 nm) which reduces hydrophobic tail interactions such that it cannot compensate for the coulumbic repulsion between headgroups. Together, the rate of PFBA degradation is dependent on the number of surface sites available for it to bind. When all surface sites are covered, then the rates have reached maximum and can no longer increase with increasing concentration of PFBA (Figure 3). At 92 uM, PFBS reaches a Vmax value similar to PFBA, followed by a short decrease, then an increase in the absolute rates of degradation. The increase can

be attributed to the increasing pH of the solution which can shift the equilibrium towards a slightly more protonated concentration of PFBS which can partiition to the gas phase. However, upon higher concentration, aggregation of the anionic form of PFBS can occur[23] which suppresses the pH and in turn increases the amount of anionic surfactant in solution. Adsorption would increase the number of bubbles in solution therefore increasing the number of surface adsorption sites.

Conclusions

The concentration-dependent sonochemical kinetics have been studied over the initial concentration ranges of 200 nM to 170 μM and are fitted to a Langmuir model with rate maximums at 252 and 282 nM min^{-1} for PFBA and PFBS, respectively. The sonochemical mediated surface activities are K_{Sono}^{PFBA} = 6400 M^{-1} and K_{Sono}^{PFBS} = 7400 M^{-1}, implicating that the sonochemical surface activities, K_{Sono}^{PFBX}, are 80 to 100 times greater than the equilibrium surface activities, K_{eq}^{PFBX}. This study shows enhancements in absolute rates of degradation revealing how variations in concentration can be an optimization method in the application of ultrasound irradiation technology for the treatment of recalcitrant compounds.

Appendix

A Chemical Approach Toward Understanding the Role of Fucose in Neuronal Communication

Abstract

Fucose α(1-2) galactose carbohydrates have been implicated in modulating the recognition and communication between nerve cells that underlies long-term memory storage. Currently, our lab has established that the Fucα(1-2)Gal moiety stimulates neuronal outgrowth and changes in neuronal morphology.[2,3] Furthermore, increase in neurite outgrowth activity has been implicated through the use of polyvalent glycopolymers.[2] My project seeks to understand this mechanism by developing novel multivalent polyacrylamide probes that will help in the capture and identification of fucosyl lectins in developing neurons. Initially, we will optimize the synthesis and yields of the Fucα(1-2)Gal disaccharide followed by the polymerization of the disaccharide with a photoactivable crosslinker and biotin to yield a multifunctional glycopolymer. The capture of Fucα(1-2)Gal binding proteins will provide insight into the molecular mechanisms of fucosyl saccharides and enable us to gain a better understanding of their roles in the nervous system.

Introduction

Carbohydrates are key modulators of molecular and cellular recognition and encode information critical for mediating events such as blood-antigen recognition, inflammation, bacterial and viral pathogenesis.[10, 11] The ability of small oligosaccharide units to mimic the unique biological activities of the natural polysaccharide has provided

chemical biologists with the opportunity to create synthetic analogues with predetermined properties. [1] These defined structural properties can help elucidate the exact molecular mechanisms in which cellular signaling events take place, beginning at the cell surface and leading to downstream regulatory pathways.

Carbohydrates play an important role in many processes in the brain ranging from neuronal growth and differentiation to cell adhesion and synaptic plasticity. [21-26] Fucα(1-2)Gal, a terminal carbohydrate modification to *N*- and *O*-linked glycoproteins has been implicated in cognitive processes such as learning and memory.[2, 27, 28] For example, the inhibition of protein fucosylation using 2-deoxy-galactose, an inhibitor of the Fucα(1-2)Gal linkage, caused reversible amnesia in rats.[3,4, 29] Moreover, an increase in fucose incorporation into glycoproteins occurred upon passive avoidance training in animals and long-term potentiation (LTP), a cellular model for learning and memory.[3,5, 32,33] Finally, administration of L-fucose in rats enhanced memory formation and LTP. [3,6,34]

While the importance of fucoseα(1-2)galactose saccharides in modulating neuronal connections important for long-term memory storage have been established, their precise structure or function has yet to be elucidated in the brain. Recent studies in our lab have identified the presence of these carbohydrates on glycoproteins synapsin Ia and Ib, proteins involved in neurotransmitter release.[3] 2-Deoxy-galactose showed inhibition of the cellular fucosylation of synapsin and dramatic reduction in the expression of synapsin in 7 DIV (days in vitro) cultured neurons. Furthermore, 2-dGal added to hippocampal neurons that were cultured 7 (DIV) caused dramatic retraction of neurites and collapse of synapses, whereas 6-dGal produced no change in neuronal morphology.[3] Together, these results have suggested that Fucα(1-2)Gal and its associated proteins may regulate

morphological changes that underlie learning and memory.

Lectins possess the ability to behave as recognition molecules both inside and on the cell surface. While the existence of glycoproteins bearing the Fucα(1-2)Gal epitope have been established in the brain, potential lectins, proteins which interact with carbohydrate motifs, have yet to be identified. The recent discovery of Fucα(1-2) Gal glycoproteins in mature neuronal cultures implies that Fucα(1-2)Gal lectins also exist in the brain.[3,13] In an effort to capture these lectins, our lab synthesized the chemical probe in Figure 1 containing the carbohydrate recognition element, biotin, and a trifluoromethylphenydiazirine moiety, which enabled the capture of lectins via photoactivated crosslinking. However, monovalent interactions were not strong enough to isolate lectins for identification purposes. Overall, our efforts to identify these lectins have been hampered by the lack of an efficient biological probe that can bind to them strongly enough for isolation and purification.

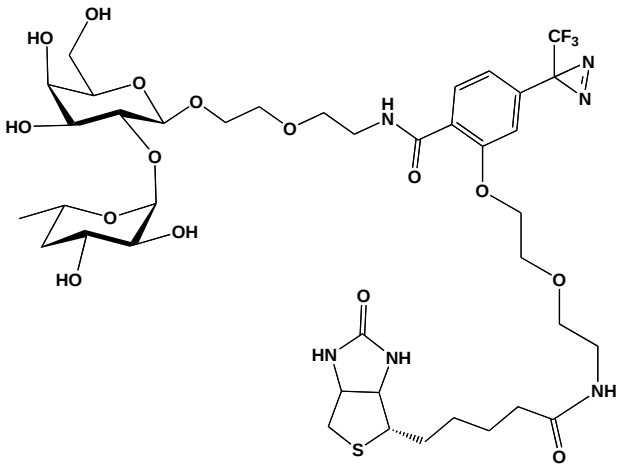

Figure 1. First Generation Chemical Probe for Identifying Fucα(1-2)Gal lectins.

The difficulty in capturing lectins lies in their weak carbohydrate-binding affinities.[7] Interestingly, polyacrylamide polymers bearing multiple Fucα(1-2)gal

epitopes (FucGal - PAA; MW ≈ 30kDa, 20% disaccharide density) were found to significantly enhance the interaction between carbohydrates and lectin receptors.[2] An interesting implication for this is that specific small molecules when supplied at high concentrations, is sufficient to stimulate a signal transduction cascade by coupling the functions of multiple cell surface receptors. Many receptors involved in cell surface signaling events function as dimers and oligomers which can increase ligand-receptor binding interactions thus stimulating downstream signaling events. [39] This clustering mechanism can either optimize alignment of an enzyme active site through the interactions of several receptors, cause subcellular localization of receptors to sites where intracellular signaling proteins are present, or enhance the intensity of a signal by increasing the number of receptors in one location. [38]

The ability of polyvalent interaction to amplify a biological effect has led my research to focus on the design and synthesis of a multivalent polyacrylamide-based capture probe to identify hard to isolate lectins and map out their roles as recognition molecules that mediate events involved in neuronal communication

Project Goals

Taking advantage of the enhanced binding affinity of lectins to polyvalent carbohydrate ligands, my project seeks to develop a new generation of multivalent probes to capture and identify lectins from the embryonic hippocampus of rats. The glycopolymer is highly functionalized to contain several Fucα(1-2)Gal recognition elements, phenylazide photo affinity labels to photochemically attach the polymer to recognition sites on the lectin receptor, and a biotin unit located at the end of the polymer to prevent interference with ligand/lectin receptor interactions and to optimize

purification approaches using avidin (streptavidin) based affinity chromatography.[8] The flexible design allows control over carbohydrate density and spacing between the polyacrylamide backbone and the carbohydrate ligand.

Capture of Fucα(1-2)Gal binding proteins will be followed by their identification by mass spectrometry. Our findings will establish that lectins in the brain are specific for the Fucα(1-2)Gal relative to other disaccharides and will provide a deeper understanding of the stereochemical and structural characteristics that give rise to carbohydrate specificity and binding interactions. We will be able to investigate whether Fucα(1-2)Gal saccharides function as an extracellular "recognition element" in their interactions with lectins. Together, our discoveries will help to correlate the chemical and structural changes occurring at the synapse to the downstream processes involved in nerve cell communication.

Synthetic Design

Our second generation of capture probes will consist of an end-labeled biotin with a spacer arm connected to a polyacrylamide backbone containing several Fucα(1-2)Gal and phenylazide units (Figure 2). The synthetic strategy of this multivalent polymer relies on a cyanoxyl-mediated free radical polymerization developed by Chaikof et al[8] in which the biotin derivatized arylamine acts as the initiator in the cyanoxyl-mediated pathway providing the desired end-labeled biotin.

The advantages of this pathway lie in its controlled design and synthesis. The majority of multifunctional glycopolymers available contain several anchoring groups within the polymer, which can inhibit or reduce the overall bioactivity of the polymer by interfering with carbohydrate-binding site interactions.[35,36] Furthermore, the

polyacrylamide scaffold minus the biotin and phenylazide linker has been proven to stimulate neurite outgrown in our assays [2]. Finally, through its polyacrylamide-based backbone, the glycopolymer is flexible and behaves in a random coil fashion [1], optimizing the ability of the carbohydrates to rearrange and interact with lectins.

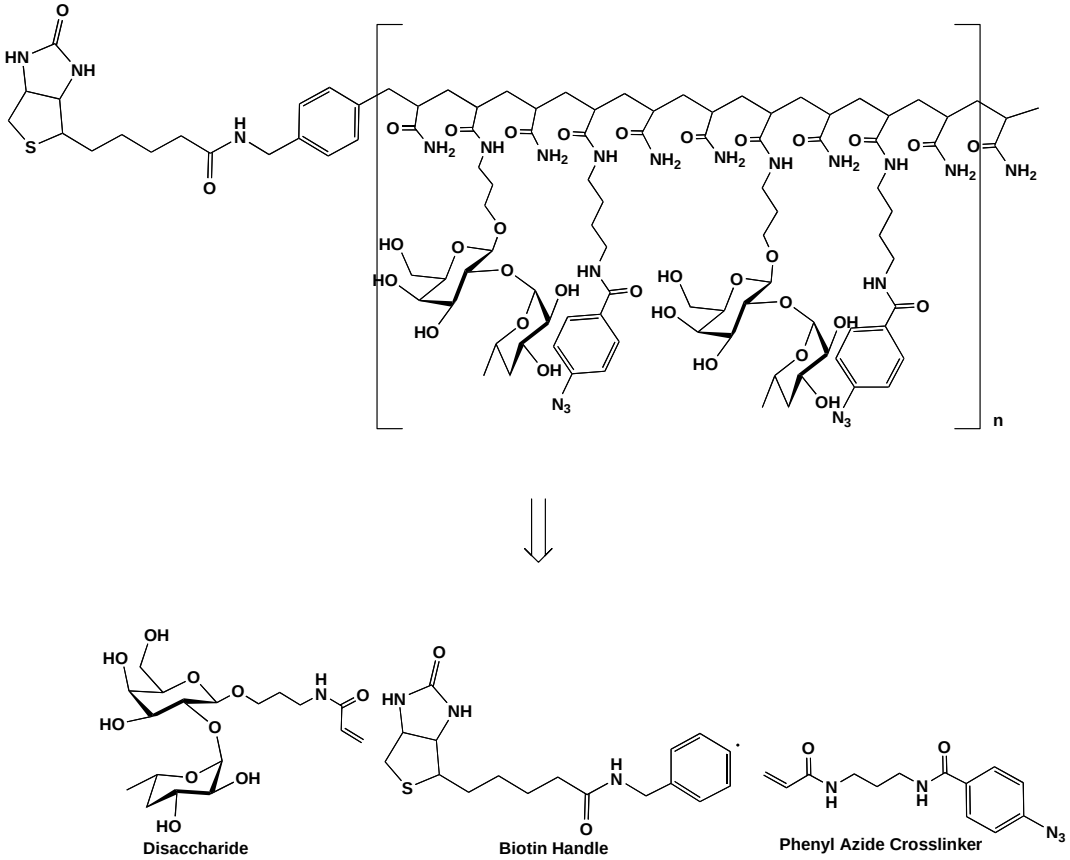

Figure 2. Design of a multivalent capture probe to identify Fucα(1-2)Gal binding proteins.

Results and Discussion

Prior to polymerization, our goal was to develop a new route to optimize the synthesis of our disaccharide. This entailed choosing ideal protecting groups that improved yields and shortened steps. Overall, we were able to successfully develop a

route to our disaccharide in ten steps. However, prior to the optimized route, we attempted a one-pot protection-glycosylation procedure developed by Wang et al[17] in which α1-2 disaccharides were generated through a highly regioselective protection of hexopyranosides to provide a free hydroxyl at the C-2 position (Figure 3).

In Wang's one-pot strategy, isopropylidenation was followed by a highly selective benzylation of hexopyranosides, generating a fully protected 2-hydroxy monosaccharide. This reaction occurs under a very mild, acid-catalyzed reductive etherification of the *O*-trimethylsilyl intermediate with benzaldehyde.[18] The resulting 2-hydroxy compound can then be coupled to an activated imidate via an α1-2 linkage. The regioselectivity at the hydroxyl of C-6 was attributed to steric interference from the anomeric linker group and an inductive effect from the anomeric oxygen which decreased the nucleophilicity at the C-2 hydroxyl position.[17]

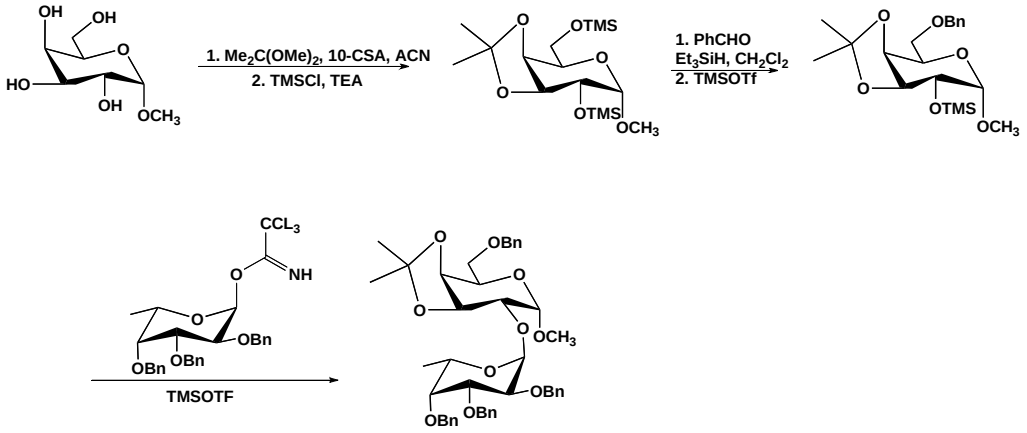

Figure 3. Wang's Regioselective One Pot Synthesis.

Synthesis of Monomers

We decided to apply Wang's one pot procedure to the protection of our galactopyranoside which had a propanolamine linker β to the anomeric position (Figure 4).

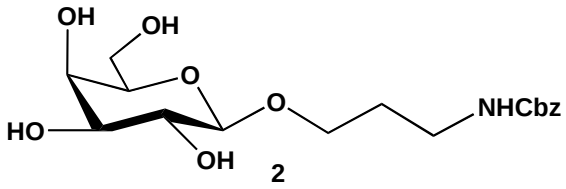

Figure 4. Carbobenzoxy 3-amino-1-propyl β-D-galactopyranoside

We chose peracetylated galactose as our starting material. Sugar peracetates are very convenient glycosyl donors and can form 1,2 trans-stereoselective products.[19] This occurs through an acid-catalyzed formation of a 1,2-acyloxonium ion intermediate which can then react with nucleophiles to produce the 1,2-trans product.[19] Therefore, peracetylated D-galactose was reacted in a $BF_3 \bullet OEt_2$ catalyzed coupling to carbobenzoxy protected 3-aminopropanol[12] , followed by deacetylation in methanol and sodium methoxide to yield the unprotected galactose monomer **2** (Figure 4).

The next step in the synthesis of our galactose monomer was isopropylidenation at the C-3 and C-4 hydroxyl, followed by silylation with tetramethylsilyl chloride at the C-2 and C-6 position (Figure 5). The silyl ether at the C-6 position served as an activator for acid catalyzed reductive etherification of benzaldeyde with triethylsilane.

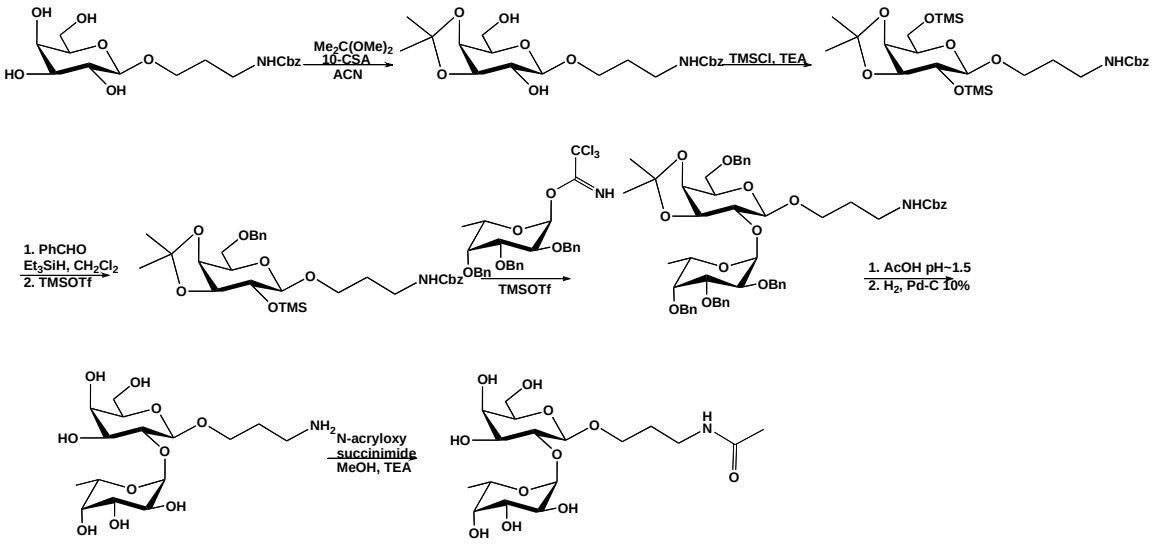

Figure 5. Proposed Route towards Fucα(1-2)Gal via One-Pot Protection and Glycosylation.

Although the Wang strategy seemed promising, attempts to synthesize our disaccharide through the one-pot method were unsuccessful. We had difficulty in generating the isopropylidene and in maintaining the silyl ether intermediate which proved labile upon addition of TMSOTf. While our linker group was in the β orientation in our galactose monomer, in Wang's procedure, most of the groups at the anomeric position were in the α orientation, except for S-ethylthiol. We considered using S-ethyl β-galactopyranoside and allyl α-galactopyranoside as possible starting materials that could later undergo either substitution or deprotection/activation at the anomeric position

by our linker group. However, the number of steps were increased such that the overall synthetic plan did not seem optimal to affording the disaccharide in good yield.

Our next step, was to improve our synthetic plan by choosing the route depicted in Figure 6. We initially had to examine the isopropylidene reaction in detail since it gave us the most problems in terms of starting material reactivity and product yield. Reacting our galactose monomer under 10-CSA in acetonitrile gave us both 3,4- and 4,6-*O*-isopropylidenes, with greater formation of the 4,6 *O*-isopropylidene. Due to the excess formation of the kinetically favored 4,6 *O*-isopropylidene, approaches using different acid catalysts over a 24 h period were implemented to optimize the synthesis of the thermodynamically stable 3,4 *O*-isopropylidene derivative and consumption of starting material. Allowing the reaction to go to 48 h resulted in full consumption of starting material but with excess formation of a methyl methoxyethyl ether at the C-6 hydroxyl. However, this was readily removed under refluxing conditions at 50°C in 10:1 MeOH/H_2O and catalytic amounts of acetic acid.

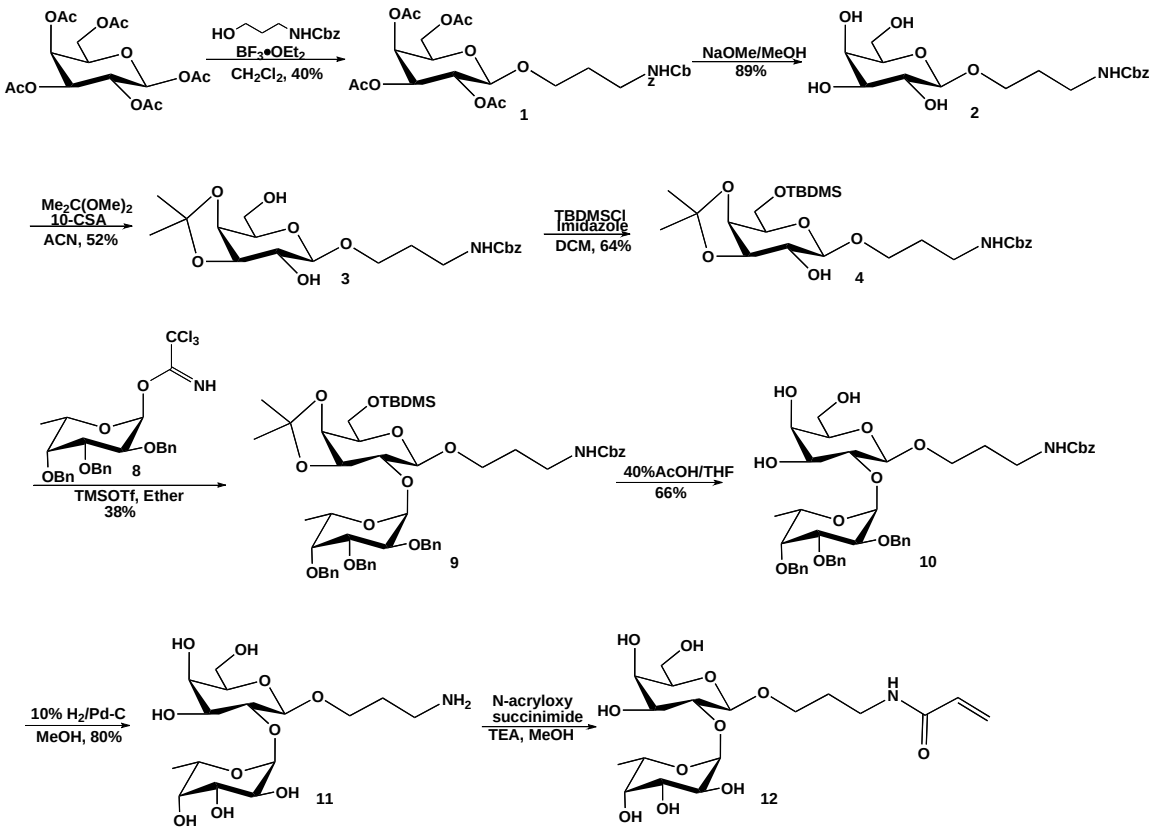

Figure 6. Synthesis of the disaccharide monomer 12.

We then chose to protect the hydroxyl group at the C-6 position with the *tert* – butyldimethylsilyl moiety since it was more stable than the TMS ether yet readily cleaved under mild acidic conditions and in parallel with the isopropylidene group.

The fucose monomer was synthesized according to Wegmann et al[16], beginning with the conversion of L-fucose to the methyl glycoside by refluxing in methanol under acidic conditions (Figure 7). This was followed by benzylation and hydrolysis of the methyl glycoside. The resulting fucose intermediate was treated with potassium carbonate, sodium hydride and trichloroacetonitrile in dichloromethane to form fucosyl trichloroacetimidate **8**. [18] Due to its instability the fucosyl imidate could not be isolated and therefore was immediately coupled to the protected galactose monomer.

Coupling the galactose acceptor **4** with trichloroacetimidate **8** in trimethylsilyl trifluoromethanesulfonate and diethyl ether produced fully protected disaccharide **9** with the desired Fucα(1-2) Gal linkage. Treatment of the disaccharide in acetic acid (pH~1.5) removed both the isopropylidene and TBDMS group in a single step **10**. Finally, hydrogenolysis on Pd-C in methanol removed the benzyl and *N*- carbobenzoxy groups **11**. The free amine was then ready for reaction with *N*-acryloxysuccinimide in TEA and MeOH to form **12**.

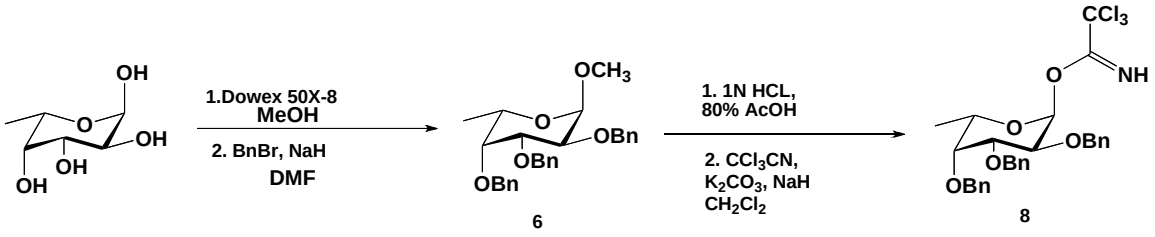

Figure 7. Synthesis of the fucosyl monomer **8.**

The phenylazide monomer was chosen because of the commercial availability of the starting material, *N*-succinimidyl 4-azidobenzoate, and its facile coupling with 1,3 diaminopropane under basic conditions. It is also compatible with other bioreagents under physiological conditions. The phenylazide activation at 360 nm is optimal since it avoids damaging the proteins and generates a highly reactive nitrene intermediate that is able to undergo C-H insertion efficiently.[9] The phenyl azide was prepared by reacting *N*-5-azido 2-nitrobenzyloxysuccinimide with diaminopropane to yield **13** (Figure 7). The product of this reaction will be coupled to *N*-acryloxysuccinimide in TEA and 1:1 THF/DMF to form **14**.

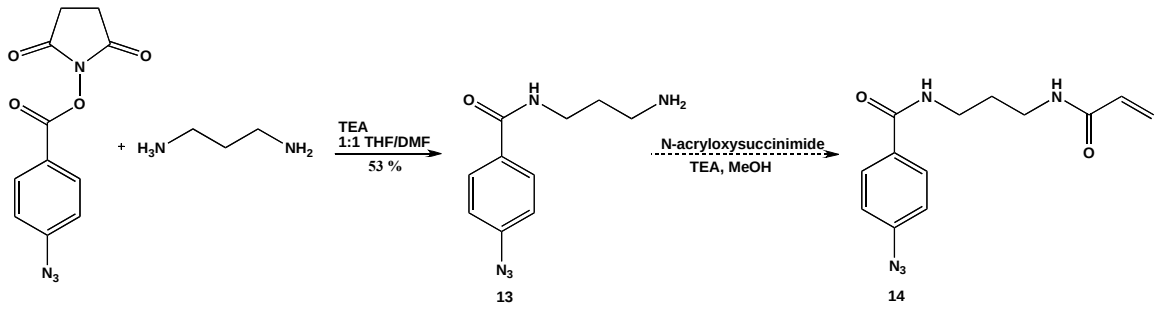

Figure 8. Preparation of phenylazide monomer.

Finally, a small sample of the galactose monomer **2** was deprotected via hydrogenolysis of the carbobenzoxy group followed by coupling to *N*-acryloxysuccinimide to yield **19** (Figure 9). This monomer was used as a model compound to test the efficacy of the Chaikof polymerization method prior to subjecting our disaccharide and phenylazide monomers to the polymerization reaction.

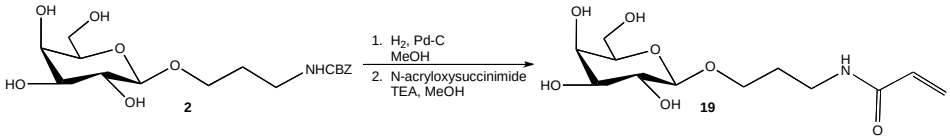

Figure 9. Synthesis of galactose monomer as a model compound for polymerization.

Polymerization

The biotinarylamine initiator was prepared by reacting *p*-nitrobenzylamine with *N*-hydroxysuccinimidyl biotin in TEA and DMF to afford *p*-nitrobenzyl biotinamide **15**, followed by hydrogenation under Pd/C in MeOH to yield 4-aminobenzyl biotinamide **16** (Figure 8). In a one pot reaction the arylamine was treated with sodium nitrite and tetrafluoroboronic acid in water and THF to give the arenediazonium cation, which upon addition of sodium cyanate provided the arylamine initiator and cyanoxyl free radical. This was followed by subsequent addition of acrylamide and the glycomonomer.

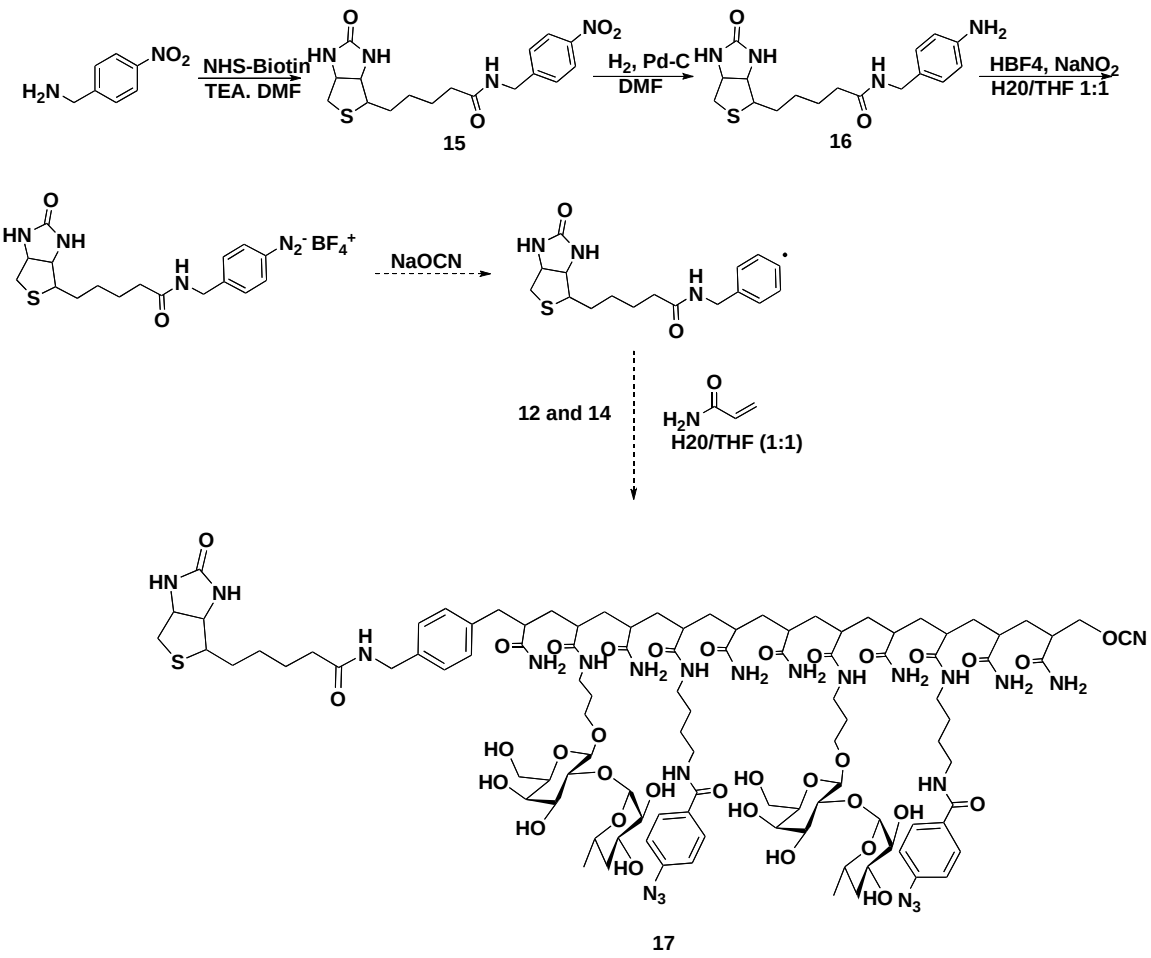

Figure 10. Biotin Chain-Terminated Multivalent Polyacrylamide Probe

While the biotin and acrylamide monomers underwent polymerization, the galactose monomer did not successfully incorporate into the polymer chain. To address this problem, the reaction was performed under deoxygenated conditions using THF that lacked stabilizer, which we believed contributed to radical quenching. However, stability of the intermediates also posed a challenge in the polymer synthesis. Currently, while optimizing the conditions in which the reactions take place, We are ensuring the purity and stability of the products by either performing our experiments in situ or using our intermediates immediately upon preparation.

NMR spectroscopy will help to characterize the glycopolymer through comparison of integration signals of the phenyl protons, anomeric protons of fucose, as well as the methine on the polymer backbone. Size-exclusion chromatography(SEC) coupled with refractive index and laser-light scattering (LLS) detectors will define the actual molar mass (M_n) and polydispersity index (M_w/M_n).

Conclusions

Completion of the multivalent capture probe in a flexible design allows for control over carbohydrate density and number of photocrosslinking groups is manifested in a cyanoxyl-mediated free-radical polymerization pathway. Furthermore, the end-labeled biotin facilitates purification without disrupting lectin-carbohydrate interactions. To complete our polymer synthesis, we will need to optimize the reaction conditions in which the polymerization can efficiently take place. After our model compound **19** has been successfully polymerized, we will polymerize it in the presence of the phenylazide monomer**.** Finally, we will polymerize our disaccharide monomer **12** with the phenylazide monomer **14** to produce our biotin-end labeled multivalent probe**.**

With the successful synthesis of our multivalent polymer, we will begin initial experiments on the capture of Fucα(1-2)Gal binding lectins located in hippocampal neurons. Once we have captured these lectins, we will be able to identify and characterize them via mass spectrometry. Following the characterization of these lectins, we will be able to perform key experiments in which lectin overexpression or site-directed mutagenesis experiments will help to elucidate the physiological roles of the lectins and their interactions with specific Fucα(1-2)Gal glycoproteins. Our discoveries should

provide a better understanding of how fucosyl saccharides modulate the molecular and cellular basis of neuronal communication.

Experimental Details

Carbobenzoxy 3-amino-1-propyl peracetylated-β-D-galactopyranoside (1). Peracetylated-β-D-galactopyranoside (18.6 g, 49.2 mmol) was dissolved in toluene/CH_2Cl_2 (1:1) (380mL). To this was added a solution of 3-amino-1-propanol *O*-benzylchoroformate (1.2 M in CH_2Cl_2, 50.0 mL, 59.1 mmol), followed by $BF_3 \bullet OEt_2$ (9.27 mL, 73.9 mmol). The reaction was stirred for 24 h at 0 °C. After completion, K_2CO_3 (3.84 g, 24.6 mmol) was added and the reaction stirred for an additional 30 min. The mixture was filtered, washed in water, and extracted three times with CH_2Cl_2. The organic phases were combined and dried over $MgSO_4$ then concentrated to afford a yellow syrup. The crude was purified by flash chromatography (1:1 EtOAc:hexanes) to afford **1** (10.5g, 40%). ^{1}H NMR (300 MHz, CDCl3): δ = 7.36 – 7.22 (m, 5H), 5.04 (s, 2H), 4.98 (dd, *J* = 3.6 Hz, *J* = 1.8 Hz, 1H) 4.43 (d, *J* = 8.1 Hz, 1H, H-1), 4.19 – 4.05 (m, 2H), 3.97 – 3.84 (m, 2H), 3.60 – 3.52 (m, 3H), 3.38 – 3.10 (m, 2H), 2.17 – 1.95 (m, 12H), 1.8 (m, 2H), 1.6 (s, 1H).

Carbobenzoxy 3-amino-1-propyl 3,4-*O*-isopropylidene-β-D-galactopyranoside (3). 1 (10.5 g, 19.5 mmol) was dissolved in MeOH (0.80 M, 263 mL) and NaOMe (8.00 M, 26.3 mL) and was monitored for completion using thin layer chromatography. The reaction was neutralized with Dowex 50X-8-200 resin (prewashed with MeOH). The resin was filtered and the filtrate concentrated in vacuo to afford a yellow solid that was subjected to flash chromatography (5:1:1 EtoAc, MeOH, H2O) to afford **2** (6.44g, 89% yield) as a white solid. **2** (0.58g, 1.56 mmol) was dissolved in acetonitrile (0.20 M, 8.00

mL) followed by addition of 2,2 dimethoxypropane (0.23 mL, 1.87 mmol). 10-CSA (0.018 g, 0.078 mmol) was then added and the reaction was stirred at room temperature for 3 h. 2,2 dimethoxypropane (1.00 mL) was then added and the reaction allowed to stir for an additional 16 h. The crude was purified using flash chromatography (100% EtOAc) to afford **3** as a yellow oil (0.33 g, 52%). ^{1}H NMR (300 MHz, $CDCl_3$): δ = 7.32 – 7.20 (m, 5H), 5.15 (t, J<1, 1H), 5.00 (s, 2H), 4.07 (d, *J* = 8.30, 1H, H-6), 4.05 – 3.97 (m, 2H), 3.92 – 3.82 (m, 2H), 3.79 – 3.70 (m, 2 H), 3.60 – 3.52 (m, 1H), 3.45 (t, *J* = 7.40, 2H), 3.24 – 3.15 (m, 1H), 1.81 – 1.66 (m, 2H), 1.41 (s, 3H), 1.22 (s, 3H). ESI/MS (M + Na) calcd for $C_{20}H_{29}NO_8$: 434.2, found 434.0.

Carbobenzoxy 3-amino-1-propyl 6-*O*-tert-butyldimethylsilyl-3,4-*O*-isopropylidene-β-D-galactopyranoside (4). **3** (0.27 g, 0.65 mmol) was dissolved in CH_2Cl_2 and cooled to –25 °C. t-Butyl dimethylsilylchloride (0.17 mL, 0.97 mmol) followed by imidazole (0.18g, 2.58 mmol) was added and the reaction stirred for 10 h at room temperature. The reaction was quenched with MeOH (0.65 mL), diluted with CH_2Cl_2, and washed with 1N HCl, $NaHCO_3$, brine, then dried over $MgSO_4$. The crude was purified by flash chromatography (2:1 hexanes, EtOAc) to afford **4** as a colorless syrup (0.22g, 64%). ^{1}H NMR (300MHz, $CDCl_3$): δ = 7.38 - 7.21(m, 5H), 5.05 (s, 2H), 4.22 (d, *J* = 7.8 Hz, 1H, H-1), 4.18 (dd, *J* = 1.8 Hz, 4Hz, 1H, H-6), 4.12 (d, *J* = 8.4, 1H, H-6'), 4.06 – 3.98 (m, 2H), 3.94 – 3.85 (m, 2H), 3.81 – 3.72(m, 1H), 3.62 – 3.50 (m, 2H), 3.46 – 3.37 (m, 1H), 3.35 – 3.20 (m, 2H) 1.86 – 1.70 (m, 2H), 1.50 (s, 3H), 1.32 (s, 3H), 0.89 (d, 4.2 Hz, 9H), 0.09 (d, *J* = 13.8 Hz), 6H). ESI/MS (M + Na) calcd for $C_{24}H_{43}NO_8Si$: 548.3, found 548.0.

Methyl α-L-fucopyranoside (5). L-Fucose (25.0 g, 152 mmol), Dowex 50W-X8 resin (scoopful), and MeOH (250 mL, 0.60 M) was combined in a 500 mL flask and refluxed for 48 h. The reaction was cooled, filtered and concentrated in vacuo to afford a white solid. This was recrystallized from 100% EtOAc (8.1 g, 30%). ^{1}H NMR (300 MHz, $CDCl_3$): δ = 4.76 (d, *J* = 3.3 Hz, 1H, H-1), 4.04 (m, 1H, H-5), 3.77-3.90 (m, 3H, H-2, H-3, H-4), 3.38 (s, 3H), 1.21 (d, *J* = 6.6 Hz, 3H). ESI/MS (M + Na) calcd for $C_7H_{14}O_5$ 201.04, found 201.0.

Methyl 2,3,4-tri-*O*-benzyl-L-fucopyranose (6). **5** (8.10 g, 45.5 mmol) was dissolved in DMF (16.2 mL, 0.30 M). NaH, 60% dispersion (6.60 g, 273 mmol) was added portionwise and the reaction stirred for 2 h. The reaction was then cooled to 0°C and benzyl bromide (16.2 mL, 137 mmol) was added dropwise. The reaction was stirred at room temperature overnight. MeOH was then added to quench the reaction and the mixture poured over cold EtOAc and water. The aqueous was extracted with EtOAc three times, the organic layers were combined, dried over $MgSO_4$and concentrated in vacuo to afford a yellow syrup. The crude was purified by flash chromatography (5:1 hexanes/EtOAc) to afford a white crystalline solid **6** (9.1g, 45%). ^{1}H NMR (300 MHz, $CDCl_3$): δ = 7.34-7.24 (m, 15H), 4.65 (d, *J* = 3.3 Hz, H-1), 4.63 –5.04 (m, 6H), 4.03 (dd, *J* = 9.90 Hz, 3.90 Hz, 1H, H-2), 3.95 (dd, *J* = 10.2 Hz, *J* = 3.30 Hz, 1H, H-3), 3.83 (m, *J* = 6.50 Hz, 1H, H-5), 3.65 (dd, 1H, H-4), 3.37 (s, 3H), 1.12 (d, *J* = 6.60 Hz, 3H). ESI/MS (M + Na) calcd for $C_{28}H_{32}O_5$ 471.2, calcd 471.2.

2,3,4-Tri-*O*-benzyl-L-fucopyranose (7). **6** (9.10 g, 20.3 mmol) was dissolved in a solution of 80% acetic acid (144 mL) and 1N HCl (80.0 mL). The reaction was heated between 95 –100 °C. After cooling, the reaction was extracted three times with CH_2Cl_2.

The CH_2Cl_2 solution was washed with cold $NaHCO_3$ (sat), followed by a wash with water. The organic phases were combined and dried over $MgSO_4$, filtered, and concentrated in vacuo. The crude was then purified by silica chromatography (5:1 hexanes/EtOAc) to afford **7** (5.0 g, 57%). ^{1}H NMR (300 MHz, $CDCl_3$): δ = 7.25 – 7.37 (m, 15 H), 5.30 (s, 1H, H-1), 4.98 – 4.66 (m, 6H), 4.10 (q, *J* = 6.6 Hz), 4.05 (dd, *J* = 3.90 Hz, 9.90 Hz, 1H, H-2), 3.89 (dd, *J* = 2.70 Hz, 9.90 Hz, 1H, H-3), 1.14 (d, *J* = 6.60 Hz, 3H). ESI/MS (M + Na) calcd for $C_{27}H_{30}O_5$: 457.2, found 457.2.

Carbobenzoxy 3-amino-1-propyl 6-*O*-tert-butyldimethylsilyl-3,4-*O*-isopropylidene-2-*O*-(2,3,4-tri-*O*-benzyl-α -L-fucopyranosyl)-β-D-galactopyranoside (9). **7** (0.25 g, 0.58 mmol) and K_2CO_3 was dissolved in CH_2Cl_2 (4.10 mL, 0.14M), followed by the addition of Cl_3CCN (0.31 mL, 3.1 mmol). The reaction was stirred at room temperature for 15 min. followed by the portionwise addition of NaH (0.015 g, 0.63 mmol). The reaction was stirred overnight. The crude mixture was passed through celite and washed three times with anhydrous CH_2Cl_2. The crude reaction was then concentrated in vacuo to afford a yellow syrup (0.36 g) and immediately used for the next reaction. **4** (0.11 g, 0.21 mmol) and **8** (0.36 g, 0.63 mmol) were combined in a round bottom flask, azeotroped three times with toluene, and dried under high vacuum for 6 h. Dry ether was then added and the reaction stirred for 15 min. TMSOTf (16.0 uL, 0.09 mmol) was diluted in ether (0.10 M, 0.90 mL), cooled to 0 °C and added to the mixture containing **4** and **8.** The reaction was warmed to room temperature and stirred for 16 h. The reaction was slowly quenched with $NaHCO_3$ (1.90 g) and stirred for 30 min. It was then diluted with water and EtOAc. The aqueous and organic layers were extracted, and the aqueous extracted three times with EtOAc. The organic layers were combined, washed with brine,

dried over $MgSO_4$, filtered and concentrated to afford a yellow syrup. The product was purified by flash chromatography (6:1 hexanes/EtOAc) to afford a white crystalline solid **9** (0.08 g, 42%). ^{1}H NMR (300 MHz, $CDCl_3$): δ = 7.38 - 7.11 (m, 20H), 5.46 (d, *J* = 4.0 Hz, 1H), 5.03 - 4.53 (m, 8H), 4.25 – 4.14 (m, 2H), 4.13 – 3.98 (m, 4H), 3.86 – 3.79 (m, 4H), 3.77-3.65 (m, 2H), 3.52 – 3.35 (m, 3H), 3.16 (q, *J* = 6.3 Hz, 2H), 1.76 – 1.50 (m, 2H), 1.40 (s, 3H), 1.21 (s, 3H), 1.22(d, *J* = 6.6 Hz, 3H), 0.8 (s, 9H), 0 (s, 6H). ESI/MS (M + Na) calcd for $C_{45}H_{63}O_{10}Si$: 964.5, found 965.0.

Carbobenzoxy 3-amino-1-propyl 2-*O*-(2,3,4-tri-*O*-benzyl-α -L-fucopyranosyl)-β-D-galactopyranoside (10). **9** (0.018 g, 0.021 mmol) was dissolved in 2:1 acetic acid/THF (0.10 M, 0.21 mL), pH~1.5, and stirred at 34 °C for 48 h. The reaction was then diluted with water and EtOAc and the aqueous extracted three times with EtOAc. The organic layers were combined, dried over $MgSO_4$, filtered, and concentrated in vacuo to afford a white crystalline solid **10** (0.01 g, 66%). **10** (0.012 g, 0.021 mmol) was dissolved in MeOH (0.42 mL, 0.20 M). 10% Pd-C (0.002 g) was added and the flask purged once with argon and twice with hydrogen. The reaction was stirred under hydrogen gas for 5 h at room temperature. The reaction was filtered through celite and concentrated in vacuo to yield a white solid (4.80 g, 87%). ^{1}H NMR (300 MHz, D_2O) δ = 5.21 (d, J = 2.20 Hz, 1H, H-1'), 4.40 (d, *J* = 7.80 Hz, H-1), 4.11 – 3.44 (m, 12H, H-2, H-3, H-4, H-5, H-6a, H-6b', H-2', H-3', H-4', H-5', CH_2), 3.21 (m, 2H), 1.84 – 1.68 (m, 2H), 1.04 (d, *J* = 6.60 Hz, 3H). ESI/MS (M + Na) calcd for $C_{15}H_{29}NO_{10}$: 406.2, found 406.0.

1,3 Diaminopropyl N-succinimdyl-4-azidobenzoate (13). Triethylamine (0.02 mL, 0.14 mmol) was added to a solution of N-succinimidyl 4-azidobenzoate (0.05 g, 0.02

mmol) and 1,3-diaminopropane THF/DMF (1:1). The reaction was purified by flash chromatography (5:1:1 EtOAc/MeOH/H_2O).

4-Nitrobenzyl-biotinamide (15). To a solution of *p*-nitrobenzylamine (0.08 g, 0.41 mmol) in DMF (1.60 mL) was added triethylamine (0.50 mL, 0.56 M). After the solution was stirred for 30 min., a solution of *N*-hydroxysuccinimide-biotin (0.10 g, 0.29 mmol) was added. The reaction mixture was stirred for 24 h at room temperature, then concentrated in vacuo to give a dark yellow residue which was purified by gradient flash chromatography (100% chloroform to 9:1 chloroform/MeOH) to afford a yellow solid (0.08 g, 53%). ^{1}H NMR (300 MHz, DMSO-d_6): δ = 8.50 (t, *J* = 7.60 Hz, 1H), 8.19 (d, *J* = 9.9 Hz, 2H), 7.52 (d, *J* = 9.90 Hz, 2H), 6.42 (s, 1H), 6.38 (s, 1H), 4.39 (m, 2H), 4.30 (dd, *J* = 4.50, 8.30 Hz, 1H), 4.10 (m, 4H), 3.19 (d, *J* = 4.2 Hz, 1H), 2.82 (dd, 1H, *J* = 12.4, 4.5 Hz), 2.60 (s, 2H), 2.18 (t, *J* = 7.90 Hz, 2H), 1.59 (m, 4H), 1.33 (m, 2H). ESI/MS (M + Na) calcd for $C_{17}H_{22}N_4O_4S$: 379.14, found 378.0.

4-Aminobenzyl-biotinamide (16). In the presence of Pd-C (0.019 g), **15** (48.2 g, 0.13 mmol) in anhydrous DMF (2.50 mL, 0.05M) was charged with hydrogen balloon for 4 h at room temperature. The reaction mixture was filtered through celite, and the filtrate evaporated to provide a yellow residue that was purified by flash chromatography (5:1 chloroform/MeOH) to afford a light yellow solid **16** (0.02g, 50%). ^{1}H NMR (300 MHz, CD_3OD): δ = 6.95 (d, *J* = 8.10 Hz, 2H), 6.05 (d, *J* = 8.10 Hz, 2H), 4.38-4.40 (m, 1H), 4.11 (s, 1H), 3.22 (m, 1H), 3.12 (dd, *J* = 4.90, 12.6 Hz, 1H), 2.59 (d, *J* = 12.7 Hz, 1H), 2.13 (t, *J* = 9.80 Hz, 2H), 1.70-1.42 (m, 4H), 1.38-1.22 (m, 2H). ESI/ MS (M + Na) calcd for $C_{17}H_{24}N_4O_2S$: 348.16, found 349.0.

Copolymerization of 3-acrylamino-1-propyl *O*-galactopyranoside (17) and acrylamide by biotin arylamine initiator and NaOCN.

16 (0.003g, 0.009 mmol) was reacted with HBF_4 48% wt (2.50 uL, 0.039 mmol) at 0 °C in 1:1 H_2O/THF (0.1 mL) under argon. The diazonium salt was generated by adding sodium nitrite (0.076 g, 0.011 mmol) to the reaction medium. After 30 min., a degassed mixture of **19** (0.0065 g, 0.022 mmol), acrylamide (0.011 g, 0.16 mmol), and sodium cyanate (0.029 g, 0.045 mmol) dissolved in 1:1 H_2O/THF (0.1 mL) were introduced into the flask containing the diazonium salt. The polymerization medium was then heated to 50 °C for 16 h. The cooled reaction was dialyzed exhaustively against deionized water for 18 h followed by lyophilization.

3-acrylamino-1-propyl-*O*-galactopyranoside (18). 2 (1.31 g, 3.5 mmol) was dissolved in MeOH (39 mL, 0.09M). 10% Pd-C (0.14 g) was added and the reaction purged once with argon and twice with hydrogen gas. The reaction was stirred for 8 h under hydrogen gas at room temperature, followed by filtration through celite. The filtrate was concentrated in vacuo to afford **18** (0.72, 87%) which was used in situ for the next reaction. **18** (0.20 g, 0.84 mmol) was dissolved in a solution of MeOH (2.10 mL, 0.4 M) and triethylamine (1 mL) and was cooled to 0°C. N-acryloxysuccinimide (0.36g, 2,1 mmol) was added. After 5 h, a fresh portion of N-acryloxysuccinimide was added and the temperature allowed to reach 25°C. The reaction was stirred overnight, followed by purification via flash chromatography (5:1:1 EtOAc/MeOH, H_2O to yield **19** (0.067 g, 27%). ^{1}H NMR (300 Mhz, D_2O): δ = 6.18 (d, J = 1.80 Hz, 2H), 5.73 (dd, J = 7.80 Hz, 1.8 Hz, 1H), 4.37 (d, 7.8 Hz, 1H, H-1), 3.98 - 3.90 (m, 3H), 3.82 – 3.61 (m, 6H), 3.53 –

3.47 (m, 2H), 3.34 (t, J = 5.1 Hz, 2H). ESI/MS (M + Na) calcd for $C_{12}H_{21}NO_7$: 313.1, found 313.0.

Carbobenzoxy 3-amino-1-propanol (20). 3-amino-1-propanol (44 g, 586 mmol) was dissolved in THF (100 mL, 2.9 M) and the temperature lowered to 0°C. Benzylchloroformate (50.0 g, 293 mmol) was added dropwise and the reaction stirred for 30 min. The reaction was concentrated in vacuo as a colorless oil. The mixture was extracted in 10% HCl and CH_2Cl_2 three times and the organic layers combined and dried over $MgSO_4$. The organic phases were then concentrated in vacuo to afford a white solid (53.9 g, 88%). ^{1}H NMR (300 MHz, $CDCl_3$): δ = 7.38 – 7.25 (m, 5H), 5.11 (s, 2H), 3.68 (t, *J* = 5.4 Hz, 2H), 3.38 – 3.34(t, *J* = 6.3 Hz, 2H), 2.08 (s, 1H), m (1.74 – 1.66). ESI/MS (M + Na) calcd for C11H15NO3: 232.1, found 232.0.

References

1. Bovin, N., Yu E, Korchagina T. *Glycoconjugate J*. **1993**, 10, 142-151.
2. Kalovidouris S., Gama C., Hsieh-Wilson, L. *J. Am. Chem. Soc.* **2005**, 127, 1340-1341.
3. Murrey, H., Kalovidouris S., Gama C., Luo W., Porton, B., Hsieh-Wilson L. *Proc. Natl. Acad. Sci. U.S.A.* **2005,** 103, 21-26.
4. Kaifre, R., Plantefaber L, Goldstein I. *J. Carbohydr. Res.* **1985**, 140, 37-49.
5. Lowary T, Hindsgaul O. *Carbohydr. Res.* **1993**, 249, 163-165.
6. Zhang, Z., Magnusson, G. *Carbohydr. Res.* **1994**, 262, 79-101.
7. Toone E. *Curr. Opin. Struct. Biol*. **1994**, 4, 719-728.
8. Sun, X., Faucher K., Houston, M., Grande, D., Chaikof, E. *J. Am. Chem. Soc*. **2002**, 124, 7258-7259.
9. Hermanson, G. *Bioconjugate Techniques*. 1996, Academic Press, Inc., 163-255.
10. Watson, J., Spaltenstein, A., Kingery, J., Whitesides, G. *J. Med. Chem*. **1994**, 37, 3419-3433.
11. Mammen, M., Dahmann, G., Whitesides, G. *J. Med. Chem*. **1995**, 38, 4719-4190.
12. Mereyala, H., Gurrala, S. *Carbohydr. Res*. **1998**, 307, 351-354.
13. Liptak, A., Fugedi, P., Kerekgyarto, J., Nanasi, P. *Carbohydr. Res.* **1983**, 113, 225-231.
14. Catelani, G., Colonna, F., Marra, A. *Carbohydr. Res.* **1988**, 182, 297-300.
15. Barili, P., Berti, G., Catelani, G., Colonna, F., Marra, A. *Tetrahedron Lett*. **1986**, 27, 2307-2310.

16. Wegmann, B., Schmidt, R. *Carbohydr. Res.* **1988**, 184, 254-261.

17. Wang, C., Lee, J., Luo, S., Fan, H., Pai, C., Yang, W., Lu, L., Hung, S. *Angew. Chem. Int. Ed*. **2002**, 41, 2360-2362.

18. Sassaman, M., Kotian, K., Prakash, S., Olah, G. *J. Org. Chem*. **1987**, 52, 4314-4319.

19. Ibatullin, F., Shabalin, K., Janis, J., Shavva, A. *Tetrahedron Lett*. **2003**, 44, 7961-7964.

20. Zanetta, J., *Acta Anat.* **1998**, 161, 180-195.

21. Charter, M., Koshland, L., Bertozzi, D. *J. Biol. Chem.* **2002**, 277, 9255-9261.

22. Lyon, M., Gallagher, J. *J. Matrix. Biol*. **1998**, 17, 485-493.

23. Ethell, I., Yamaguchi, Y. *J. Cell Biol*. **1999**, 144, 575-586.

24. Kinnunen, A., Niemi, M., Kinnune, T., Kaksonen, M., Nolo, R., Rauvala, H. *Eur. J. Neurosci.* **1999**, 11. 491-502.

25. Walz, A., McFarlane, S., Brickman, Y., Nurcombe, V., Bartlett, P., Holt, C. *Development* **1997**, 124, 2421-2430.

26. Zanetta, J., Reeber, A., Vincendon, G., Gombos, G. *Brain Res*. **1977**, 138, 317-328.

27. Krusius, T., Finne, J. *Eur. J. Neurosci*. **1977**, 78, 369-379.

28. McCabe, N., Rose, S. *J. Neurochem*. **1987**, 48, 538-542.

29. Krug, M., Jork, R., Reymann, K., Wagner, M., Matthies, H., *Brain Res.* **1991**, 540, 237-242.

30. Matthies, H., Kretlow, J., Smalia, K., Staak, S., Krug M., *Neurosci*. **1999**, 91, 175-183.

31. Angenstein, F., Matthies, H., Staeck, S., Reymann, K., Staak S. *Neurochem. Int.* **1992**, 21, 403-408.

32. Sukumar, R., Rose, S., Burgoyne, R. J. *Neurochem*. **1980**, 34, 1000-1006.

33. Wetzel, W., Popov, N., Lossner, B., Schulzeck, S., Honza, S., Matthies, H. *Pharmacol. Biochem. Behav*. **1980**, 13, 765-771.

34. Grande, D., Baskaran, S., Baskaran, G., Chaikof, E. *Macromolecules* **2000**, 33, 1123-1125.

35. Hou, S, Sun, X., Dong, C. Chaikof, E. *Bioconjugate Chem*. **2004**, 15, 954-959.

36. Fisher, A., Mann, A., Verma, V., Thomas, N., Mishra, R., Johnson, R. *J. Med. Chem.* **2006**, 49, 307-317.

37. Kiessling, LL., Gestwicki, JE., Strong, LE. *Angew Chem Int Ed Engl*. **2006**, 45, 2348-68.

38. Wassler, MJ., Shur, BD. *J Cell Sci*. **2000**, 113, 237-45.